國立臺灣大學工學院化學工程學系

碩士論文

Department of Chemical Engineering

College of Engineering

National Taiwan University

Master’s Thesis

以分子設計與溶液製程優化提升有機太陽能電池性能之研究

Molecular Design and Eco-Friendly Processing for High-Performance Organic Solar Cells

張嘉富

Jia-Fu Chang

指導教授:闕居振 博士

Advisor: Chu-Chen Chueh, Ph.D

中華民國 114 年 7 月

July, 2025

doi:10.6342/NTU202502276

口試委員會審定書

MASTER'S THESIS ACCEPTANCE CERTIFICATE
NATIONAL TAIWAN UNIVERSITY

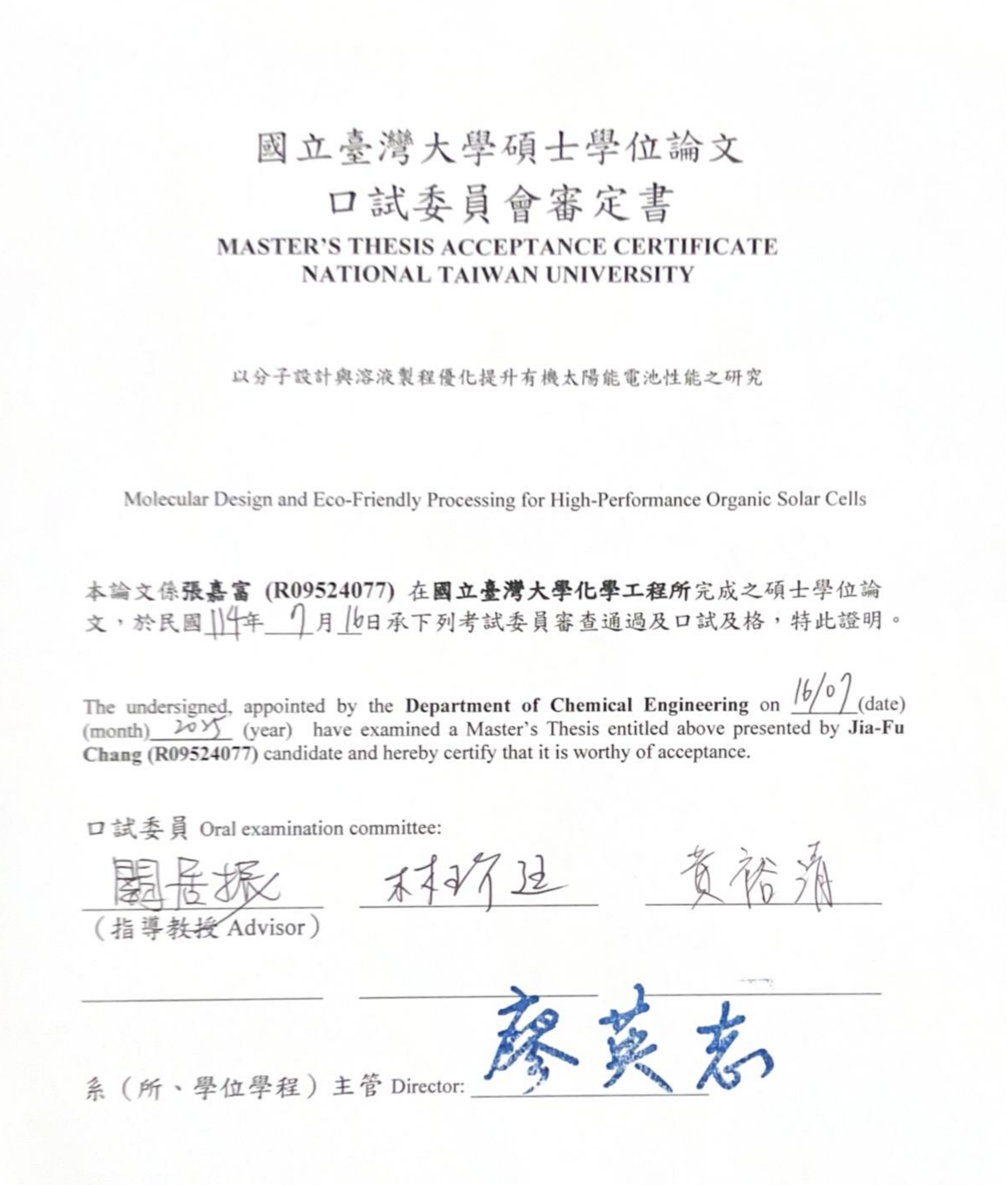

國立臺灣大學碩士學位論文
口試委員會審定書
MASTER'S THESIS ACCEPTANCE CERTIFICATE
NATIONAL TAIWAN UNIVERSITY

以分子設計與溶液製程優化提升有機太陽能電池性能之研究

Molecular Design and Eco-Friendly Processing for High-Performance Organic Solar Cells

本論文係**張嘉富 (R09524077)** 在**國立臺灣大學化學工程所**完成之碩士學位論文，於民國114年7月16日承下列考試委員審查通過及口試及格，特此證明。

The undersigned, appointed by the **Department of Chemical Engineering** on 16/07 (date) (month) 2025 (year) have examined a Master's Thesis entitled above presented by **Jia-Fu Chang (R09524077)** candidate and hereby certify that it is worthy of acceptance.

口試委員 Oral examination committee:

闕居振　林祈廷　黃裕清

（指導教授 Advisor）

系（所、學位學程）主管 Director: 廖英志

doi:10.6342/NTU202502276

誌謝

首先，衷心感謝闕老師這幾年的教導和幫助，闕老師在學術上，會與學生積極討論並給予實質的建議，從研究主題的發想、實驗設計，到論文的撰寫，總是耐心地給予意見，讓我在研究路上得以穩健前行。除了在學術上的交流，老師更會關心學生的生活，常常會跟我們分享人生的一些價值觀，帶領我去看見更廣更遼闊的視野。老師從不吝於讓學生出國去參加研討會，如果有機會也會送我們去國外與當地實驗室交流學習，也因此我才能獲得這些寶貴的經驗。而在老師紮實的訓練下，我才能培養出不錯的研究素養及解決實驗問題能力。最後想感謝老師，在我低潮、狀態最差的時候拉我一把，老師對我從不放棄，因為有老師的那些諄諄教誨，我也才能往人生的下一篇章邁進。總而言之，闕老師在學術中是一位受人尊敬的師長;在生活中更是一位值得信任且十分可靠的引路人，非常感謝老師。

接著感謝帶我入門的師父柏辰、丞典，總是耐心仔細地教我做實驗以及傳授我許多 OPV 的知識，讓當時處於初學者的受益良多。感謝玠廷學長，讓我有機會能參與與英國合作的 work，有了學長的幫助，使我的實力往更上一層推進，首次去澳洲參加研討會，也因為有了這個 work，讓我可以和國外人士交流切磋。感謝同居的誌元、明軒，生活上如果遇到挫折跟你們分享，總能得到慰藉，研究路上也才不會感到徬徨，明軒優秀的研究能力也幫助了我不少，出國也都是靠明軒的照顧才能讓旅途順利。感謝吳哥、炯翰，這兩位學長跟學弟相處沒有一絲距離感，實驗室有吳哥的存在，氣氛十分熱鬧及歡樂，在研究生涯中，也常常和炯翰聊一些實驗問題及看法，學術討論之餘，和炯翰聊聊生活瑣事與興趣，都非常的自在，日本行因為有他完美的規劃，那些回憶令我如今始終難以忘懷。

接續我想感謝我的 OPV 組戰友宇呈，宇呈待人十分真誠且幽默風趣。同為南部人，彼此之間相處非常契合。在實驗上，會一起找 bug 讓元件的效率變高，每次做出來效率的進步，哪怕只是增加一點，也會感到十分振奮。追求效率提高的路上很辛苦，從一開始抓不到基準點到能與世界匹敵，如果沒有宇呈那份勇於嘗試以及全力以赴的態度是無法達成的。而在碩論第三章中有許多實驗的量測以及數據分析，都是宇呈花時間帶我做的，如果沒有他的幫忙，這篇 paper 上的邏輯以及故事性是無法完整通順的。跟宇呈聊碰到的挫折，他也總不耐煩地聆聽並給予建議，OPV 組能跟宇呈同行，讓我在研究路途中不感到孤獨。

再來我想感謝實驗室的夥伴們，稟翔、世峰、奕翔、沛瑾、婾婷、昱寬、彥涵、音醍、丁力、冠霖、浩維、家洵、宇翔、旭孜、筑雁、小汪、丞祐、昶睿等等。實驗室的每個人都很友善，相處融洽且溫馨，讓我的研究生涯增添了許多色彩及樂趣，十分感謝大家的幫忙。

最後，我想感謝我的朋友及家人，謝謝朋友們總是很義氣地陪在我身邊，在失落時，總能提供幫助，並且讓我歡笑，彼此之間也創造了許多很美好的回憶。謝謝我的父母，一路拉拔我長大，在我做任何決定時都會支持我，絕不會有任何怨言，提供生活費及學費使我無後顧之憂，在我低潮時也給予鼓勵，每次回嘉義時都能好好充電，有了父母無條件的支持與鼓勵，我才能有前進的動力並且順利完成學業，非常感謝愛我的父母。

摘要

有機太陽能電池(Organic Solar Cells, OSCs)因其輕量化、機械柔性佳，以及可相容於低成本溶液製程等特性，被視為極具潛力的新興光電技術。在多種 OSC 架構中，目前主要發展方向可分為兩類：其一為採用聚合物與非富勒烯小分子受體(non-fullerene acceptors, NFAs)組成的混合型系統(polymer:NFA)；其二則為全聚合物太陽能電池(All-Polymer Solar Cells, All-PSCs)，即同時以共軛高分子作為電子施體與受體材料。前者已達成優異的光電轉換效率(PCE)，但仍面臨施體材料分子設計與形貌穩定性等挑戰；而後者雖具備更優異的熱穩定性、機械強度與長期穩定性，卻因兩種聚合物間相容性差與形貌控制困難，導致元件表現及可重複性受限。

本論文針對上述兩類系統所面臨之材料與製程挑戰，分別提出兩項互補且具策略性的解決方案：(1) 在 polymer:NFA 系統中，透過分子工程手法設計並優化聚合物施體的結構與光電特性；(2) 在 All-PSC 系統中，導入綠色共溶劑搭配揮發性固態添加劑的製程策略，以調控主動層的微觀形貌並實現理想的電荷傳輸行為。

在材料分子設計方面，本研究合成六種以異靛青(isoindigo)為主體的共軛高分子電子給體，並系統性探討其側鏈對稱性與主鏈氟化對光電與結晶性質的影響。這些材料分為兩大系列：未氟化的 PII2T 系列(**P1-P3**)與氟化的 PII2TF 系列(**P4-P6**)，其中側鏈分別採用對稱(雙 DT 或雙 SiO-C8)或非對稱(DT/SiO-C8)設計。分析結果指出，氟化能有效提升分子的共平面性與 π-π 堆疊能力，而非對稱側鏈設計則有助於形成有利的 face-on 堆疊取向與更緊密的鏈間堆積。基於非對稱側鏈的 **P2** 與 **P5** 在各自系列中表現出最高的功率轉換效率(PCE)，並在短路電流(J_{sc})、填充因子(FF)與復合抑制方面皆有顯著改善。此外，氟化設計亦能減緩側鏈結構變異對形貌與元件效能的影響，提升元件穩定性與製程耐受度。本部分結果突顯了分子結構工程在優化 OSC 材料性能中的關鍵角色。

接續材料設計成果，本研究進一步發展綠色溶劑製程策略，應用於高性能 PM6:PY-IT 全高分子主-受體系統，以優化其活性層形貌並兼顧環境永續性。鑑於傳統使用的氯仿(CF)對環境與健康具潛在危害，本研究選用三種較高沸點的環保輔助溶劑—THF、2-MeTHF 與 3-MeTHF—與 CF 混合，以調控薄膜形成過程中的乾

燥速率。再搭配具揮發性的固體添加劑，得以在不殘留的前提下，有效調控聚合物聚集、相分離行為與奈米結構形成。紫外可見光譜與變溫吸收測試證實，混合溶劑系統能促進分子間有序堆積並穩定溶液態聚集。另外由同步輻射之結果則指出，這些製程條件有助於降低相區尺寸、增進垂直結晶性並提升主/受體的混合相容性。CF+THF 與 CF+2-MeTHF 製程所製備的元件其 PCE 皆超過 17%，顯著優於使用純 CF 或 CF+3-MeTHF 之對照組。此類元件不僅展現更佳的電荷傳輸平衡與抑制復合能力，其薄膜亦具備較高的內建電壓、更低的陷阱密度與能態整序，進一步提升激子解離效率、電荷抽取能力與開路電壓(V_{oc})。此外，此優化策略同樣適用於雙成份(binary)與三成份(ternary)系統，顯示出其高度通用性與潛力。

綜合上述研究成果，本論文從材料分子設計到製程控制，建立了一套完整策略以系統性優化有機太陽能電池之奈米形貌、光電特性與載子動態行為。本研究不僅提供深入理解 OSC 中結構-形貌-性能之關聯性，也為未來發展具備高效率與環境永續性的製程技術奠定重要基礎。

Keywords: 有機太陽能電池、以異靛藍為基礎的給體高分子、主鏈氟化改質、側鏈工程設計、形貌控制、綠色溶劑工程

Abstract

Organic solar cells (OSCs) have emerged as a promising photovoltaic technology due to their lightweight nature, mechanical flexibility, and compatibility with low-cost solution processing. Among various OSC architectures, two major directions have demonstrated significant potential: polymer:non-fullerene acceptor (polymer:NFA) systems, and all-polymer solar cells (All-PSCs), which utilize conjugated polymers as both donor and acceptor. While polymer:NFA systems have achieved excellent power conversion efficiencies (PCEs), ongoing challenges remain in optimizing donor molecular design and reducing morphology sensitivity. All-PSCs, on the other hand, offer enhanced thermal stability, mechanical robustness, and long-term device durability, but suffer from more complex morphology control and limited miscibility between two polymer components.

To address these challenges across both material systems, this thesis integrates two synergistic strategies: (1) molecular engineering of donor polymers in polymer:NFA systems to enhance structural and electronic properties, and (2) solvent-processing optimization in All-PSCs using green co-solvents and solid additives to achieve ideal phase morphology and balanced charge transport.

For molecular engineering of conjugated polymers, six isoindigo-based donor polymers were synthesized and systematically investigated to evaluate the effects of side-chain symmetry and backbone fluorination on their optoelectronic and morphological properties. The polymers were divided into two series—PII2T (non-fluorinated, **P1–P3**) and PII2TF (fluorinated, **P4–P6**)—with variations in symmetric or asymmetric side-chain substitution using alkyl (DT) and siloxane (SiO–C8) branches. Optical absorption, cyclic voltammetry, and GIWAXS analyses

revealed that backbone fluorination significantly improves molecular planarity and facilitates stronger π–π stacking, while asymmetric side chains induce favorable face-on orientation and tighter interchain packing. Devices based on asymmetric polymers (**P2** and **P5**) exhibited the highest power conversion efficiencies (PCEs) in each series, with enhanced short-circuit current (J_{sc}), fill factor (*FF*), and reduced recombination losses. Furthermore, fluorination was shown to mitigate the influence of side-chain structure, improving morphology robustness and reducing performance variation. These findings underscore the importance of rational molecular engineering in optimizing OSC materials for enhanced device performance.

Building upon these insights into material design, a green solvent engineering strategy was developed to further optimize the morphology of All-PSCs based on a high-performance PM6:PY-IT donor–acceptor blend. Recognizing the environmental and health concerns associated with commonly used solvents like chloroform (CF), three eco-friendly co-solvents—tetrahydrofuran (THF), 2-methyltetrahydrofuran (2-MeTHF), and 3-methyltetrahydrofuran (3-MeTHF)—were blended with CF to modulate the drying kinetics during film formation. In combination with a volatile solid additive (DTT), this strategy enabled precise control over domain size, polymer aggregation, and phase separation dynamics. Optical absorption and temperature-dependent UV-Vis measurements confirmed that the mixed solvent systems promoted more ordered molecular packing and stronger solution-state aggregation. GIWAXS and GISAXS analyses further showed that these processing conditions resulted in reduced domain sizes, enhanced vertical crystallinity, and improved donor–acceptor miscibility. Devices fabricated with CF+THF and CF+2-MeTHF blends achieved PCEs over 17%, significantly outperforming devices processed with only CF or with CF+3-MeTHF. These high-performing devices

exhibited balanced charge transport and suppressed recombination losses. Additionally, the optimized films exhibited higher built-in potential, lower trap densities, and reduced energetic disorder, all of which contributed to enhanced exciton dissociation, more efficient charge extraction, and higher V_{oc} values. These improvements were consistently observed across binary and ternary device systems, confirming the generality and robustness of the proposed solvent engineering approach.

Together, the results provide a comprehensive framework for tuning the nanoscale morphology, optoelectronic properties, and charge transport characteristics of OSCs. This study not only contributes valuable insights into structure—morphology—performance relationships in OSCs, but also offers practical guidelines for scaling up organic photovoltaics with eco-conscious manufacturing protocols.

Keywords: Organic solar cells, isoindigo-based donor polymers, backbone fluorination, side-chain engineering, morphology control, green solvent engineering

doi:10.6342/NTU202502276

Contents

doi:10.6342/NTU202502276

List of Figures

doi:10.6342/NTU202502276

doi:10.6342/NTU202502276

List of Tables

doi:10.6342/NTU202502276

CHAPTER 1

Introduction

1.1 Background on Photovoltaic Technologies

As the global demand for energy continues to grow, concerns about climate change, fossil fuel depletion, and environmental degradation have intensified the push for clean, renewable energy sources. Among various renewable options, solar energy stands out due to its abundance, sustainability, and direct conversion into electricity through photovoltaic (PV) technology. Photovoltaics provide a decentralized and scalable solution for energy generation, offering the potential to power everything from small electronic devices to industrial-scale energy grids.

Traditional photovoltaic systems, most notably those based on crystalline silicon (c-Si), have dominated the commercial solar market for decades. While c-Si solar cells offer high power conversion efficiencies (PCEs) and long-term operational stability, their production involves energy-intensive processes, rigid form factors, and limited compatibility with lightweight or flexible applications. These limitations have prompted the exploration of next-generation photovoltaic technologies, including perovskite solar cells, dye-sensitized solar cells, and organic solar cells (OSCs). OSCs, in particular, have emerged as an attractive alternative due to their unique advantages, such as mechanical flexibility, low-cost solution processability, and the potential for large-area roll-to-roll manufacturing.[1-3] As shown in **Figure 1-1**, these properties open new possibilities for applications in portable electronics, building-integrated photovoltaics (BIPV), and wearable energy devices.[4, 5] Furthermore, the tunability of organic semiconductors at the molecular level enables precise control over optical absorption, energy levels, and charge transport properties, offering a versatile platform for continuous performance improvements.[6, 7]

Despite these advantages, achieving high-efficiency, stable, and scalable OSCs remains a key challenge. Central to overcoming this challenge is a deeper understanding of the interplay between material structure, processing methods, and device physics—a theme that underpins the present research.

1.2 Organic Solar Cells (OSCs)

1.2.1 Working Mechanism of OSCs

Organic solar cells (OSCs) convert sunlight into electricity through a sequence of photophysical and charge transport processes within organic semiconducting materials. Upon illumination, photons are absorbed by the active layer, promoting electrons to an excited state and forming tightly bound excitons due to the inherently low dielectric constant of organic materials.[8, 9] These excitons must reach a donor–acceptor (D/A) interface within their limited diffusion length—typically around 10 to 20 nanometers—before recombining. At the D/A interface, the exciton undergoes dissociation, driven by the energy level offset between the donor and acceptor components, resulting in the generation of free charge carriers (electrons and holes).[10] These carriers then migrate through their respective transport pathways, with electrons

doi:10.6342/NTU202502276

moving through the acceptor domains and holes through the donor domains, toward the cathode and anode, respectively. Ultimately, the separated charges are collected at the electrodes, producing photocurrent, as shown in **Figure 1-2**.[11]

Each step of this mechanism—from photon absorption and exciton diffusion to charge separation and collection—is strongly influenced by the molecular structure of the active layer materials and their morphological organization. Therefore, even subtle variations in material design or film formation conditions can significantly impact the overall efficiency of OSCs.

1.2.2 The Role and Design of the Bulk Heterojunction (BHJ) Layer

To improve exciton dissociation and facilitate efficient charge transport, most OSCs adopt a bulk heterojunction (BHJ) architecture in which donor and acceptor materials are intimately blended.[12] This bicontinuous interpenetrating network increases the D/A interfacial area and provides continuous pathways for both electrons and holes to reach their respective electrodes. The effectiveness of the BHJ depends on achieving an optimal nanoscale morphology, characterized by well-dispersed donor and acceptor domains with suitable size and purity. If the domains are too large, excitons may recombine before reaching the D/A interface; if the domains are too finely mixed, charge carriers may encounter difficulties finding uninterrupted percolation paths, leading to recombination losses, as shown in **Figure 1-3**.[13, 14] Consequently, both the thermodynamics and kinetics of film formation must be carefully controlled.

This morphological control is typically achieved through a combination of molecular design—such as tuning the backbone planarity, introducing side-chain modifications, or employing non-covalent interactions—and processing techniques,

doi:10.6342/NTU202502276

including solvent selection, additive incorporation, thermal annealing, and solvent vapor annealing, as shown in **Figure 1-4.**[15, 16] The BHJ structure remains a cornerstone of OSC development, offering a flexible and tunable platform for optimizing device performance.

1.2.3 Recent Progress and Key Challenges

Over the past decade, OSCs have made remarkable strides, with single-junction devices achieving power conversion efficiencies exceeding 19%.[17, 18] This progress has been driven by the development of non-fullerene acceptors (NFAs), which offer broader absorption, better energy level alignment, and improved morphological stability compared to their fullerene-based predecessors.[19] Alongside, new classes of donor–acceptor conjugated polymers have been synthesized, enabling fine control over optical and electronic properties, as well as enhanced molecular packing. At the same time, significant innovations in processing strategies—such as solvent and additive engineering—have enabled better control over phase separation and domain purity within the BHJ layer. These combined advances have brought OSCs closer to commercial viability.

Nevertheless, several critical challenges remain. Achieving and maintaining optimal morphology over time is difficult, as thermal fluctuations and mechanical stress can lead to phase segregation or crystallization. Furthermore, controlling the domain size and interfacial distribution with reproducibility remains a bottleneck, particularly for large-area or roll-to-roll fabrication.[20] There is also a pressing need to improve the environmental sustainability of OSC fabrication processes, especially regarding solvent toxicity and material waste.[21] Overall, addressing these challenges requires integrated

doi:10.6342/NTU202502276

approaches that combine molecular design and process engineering—precisely the dual focus of the present research.

1.3 All-Polymer Solar Cells (All-PSCs)

1.3.1 Introduction to All-Polymer Solar Cells

All-polymer solar cells (All-PSCs) are a sub-class of OSCs in which both the electron donor and acceptor are conjugated polymers.[22, 23] This unique configuration offers distinct advantages over traditional polymer : small molecule systems, including enhanced mechanical flexibility, improved thermal stability, and compatibility with scalable solution-processing techniques.[24] These features make All-PSCs highly attractive for emerging applications such as wearable electronics and roll-to-roll photovoltaics.

However, despite these benefits, the development of All-PSCs is challenged by issues related to phase separation and morphology control. The polymeric nature of both donor and acceptor components often leads to large, entangled domains and poor miscibility, which hinder efficient exciton dissociation and charge transport.[25] These morphological challenges highlight the need for specialized materials and finely tuned processing strategies, both of which are addressed in the subsequent sections.

1.3.2 Evolution of Polymer Acceptors

The success of All-PSCs relies heavily on the advancement of high-performance polymer acceptors. Early attempts using perylene diimide (PDI), naphthalene diimide (NDI), and diketopyrrolopyrrole (DPP)-based acceptors often suffered from narrow

doi:10.6342/NTU202502276

absorption windows, high energy losses, and low carrier mobility.[26] These limitations restricted the efficiency and stability of early All-PSC devices.

A turning point in polymer acceptor development came with the introduction of Y6-based structures. As illustrated in **Figure 1-5**, the evolution of conjugated polymer acceptors reached a major breakthrough with the polymerization of Y6-type small-molecule acceptors into polymerized small-molecule acceptors (PSMAs).[27, 28] Among these, materials such as PY-IT and PJ1 have demonstrated strong absorption, excellent energy-level alignment with common donor polymers like PM6, and superior morphological compatibility, pushing device efficiencies beyond 17%.[29]

1.3.3 PSMA-Type Acceptors: From Concept to Application

PSMAs are designed by polymerizing high-performing non-fullerene small-molecule acceptors (SMAs), retaining their favorable optical and electronic properties while improving processability and morphological control. Compared to traditional SMAs, PSMAs offer better film-forming properties, additional electron-transporting channels, and enhanced thermal and photostability. Furthermore, their polymeric nature helps reduce diffusion-driven phase instability, a common degradation mechanism in OSCs.[30]

As shown in **Figure 1-6**, the regularity of PSMA backbones contributes to improved solid-state packing and reduced energetic disorder, which are essential for high device performance.[31] Importantly, the compatibility of PSMA-type acceptors with polymer donors leads to more homogeneous active layers, enabling better charge separation and reduced recombination losses. These features have made PSMA-based systems a central focus in the design of next-generation All-PSCs.

doi:10.6342/NTU202502276

1.3.4 Outlook and Remaining Challenges

While the use of PSMAs such as PY-IT has enabled significant progress in All-PSCs, further optimization is still required to fully realize their potential. Central to this effort is the control of active layer morphology, which remains a major bottleneck. Achieving finely interpenetrating donor–acceptor networks, maintaining nanoscale domain sizes, and optimizing chain orientation all require a delicate balance between molecular design and processing conditions. Although various strategies such as additive engineering, solvent selection, and post-processing techniques have been proposed, a unified understanding of how these methods influence the microstructure and performance of All-PSCs remains limited. These considerations will be explored in greater detail in the following section, which focuses specifically on the role of morphology and material design in high-performance OSCs and All-PSCs.

1.4 Morphology and Material Design in Organic Solar Cells

The efficiency and stability of organic solar cells (OSCs)—including all-polymer solar cells (All-PSCs)—are deeply influenced by the morphological structure of the active layer and the intrinsic properties of the materials that comprise it. These two aspects are not independent; instead, they are intrinsically linked: the molecular structure of donor and acceptor materials largely determines how they self-assemble, phase separate, and ultimately influence charge dynamics within the bulk heterojunction (BHJ). Understanding and engineering both the morphology and material design of OSCs is therefore fundamental to achieving high-performance devices.

doi:10.6342/NTU202502276

1.4.1 Donor–Acceptor Design and Intramolecular Charge Transfer

A central strategy in molecular design for OSCs is the donor–acceptor (D–A) architecture, where electron-rich (donor) and electron-deficient (acceptor) segments are alternated along the polymer backbone.[32] This design creates a "push–pull" electronic structure, promoting intramolecular charge transfer (ICT) upon photoexcitation.[33] As illustrated in **Figure 1-7**, classical A-D-A small-molecule acceptors like ITIC feature a single donor flanked by two acceptors, while more advanced structures like Y6 adopt an A-D-A’-D-A configuration.[33] This further enhances the delocalization of electrons along the conjugated backbone and strengthens the ICT effect.[34]

Such ICT behavior plays a critical role in improving light absorption, energy level alignment, and exciton dissociation. It facilitates the generation of low-binding-energy excitons and enhances charge carrier mobility by increasing orbital overlap.[34] In the context of polymer materials, incorporating this D–A concept into backbone design—through alternating electron-donating and electron-withdrawing moieties—can significantly influence molecular packing, crystallinity, and energy levels.

1.4.2 Morphological Requirements for Efficient Charge Generation

In OSCs, the morphology of the BHJ layer must be carefully controlled to ensure that all key photophysical processes—light absorption, exciton diffusion, charge separation, and charge transport—occur with high efficiency. A well-structured morphology includes nanoscale phase separation between donor and acceptor domains, ideally in the range of 10 to 20 nm, which matches the typical exciton diffusion length.[35] If domains are too large, excitons may recombine before reaching a D/A

doi:10.6342/NTU202502276

interface. Conversely, excessive miscibility leading to overly fine or mixed domains can hinder charge percolation pathways, causing recombination or carrier trapping.

Equally important is the molecular orientation within the film. A face-on alignment, where π–π stacking occurs perpendicular to the substrate, is generally preferred in inverted device architectures because it facilitates vertical charge transport toward the electrodes.[36] Moreover, crystallinity and domain purity affect both mobility and energetic disorder. Films with high crystallinity and well-defined domains exhibit lower trap densities, enabling better carrier extraction and reduced recombination losses.[37]

In all-polymer systems, achieving this optimal morphology is more complex due to the high molecular weight and rigid chain structure of both donor and acceptor materials.[38] Therefore, both molecular structure and processing techniques must work in concert to tailor the BHJ morphology.

1.4.3 Molecular Design Strategies in OSCs

Molecular design directly impacts the morphology and functionality of the active layer. Side-chain engineering is one of the most widely used strategies to manipulate solubility, aggregation, and molecular packing, as shown in **Figure 1-8**.[39, 40] For example, branched alkyl chains improve solubility but may induce excessive torsional strain that disrupts backbone planarity.[41] In contrast, hybrid or asymmetric side chains—such as siloxane-terminated alkyl chains combined with alkyl chains—can enhance solubility while preserving or even promoting π–π stacking.[42]

In parallel, backbone fluorination is another effective strategy to modulate morphology and electronic properties. The incorporation of fluorine atoms enhances the electron-withdrawing strength of the backbone, deepens the highest occupied molecular

doi:10.6342/NTU202502276

orbital (HOMO) energy level, and introduces non-covalent interactions (e.g., F⋯S), which rigidify the backbone and promote chain ordering, as shown in **Figure 1-9**.[43-45] These effects not only improve charge mobility and reduce energetic disorder but also lead to more thermally stable morphologies—an essential factor for long-term device operation. Collectively, these molecular design strategies demonstrate how chemical structure can be used to precisely control morphology, energetics, and electronic function within the active layer.

1.4.4 Processing Control via Solvent and Additive Engineering

While material design defines the intrinsic potential of a polymer, processing conditions determine how that potential manifests in the solid state. Among various techniques, solvent engineering and additive incorporation have emerged as highly effective means to control morphology during film formation.[46, 47]

The use of high-boiling-point co-solvents delays solvent evaporation and allows extended molecular self-assembly time.[48] This results in improved molecular packing, reduced phase separation scale, and enhanced donor–acceptor miscibility. Volatile solid additives can also offer further advantages. Unlike high-boiling liquid additives, solid additives evaporate cleanly during annealing, leaving a residue-free active layer, as shown in **Figure 1-10**.[49] They act as transient structure-directing agents that enhance crystallinity, promote intermolecular interactions, and suppress trap formation.[50] Together with co-solvents, they enable fine control over morphology, leading to improved fill factors, higher short-circuit current, and overall better device performance.

These methods are especially critical in all-polymer systems, where both components are rigid and prone to phase segregation. Without careful processing control, the miscibility and morphology of polymer : polymer blends often fall outside the optimal window for efficient exciton dissociation and charge transport.

1.5 Research Objectives

Organic solar cells (OSCs) have garnered widespread attention as a promising alternative energy technology due to their inherent advantages of mechanical flexibility, lightweight nature, solution processability, and compatibility with large-area and flexible device architectures. Among various OSC platforms, all-polymer solar cells (All-PSCs)—which employ conjugated polymers as both electron donors and acceptors—have emerged as a next-generation photovoltaic architecture with the potential to deliver enhanced thermal stability, mechanical robustness, and long-term operational reliability. Over the past decade, significant advancements in material design and device engineering have led to All-PSCs achieving power conversion efficiencies (PCEs) exceeding 17%, approaching the performance of traditional polymer : non-fullerene small molecule systems.

Despite this progress, two major challenges persist in the development of high-efficiency and scalable OSC technologies. First, on the molecular design level, conventional conjugated polymers often suffer from suboptimal crystallinity, limited molecular packing, and unfavorable face-on alignment, all of which hinder efficient charge transport. In particular, designing polymers that balance solubility with backbone planarity and controlled aggregation remains difficult. Second, on the processing level, controlling phase separation and domain size during active layer formation remains a bottleneck, especially in All-PSC systems where donor–acceptor (D/A) miscibility is inherently difficult to manage due to the polymeric nature of both

doi:10.6342/NTU202502276

components. To address these limitations, this study adopts a dual-strategy approach—combining molecular structure engineering and green solvent processing design—to systematically explore and optimize the morphological, optoelectronic, and photovoltaic characteristics of OSCs.

i Mitigating Side-Chain Effects in Isoindigo-Based Polymer Donors through Backbone Fluorination for Enhanced Photovoltaic Performance

In **Chapter 2**, we investigate a series of isoindigo-based (IID) donor–acceptor conjugated polymers engineered with two key structural motifs: (i) asymmetric side chains to promote intermolecular dipole moments and controlled packing behavior, and (ii) backbone fluorination to enhance backbone coplanarity and reduce torsional disorder. Six polymers (**P1–P6**) were synthesized, incorporating various side-chain asymmetries and fluorinated bithiophene units. The results reveal that asymmetric side chains induce a face-on-dominated packing orientation and improve π–π stacking, leading to enhanced charge dissociation, more balanced carrier transport, and higher PCEs. Moreover, backbone fluorination was shown to mitigate the negative effects of flexible side chains by rigidifying the backbone structure, improving crystallinity, and narrowing the performance gap between symmetric and asymmetric variants. These findings demonstrate that synergistic structural engineering at the molecular level offers a viable route to optimize morphology and boost the efficiency of polymer donor systems.

ii Morphology-Controlled All-Polymer Solar Cells Enabled by Mixed Green Solvent Strategy

In **Chapter 3**, we focus on morphology control through green solvent engineering in All-PSC systems, using the PM6:PY-IT polymer blend as a model. A systematic study was conducted using mixed-solvent systems composed of chloroform (CF) partially replaced with eco-friendly co-solvents—tetrahydrofuran (THF), 2-methyltetrahydrofuran (2-MeTHF), and 3-methyltetrahydrofuran (3-MeTHF)—combined with a volatile solid additive, DTT. The high boiling points of these co-solvents enable slower film drying and longer molecular self-assembly time, leading to better miscibility, smaller and more controlled domain sizes, and enhanced molecular ordering. Devices processed with THF- and 2-MeTHF-based systems exhibited over 17% PCE, driven by improved light absorption, more balanced carrier mobility, suppressed trap-assisted recombination, and reduced energetic disorder, as evidenced by TRPL, SCLC, TPV/TPC, and Urbach energy analyses. Importantly, this strategy offers not only record-high performance in both binary and ternary devices, but also an environmentally responsible and scalable pathway toward sustainable OSC manufacturing.

doi:10.6342/NTU202502276

Figures

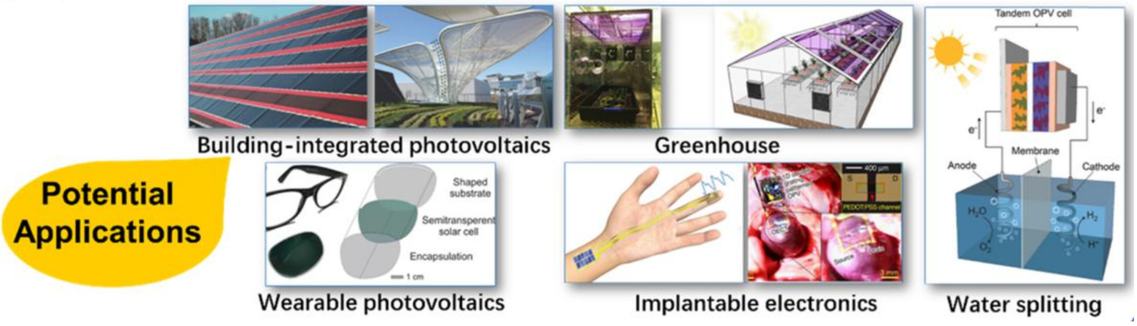

Figure 1-1 Future applications of organic solar cells in sustainable systems.

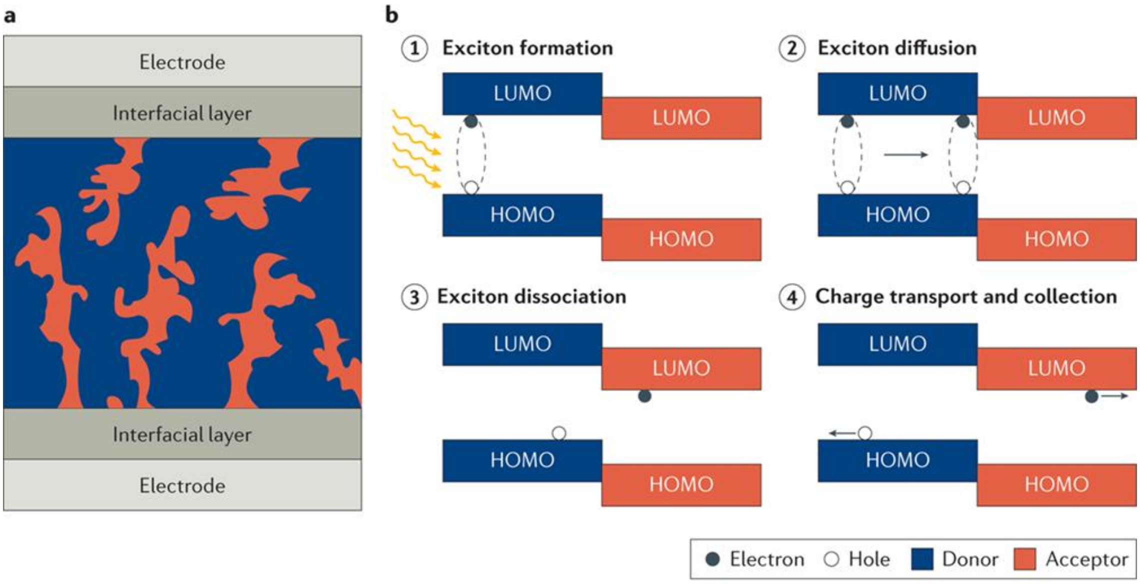

Figure 1-2 Schematic illustration of exciton dynamics and charge transport in bulk heterojunction OPVs.

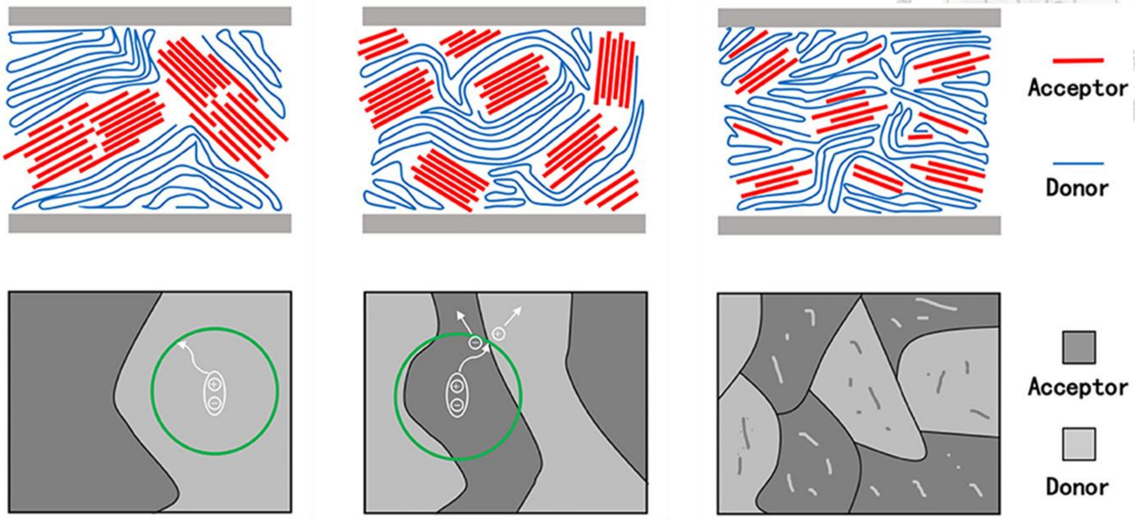

Figure 1-3 Correlation between nano-morphology and exciton dynamics in donor–acceptor blends.

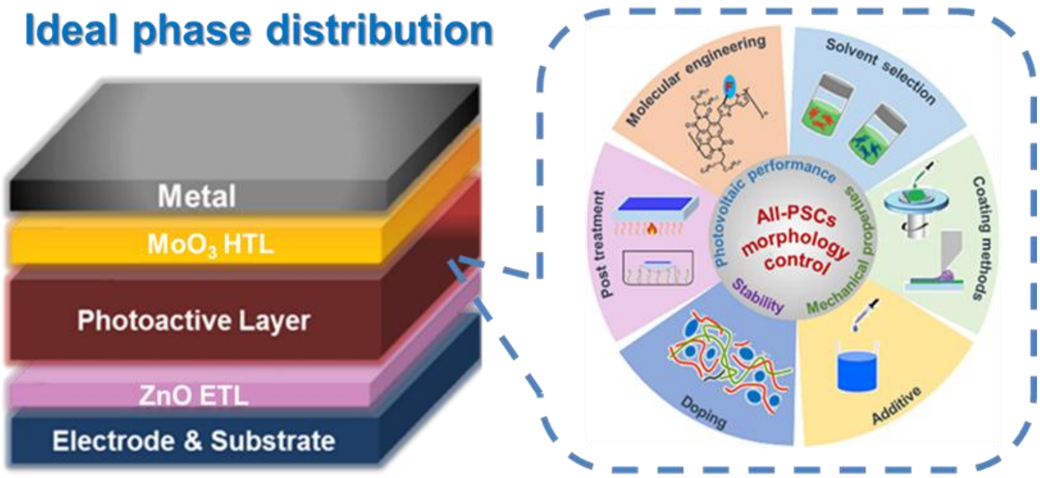

Figure 1-4 Morphology control strategies for optimized phase distribution in organic solar cells.

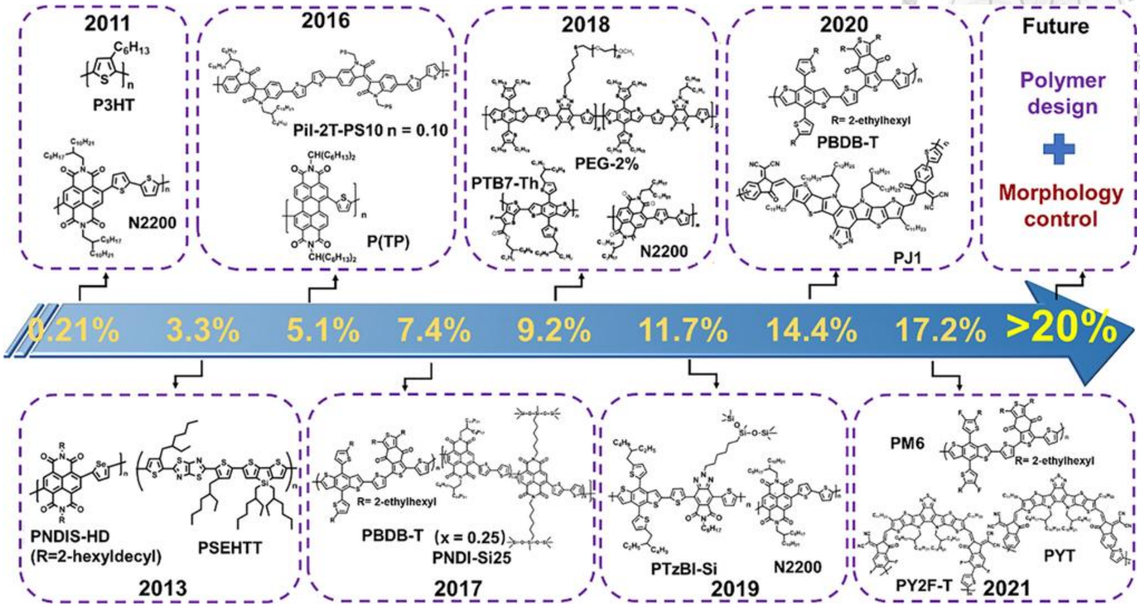

Figure 1-5 Evolution of polymer donors and acceptors toward >20% efficiency in all-polymer solar cells.

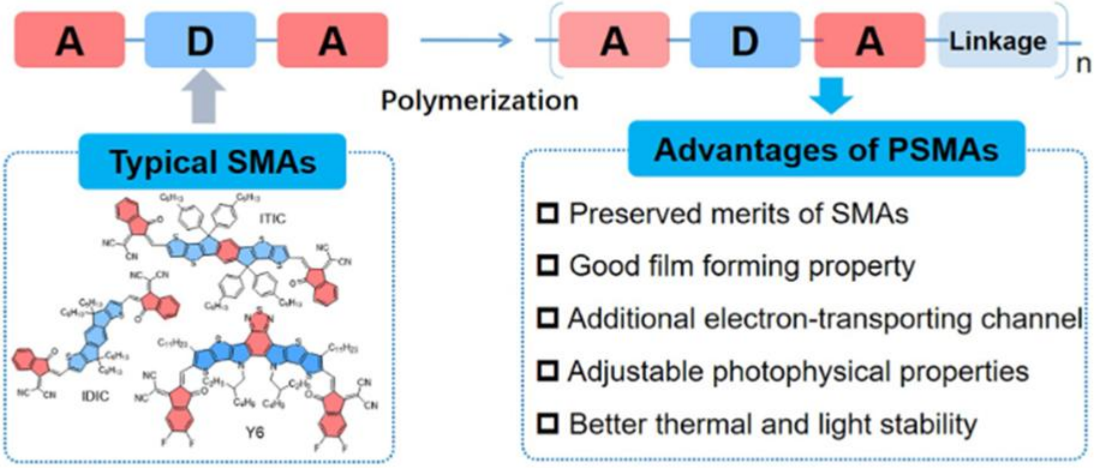

☐ Preserved merits of SMAs
☐ Good film forming property
☐ Additional electron-transporting channel
☐ Adjustable photophysical properties
☐ Better thermal and light stability

Figure 1-6 Design and advantages of polymerized small molecule acceptors for high-performance OPVs.

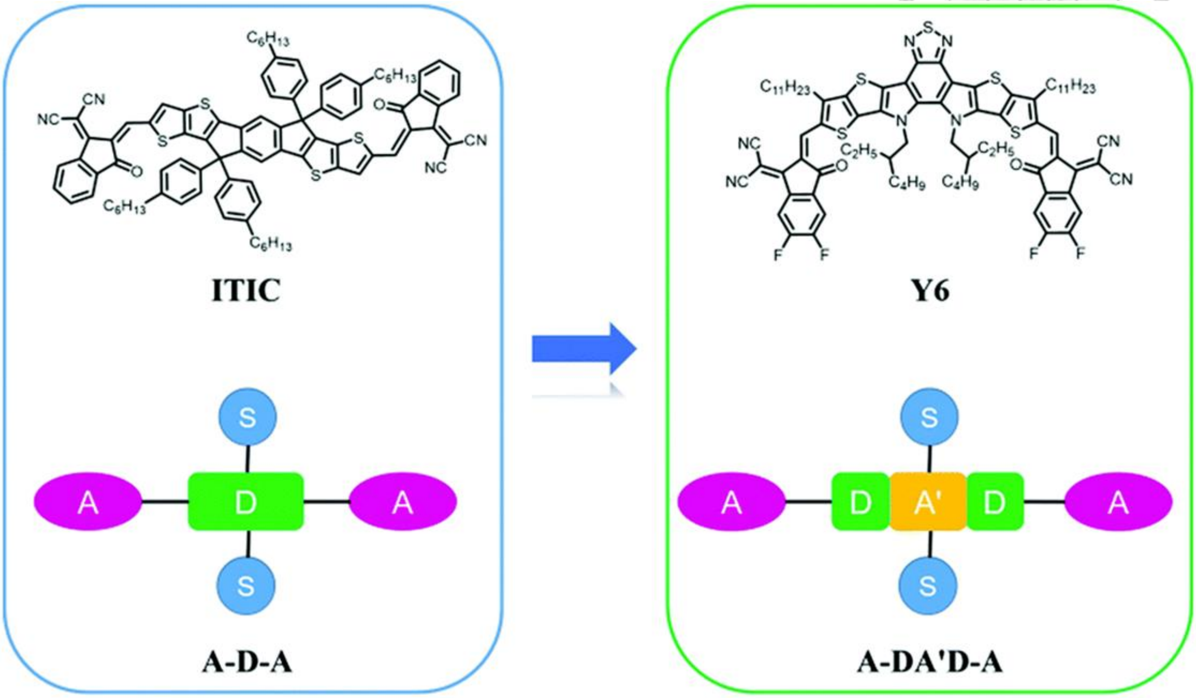

Figure 1-7 Molecular evolution of non-fullerene acceptors: from A-D-A to A-DA′D-A structures.

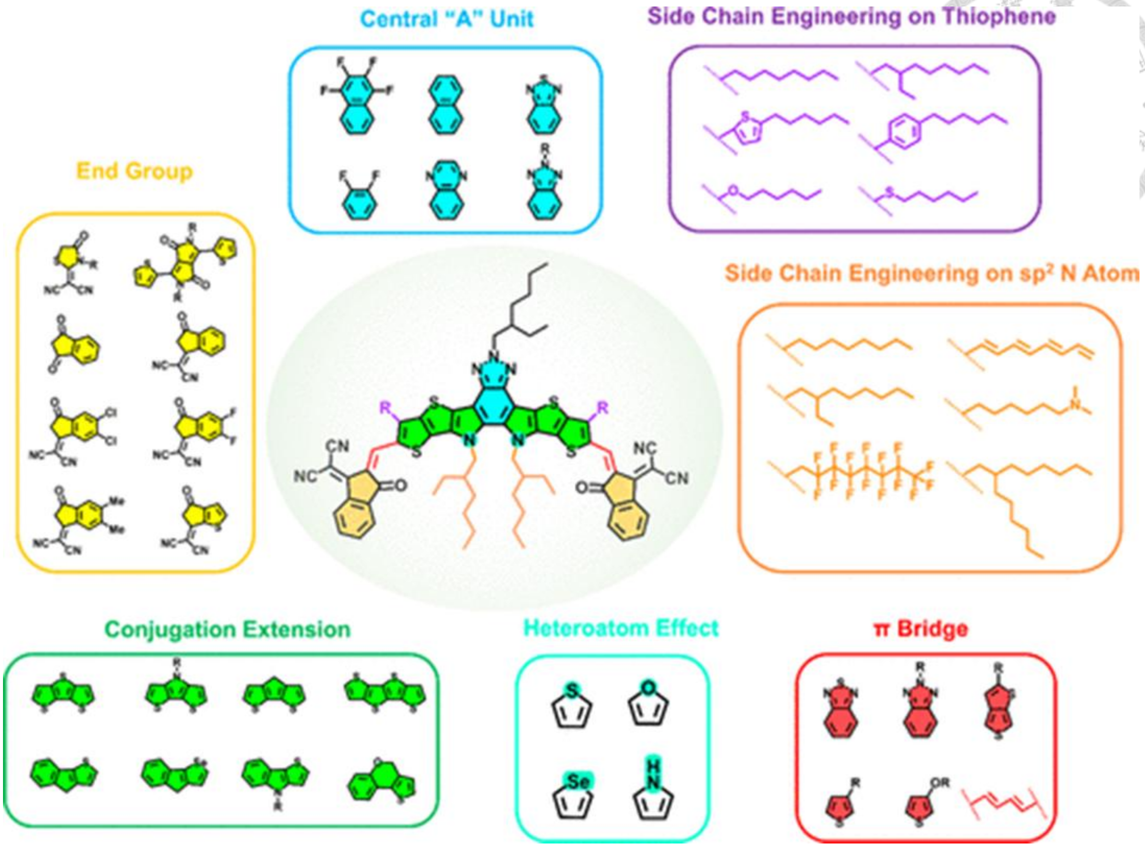

Figure 1-8 Rational design of non-fullerene acceptors: functional group engineering from core to periphery.

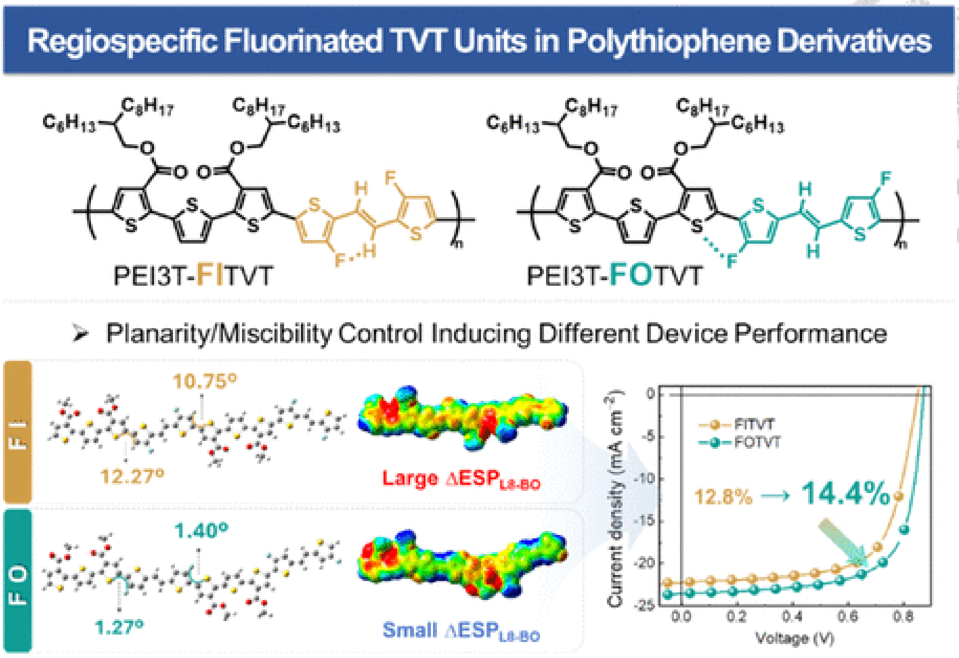

Figure 1-9 Fluorination-controlled planarity and performance in TVT-containing donor polymers for OPVs.

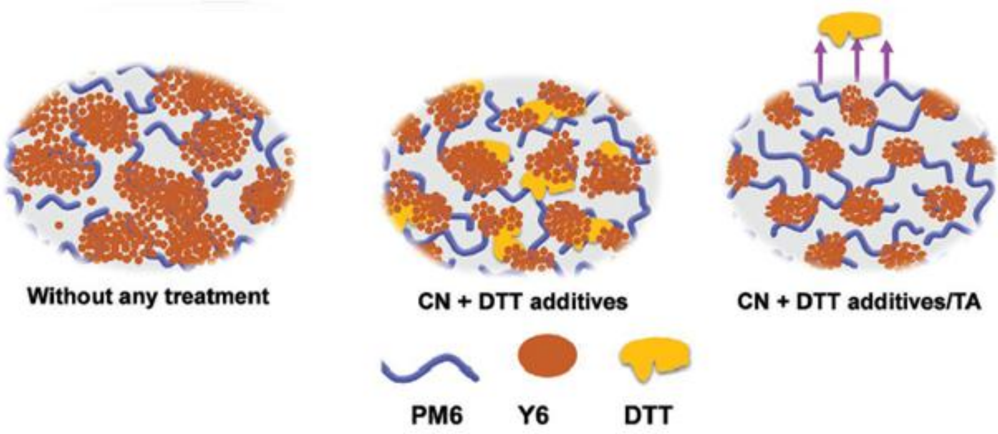

Figure 1-10 Morphology control via volatile solid additives for residue-free organic solar cell active layers.

CHAPTER 2

Mitigating Side-Chain Effects in Isoindigo-Based Polymer Donors through Backbone Fluorination for Enhanced Photovoltaic Performance

2.1 Introduction

In the past decade, organic solar cells (OSCs) have garnered significant interest within the photovoltaic research community, owing to their numerous advantages such as lightweight nature, excellent mechanical flexibility, cost-effective solution-based fabrication, and strong potential for large-scale manufacturing.[51–55] Thanks to ongoing advancements in the molecular design of photoactive components and progressive device engineering, the power conversion efficiency (PCE) of polymer solar cells (PSCs) has now reached nearly 19%, setting new performance records.[56, 57] Among the various structural strategies employed in polymer development, donor–acceptor (D–A) type conjugated polymers have emerged as a leading class of materials, primarily due to their easily tunable chemical structure and adaptable optoelectronic characteristics.[58–61]

Due to the greater synthetic complexity, the development of novel electron-deficient building blocks has progressed more slowly than that of electron-rich counterparts. To date, the majority of reported electron-deficient units have been primarily based on structures such as diketopyrrolopyrrole (DPP), perylene diimide

doi:10.6342/NTU202502276

(PDI), naphthalene diimide (NDI), and isoindigo (IID).[62–65] Among the various polymer systems, IID-based copolymers are of particular interest due to the advantageous properties of the IID unit, including its strong electron-withdrawing nature, efficient molecular packing behavior, and its derivation from naturally occurring plant sources.[66–69] Additionally, the chemical structure of IID can be readily modified. For instance, a range of side-chain modifications have been employed on IID-based copolymers to enhance their photovoltaic efficiency.[70–73] Tailoring unconjugated alkyl or siloxane-terminated side chains—such as adjusting their type, length, shape, or branching location—has proven effective in manipulating molecular packing and thin-film morphology.[71, 74] Nevertheless, while long and branched alkyl side chains can improve polymer solubility, their high flexibility may disrupt backbone planarity, which can hinder intermolecular packing and charge transport.[75] Notably, it has been recently shown that incorporating highly branched hybrid siloxane-terminated side chains can improve the solubility of conjugated polymers without significantly disrupting their intermolecular stacking behavior.[76–79] Furthermore, Méry et al. reported the use of linear siloxane hybrid side chains, which were found to markedly promote π–π stacking between polymer chains. This enhancement in molecular interaction leads to improved charge carrier mobility.[80]

In conclusion, this study systematically investigated and compared the photovoltaic performance of six IID-based polymer donors featuring subtle variations in side-chain architecture and backbone fluorination, each paired with the non-fullerene acceptor **ITIC-4F** (**Figure 2-1**). Specifically, the isoindigo (IID) unit was coupled with either a bithiophene (BT) or a fluorinated bithiophene segment to synthesize two polymer series: PII2T (**P1–P3**) and PII2TF (**P4–P6**), as illustrated in **Figure 2-2**. The polymers incorporate either symmetric or asymmetric side-chain combinations

doi:10.6342/NTU202502276

composed of a decyltetradecyl (DT) branched alkyl group and a siloxane-terminated side chain (SiO–C8).[69]

Our initial findings demonstrated that **P2** and **P5**, which incorporate asymmetric side chains, achieved the highest PCEs within the PII2T and PII2TF series, respectively. Their enhanced performance is attributed to the mismatched geometry of the side chains, which facilitates more efficient interchain packing. Additionally, asymmetric side chains generate a greater dipole moment compared to symmetric ones, thereby reinforcing intermolecular interactions.[85] We further observed that, beyond outperforming the non-fluorinated polymers (**P1–P3**), the fluorinated variants (**P4–P6**) exhibited a diminished performance gap between polymers bearing symmetric and asymmetric side chains. This effect is linked to the fluorinated backbone, which induces noncovalent F···S interactions at the thiophene units. These interactions serve to stiffen the polymer backbone in PII2TF, leading to improved crystallinity and molecular ordering. They also enhance intermolecular cohesion and help mitigate the torsional stress introduced by the side chains. Consequently, the influence of side-chain configuration on device performance is significantly reduced.

2.2 Experimental Section

2.2.1 Materials

The polymer donors **P1–P6** were synthesized following procedures reported in our previous study.[69] The non-fullerene acceptor **ITIC-4F** was obtained from 1-Material, and all solvents were sourced from Sigma-Aldrich and used as received, without additional purification.

doi:10.6342/NTU202502276

2.2.2 Device Fabrication and Characterization

The solar cell devices were constructed using an inverted architecture comprising ITO glass/ZnO/BHJ layer/MoO$_3$/Ag. Initially, ITO-coated glass substrates were cleaned by sequential ultrasonication in detergent, deionized water, acetone, and isopropyl alcohol, each for 15 minutes. After cleaning, the substrates were dried under a nitrogen stream and subjected to plasma treatment for 8 minutes. The ZnO electron transport layer was deposited by spin-coating at 4000 rpm for 30 seconds using a precursor solution composed of 0.1 g zinc acetate dissolved in 1 mL of 2-methoxyethanol with 28 μL of ethanolamine. The coated substrates were first annealed at 80 °C for 10 minutes inside a glove box, followed by a second annealing step at 180 °C for 30 minutes in ambient air. Active layer precursor solutions were prepared at a concentration of 18 mg/mL in chloroform without any processing additives. The donor-to-acceptor weight ratio was optimized at 1:1.2. These solutions were stirred overnight at 50 °C inside a glove box to ensure full dissolution. The active layer was then spin-coated onto the ZnO-coated substrates at 3000 rpm for 60 seconds. Following this, 10 nm of MoO$_3$ and 100 nm of Ag were thermally evaporated sequentially under high vacuum conditions (<10^{-6} Torr) to complete the device. The defined active area for each device was 8.5 mm^2.

The current–voltage (*J*–*V*) characteristics of the solar cells were measured under AM1.5G simulated sunlight (100 mW cm^{-2}) using a Keithley 2400 source-measure unit (SMU) controlled by computer software. Illumination was provided by a SS-F5-3A solar simulator from Enlitech Co., Ltd., and calibrated using a silicon photodiode equipped with a KG-5 filter. External quantum efficiency (EQE) spectra were recorded using a QE-R measurement system (Enlitech Co., Ltd.) under illumination from monochromatic light sourced from a xenon lamp. Light intensity across the 300–1000 nm wavelength range was calibrated using a standard single-crystal silicon reference cell. Surface morphology of the active layers was characterized via atomic force microscopy (AFM) operated in tapping mode using a MultiMode system equipped with a Nanoscope 3D controller (Digital Instruments) at room temperature. Grazing-incidence wide-angle X-ray scattering (GIWAXS) measurements were conducted at beamline BL17A1 at the National Synchrotron Radiation Research Center (NSRRC), Taiwan, using an X-ray wavelength of 1.322 Å and an incident angle of 0.25°. UV–visible absorption spectra were acquired using a Hitachi U-4100 spectrophotometer.

2.2.3 Space Charge Limited Current (SCLC) Measurement

The charge transport characteristics of the **P1–P6** blend films were evaluated using the space-charge-limited current (SCLC) technique. Hole-only devices were constructed with the architecture: ITO glass/PEDOT:PSS/BHJ layer/MoO_3/Ag, while electron-only devices followed the configuration: ITO glass/ZnO/BHJ layer/TPBi/LiF/Ag. Carrier mobilities (both hole and electron) were extracted using the Mott–Gurney law, which is expressed as: $J = (9\varepsilon_0\varepsilon_r\mu V^2)/(8L^3)$, where J is the current density, V is the applied voltage, ε_0 is the vacuum permittivity (8.85×10^{-12} F/m), ε_r is the relative dielectric constant of the photoactive material, μ is the carrier mobility, and L is the thickness of the active layer (BHJ). For organic semiconductors, ε_r typically ranges between 2 and 4; in this work, a value of 3 was assumed. The BHJ film thickness was approximately 100 nm.

2.3 Results and Discussion

2.3.1 Optical and Electrochemical Properties

The molecular weights of the six IID-based polymers, as determined by gel permeation chromatography (GPC) using THF as the eluent, are referenced from our earlier publication,[69] with relevant characteristics summarized in **Table 2-1**. The number-average molecular weights (*Mn*) for **P1** through **P6** are reported as 200, 168, 197, 143, 146, and 182 kDa, respectively, accompanied by polydispersity index (PDI) values of 1.30, 2.34, 1.27, 1.50, 3.27, and 1.38. These results indicate that all six polymers exhibit relatively high molecular weights and favorable dispersity. **Figures 2-1b** and **2-1c** present the normalized UV–vis absorption spectra of thin films composed of the IID-based polymers. Each of the **P1–P6** films displays broad absorption features, with distinct peaks appearing in the ranges of 350–450 nm and 650–750 nm. The absorption within 350–450 nm corresponds to π–π^* transitions along the polymer backbone, whereas the bands observed between 650–750 nm arise from intramolecular charge transfer (ICT) between donor and acceptor segments. Owing to their structurally similar conjugated backbones, all polymers exhibit comparable optical band gaps (*Eg*) of approximately 1.6 eV, calculated from the onset of absorption. The peak absorption wavelengths for **P1** through **P6** are 700, 706, 714, 703, 711, and 716 nm, respectively. Notably, the fluorinated **P4–P6** films show slightly red-shifted maximum absorption peaks relative to the non-fluorinated **P1–P3** counterparts. This red shift is attributed to improved backbone coplanarity in PII2TF over PII2T. Fluorination enhances the structural planarity of the polymer backbone, thereby intensifying intermolecular interactions. These stronger interactions promote denser and more orderly chain packing.

The frontier molecular orbital energy levels of the six IID-based polymers were determined using cyclic voltammetry (CV) and are referenced from our earlier study, with the results presented in **Figure 2-1d**.[19] The measured highest occupied molecular orbital (HOMO) energy levels for **P1** to **P6** were −5.40, −5.35, −5.26, −5.52, −5.53, and −5.49 eV, respectively. The corresponding lowest unoccupied molecular orbital (LUMO) energy levels, calculated using the formula LUMO = HOMO + *Eg*, were found to be −3.77, −3.76, −3.65, −3.88, −3.94, and −3.87 eV. A trend is evident in which the HOMO and LUMO levels shift upward progressively from **P1** to **P3**. A similar upward shift is observed for **P6** when compared to **P4** and **P5**. These findings suggest that increasing the proportion of siloxane-terminated side chains in both PII2T and PII2TF enhances the electron-donating character of the polymers, resulting in elevated energy levels. Importantly, due to the strong electron-withdrawing nature of fluorine, the fluorinated polymers **P4–P6** exhibit lower HOMO and LUMO levels compared to their non-fluorinated counterparts (**P1–P3**). This deeper energy alignment contributes to the higher open-circuit voltage (V_{oc}) observed in the solar cells fabricated from **P4–P6**.

2.3.2 Photovoltaic Performance

To investigate the combined effect of asymmetric side chains and backbone fluorination on photovoltaic performance, inverted solar cell devices were fabricated using **P1–P6** as polymer donors, with **ITIC-4F** employed as the non-fullerene acceptor (NFA), as illustrated in **Figure 2-1e**. The detailed fabrication procedures are provided in the Experimental Section. **Figures 2-3a** and **2-3b** display the current density–voltage (*J*–*V*) characteristics of the fabricated devices, and the corresponding photovoltaic parameters—including open-circuit voltage (V_{oc}), short-circuit current density (J_{sc}), and fill factor (*FF*)—are summarized in **Table 2-2**. The influence of side-chain architecture on device performance is particularly evident in the **P1–P3** series. A downward trend in V_{oc} was observed from **P1** to **P3**, which correlates with the progressive upward shift of their HOMO energy levels (**Figure 2-1d**). Among them, **P2**, which features asymmetric SiO–C8/DT side chains, achieved the highest power conversion efficiency (PCE) of 4.412%, accompanied by a V_{oc} of 0.88 V, a J_{sc} of 9.12 mA cm^{-2}, and a *FF* of 57.4%. This represents a significant improvement over **P1** (PCE: 1.16%) and **P3** (PCE: 3.22%), both of which contain symmetric side chains. The enhanced performance of **P2** is attributed to its asymmetric side-chain geometry, which will be discussed in further detail in a later section. Conversely, the lowest efficiency observed for the **P1**-based device is likely linked to the high flexibility of its DT side chains, which can induce greater torsional strain and disrupt optimal molecular packing.[75] These findings underscore the critical impact of side-chain structure on photovoltaic performance and emphasize the performance advantage offered by asymmetric side-chain engineering.

Importantly, incorporating fluorine atoms into the polymer backbone led to further enhancement in photovoltaic performance. As illustrated, devices based on the fluorinated polymers **P4–P6** consistently exhibited higher PCEs than those derived from their non-fluorinated counterparts **P1–P3**. This improvement can be attributed to the deeper HOMO energy levels of **P4–P6** (**Figure 2-1d**), which contributed to higher V_{oc} across all fluorinated devices. A downward trend in V_{oc} was also observed from **P4** to **P6**, corresponding to the increasing proportion of SiO–C8 side chains. Notably, **P5**—featuring asymmetric SiO–C8/DT side chains—achieved the highest PCE of 4.52%, along with a V_{oc} of 0.96 V, a J_{sc} of 8.18 mA cm^{-2}, and a *FF* of 57.1%, outperforming both **P4** (PCE: 3.66%) and **P6** (PCE: 3.80%), which bear symmetric side chains. These findings once again validate the performance benefits of asymmetric

doi:10.6342/NTU202502276

side-chain engineering. Moreover, when comparing **P4** with the non-fluorinated **P1**, the fluorinated polymer demonstrated nearly a threefold increase in PCE, along with notable improvements in V_{oc}, J_{sc}, and FF. This significant enhancement is likely due to the more rigid backbone geometry of PII2TF, which effectively mitigates the torsional effects introduced by flexible DT side chains. A similar, though more modest, improvement was observed when comparing P6 to its non-fluorinated analog, **P3**.

In addition, it is well established that the potential loss (ΔE_{loss}) of a solar cell is directly related to its V_{oc}, and can be calculated using the expression $\Delta E_{loss} = Eg - qV_{oc}$. A comparison of ΔE_{loss} and corresponding V_{oc} values for both non-fluorinated (**P1–P3**) and fluorinated (**P4–P6**) devices is presented in **Figure 2-4**. As evident from the data, all fluorinated devices (**P4–P6**) exhibit lower ΔE_{loss} values than their non-fluorinated counterparts (**P1–P3**), suggesting reduced energy losses. Furthermore, within each series, devices based on **P2** and **P5**—featuring asymmetric side chains—achieved the lowest ΔE_{loss} values, reinforcing the performance benefit of asymmetric side-chain design in minimizing potential loss. **Figure 2-5** illustrates the PCEs of the same set of devices, further confirming that backbone fluorination diminishes the influence of side-chain variation on overall photovoltaic performance. This effect can be attributed to the formation of more extensive crystalline domains in the polymer films, induced by backbone fluorination—a topic that will be elaborated upon in the morphological analysis section.

Figures 2-3c and **2-3d** display the external quantum efficiency (EQE) spectra of the devices based on **P1–P3** and **P4–P6**, respectively. Among the non-fluorinated polymers, **P2** and **P3** devices demonstrated significantly higher EQE responses across the 300–850 nm range compared to **P1**, aligning with their superior J_{sc} values. In contrast, the fluorinated devices (**P4–P6**) showed similar EQE profiles over the same spectral range, with peak EQE values reaching 38%, 40%, and 45% for **P4**, **P5**, and **P6**, respectively. This uniformity in EQE among fluorinated polymers further supports the conclusion that backbone fluorination minimizes the performance variability caused by differences in side-chain architecture.

2.3.3 Charge Recombination and Transport Properties

To further investigate the charge dissociation characteristics of these devices, we analyzed the relationship between photocurrent density (J_{ph}) and effective voltage (V_{eff}), as illustrated in **Figures 2-6a** and **2-6b**.[76, 77] The photocurrent density, J_{ph}, was determined using the equation $J_{ph} = J_L - J_D$, where J_L represents the current density under AM1.5G illumination, and J_D corresponds to the dark current density. The effective voltage, V_{eff}, is defined as $V_{eff} = V_0 - V_{bias}$, where V_0 is the voltage at which J_{ph} equals zero, and V_{bias} is the externally applied bias. Typically, J_{ph} reaches a saturation level (J_{sat}) at high V_{eff}, indicating that photogenerated charge carriers are fully dissociated and efficiently collected at the electrodes due to the strong internal electric field. Therefore, the ratio J_{ph}/J_{sat} serves as an indicator of the charge dissociation probability under a specific bias condition. However, since none of the six devices achieved full saturation (J_{sat}) at V_{eff} = 1 V, likely due to suboptimal exciton dissociation, we used J_a—the J_{ph} value at V_{eff} = 1 V—as a practical approximation in place of J_{sat}. This provides a reasonable estimate for assessing charge dissociation efficiency. At V_{eff} = 0.1 V, the calculated J_{ph}/J_a ratios for **P1** through **P6** were 0.233, 0.454, 0.279, 0.34, 0.551, and 0.331, respectively. These results show that **P2** and **P5**, both incorporating asymmetric SiO–C8/DT side chains, exhibited the highest charge dissociation efficiencies compared to their symmetric analogs. Additionally, the fluorinated

doi:10.6342/NTU202502276

polymers **P4–P6** demonstrated greater charge dissociation than the non-fluorinated series **P1–P3**.

To further understand charge recombination dynamics, the dependence of the device's short-circuit current density (J_{sc}) on incident light intensity within the range of 10–100 mW cm^{-2} was examined. The relationship between J_{sc} and light intensity (P_{light}) typically follows a power-law form, expressed as $J_{sc} \propto (P_{light})^{\alpha}$, where α denotes the exponential fitting parameter.[94, 95] Generally, an α value approaching 1 suggests minimal bimolecular (non-geminate) recombination within the device. Since bimolecular recombination is recognized as a key loss pathway in OSCs,[96] minimizing this recombination mechanism is critical for improving device efficiency. From the slopes extracted in **Figures 2-8c** and **2-8d**, the α values for devices **P1** through **P6** were determined to be 0.81, 0.98, 0.90, 0.93, 0.98, and 0.94, respectively. Notably, **P2** and **P5**—both incorporating asymmetric SiO–C8/DT side chains—showed α values close to unity, indicating minimal bimolecular recombination. These findings once again emphasize the beneficial effect of asymmetric side-chain architecture on device performance and help explain the high *FF* values observed for both **P2** and **P5**. Additionally, the fluorinated **P4** device exhibited a significantly higher α value compared to its non-fluorinated counterpart **P1**, supporting the conclusion that backbone fluorination helps suppress recombination and mitigates the performance variation caused by different side-chain configurations.

The charge recombination behavior of these devices is also confirmed by their dark current curves as shown in **Figure 2-7**. In OSCs, dark current (also referred to as leakage current) typically arises from charges generated through trap states, which are often associated with structural imperfections or the inherently disordered nature of the photoactive materials.[97, 98] As shown in **Figure 2-7a**, devices based on **P2** and **P3**

doi:10.6342/NTU202502276

exhibited noticeably lower leakage currents compared to the **P1**-based device, indicating the beneficial effect of incorporating SiO–C8 side chains in reducing unwanted current leakage. On the other hand, the leakage currents observed for the fluorinated **P4–P6** devices were all within the same order of magnitude ($\sim 10^{-5}$ A), suggesting that backbone fluorination mitigates the variation in leakage current caused by side-chain differences.

The charge transport properties of the devices were further analyzed using the space-charge-limited current (SCLC) method. A detailed description of the measurement procedure can be found in the Experimental Section, and the corresponding J–V characteristics are presented in **Figures 2-9** and **2-10**. The extracted hole and electron mobilities (μ_h/μ_e) for the **P1–P6** devices were determined to be $1.04 \times 10^{-5}/1.40 \times 10^{-6}$, $2.38 \times 10^{-4}/1.42 \times 10^{-4}$, $1.40 \times 10^{-3}/9.22 \times 10^{-5}$, $9.94 \times 10^{-6}/4.23 \times 10^{-6}$, $1.92 \times 10^{-4}/1.26 \times 10^{-4}$, and $2.02 \times 10^{-3}/8.41 \times 10^{-5}$ $\mathrm{cm^2 \cdot V^{-1} \cdot s^{-1}}$, respectively. These correspond to μ_h/μ_e ratios of 7.43, 1.68, 15.18, 2.35, 1.52, and 24.02, as summarized in **Figure 2-8** and **Table 2-3**. A consistent increase in hole mobility (μ_h) from **P1** to **P3** aligns well with the corresponding rise in J_{sc} values. A similar trend is evident among the fluorinated polymers (**P4–P6**).

Notably, the **P2** and **P5** devices exhibited more balanced charge transport (μ_h/μ_e ratios closer to 1), which is known to suppress bimolecular recombination and thus contributes to their higher *FF*. These observations are in agreement with the earlier J_{sc}–light intensity dependence analysis shown in **Figures 2-6c** and **2-6d**.

2.3.4 Morphology Characterization

These findings suggest that incorporating asymmetric side chains along with backbone fluorination can help establish a more favorable BHJ morphology, thereby enhancing overall device performance. To further investigate how side-chain configuration and backbone fluorination affect crystallinity and molecular organization, we examined the surface morphology of **P1–P6:ITIC-4F** blend films using tapping-mode atomic force microscopy (AFM). **Figure 2-11** shows the AFM height images, while the corresponding phase images are presented in **Figure 2-12**. The root-mean-square (RMS) roughness values measured for the blend films of **P1** to **P6** were 1.50, 3.05, 1.72, 3.44, 3.74, and 3.03 nm, respectively. Among these, the **P1**-based film exhibited the smoothest surface, likely due to its more amorphous nature (**Figure 2-12a**). However, this extensive intermixing and lack of phase separation appear to hinder exciton dissociation and charge transport, which correlates with its lowest J_{sc} value.[63, 99] Interestingly, the **P2** and **P5** blend films—both featuring asymmetric side chains—displayed higher surface roughness compared to their symmetric counterparts, suggesting improved crystallinity. Likewise, the fluorinated blend films (**P4–P6**) exhibited greater RMS values than their non-fluorinated analogs (**P1–P3**), indicating that backbone fluorination enhances polymer crystallinity. It is worth noting that, compared to the **P1** blend, the **P4**-based film exhibited a more fibrous surface morphology, further demonstrating the role of fluorination in promoting better molecular ordering and polymer's crystallinity.

To gain deeper insight into the above observations, grazing incidence wide-angle X-ray scattering (GIWAXS) measurements were conducted on the films. The resulting two-dimensional (2D) GIWAXS patterns are displayed in **Figures 2-13a**, **2-13b**, and **2-14**, with their corresponding one-dimensional (1D) line-cut profiles presented in

doi:10.6342/NTU202502276

Figures 2-13c and **2-13d**. Due to the inherent flexibility of the DT side chains, the **P1** blend film exhibited no distinct peaks in the 1D line-cut profile, indicating a largely amorphous morphology. Amorphous domains are generally associated with poorer charge transport properties when compared to crystalline regions, which aligns with the charge mobility trends observed in the earlier SCLC measurements. As a result, the **P1**-based device demonstrated the lowest overall performance. In contrast, the blend films of **P2** through **P5** showed pronounced lamellar (100) stacking peaks in both the in-plane (IP) and out-of-plane (OOP) directions, suggesting enhanced molecular order. Particularly, the **P4** and **P5** films displayed an additional (200) lamellar peak in the OOP direction, which can be attributed to the high backbone coplanarity of the PII2TF structure. This highlights the effect of backbone fluorination in promoting crystallinity, as clearly seen in the **P4** blend film when compared to the more disordered **P1** film. The rigid conformation of the PII2TF backbone helps reduce torsional strain from the DT side chains, thereby enabling more efficient molecular packing and improved device performance. Furthermore, both **P2** and **P5** blend films exhibited a distinct π–π stacking peak (010) in the OOP direction, indicative of a dominant face-on orientation. This ordered packing is attributed to the effective interchain interactions facilitated by the asymmetric side chains. These findings underscore the critical role of asymmetric side-chain design in promoting favorable molecular organization within the active layer.

The key crystallographic parameters—such as peak position, d-spacing, and crystal coherence length (CCL)—along both the out-of-plane (OOP) and in-plane (IP) directions are summarized in **Table 2-4** and **Table 2-5**, respectively. The CCL values were calculated based on the Scherrer equation: CCL = $2\pi/\Delta q$, where Δq represents the full width at half maximum (FWHM) of the corresponding diffraction peak.[100] As shown in **Figures 2-15a** and **2-15b**, the observed increases in d-spacing along both

doi:10.6342/NTU202502276

OOP and IP directions are closely linked to the presence of bulky SiO–C8 side chains and the use of the fluorinated PII2TF backbone. Due to the volumetric bulk of the SiO–C8 chains, a progressive increase in (100) d-spacing was observed from the **P2** to **P3** blend films in both orientations. A similar trend is evident among the fluorinated counterparts. Meanwhile, the fluorinated blend films **P4–P6** exhibited significantly larger (100) d-spacing values in both the out-of-plane (OOP) and in-plane (IP) directions compared to their non-fluorinated counterparts, **P1–P3**. This observation is primarily attributed to the greater backbone rigidity of PII2TF in contrast to PII2T. The structural rigidity of PII2TF is further evidenced by the increased (010) d-spacing in the OOP direction for the **P5** blend film, relative to the non-fluorinated **P2** film (**Figure 2-15c**). Notably, **P2** and **P5**—both incorporating asymmetric SiO–C8/DT side chains—exhibited the largest crystal coherence lengths (CCL) in both OOP and IP directions among all samples (**Figures 2-15a** and **2-15b**). Their larger crystalline domains are also corroborated by the higher RMS roughness values observed in AFM measurements (**Figure 2-11**). This suggests that the asymmetric side chains promote efficient interchain packing, which in the case of **P2**, also compensates for torsional distortion typically seen in the PII2T backbone. As a result, the molecular planarity and crystallinity are significantly enhanced. Furthermore, the asymmetric side chains present in **P2** and **P5** contribute to a molecular dipole moment, which strengthens intermolecular forces and facilitates the formation of well-interconnected donor–acceptor (D/A) networks within the active layer.[85] These structural advantages improve D/A interfacial contact, enhancing exciton dissociation and suppressing charge recombination. Collectively, these factors account for the high fill factor values exceeding 57% observed in both **P2-** and **P5-**based devices.

doi:10.6342/NTU202502276

2.4 Conclusion

In conclusion, this study investigates the influence of synergistic structural modifications—specifically, asymmetric side chains and backbone fluorination—on the performance of polymer donors in photovoltaic applications. Six IID-based polymers were examined, each exhibiting subtle differences in side-chain architecture and backbone fluorination. Our findings indicate that both the degree of backbone fluorination and the proportion of siloxane-terminated side chains significantly affect the optoelectronic characteristics. Fluorination of the polymer backbone results in **P4–P6** having deeper HOMO/LUMO energy levels and red-shifted absorption spectra compared to their non-fluorinated counterparts (**P1–P3**). Moreover, an increase in the content of SiO–C8 side chains leads to a gradual elevation of the HOMO/LUMO energy levels across the polymer series. Notably, **P2** and **P5**—those incorporating asymmetric side chains—achieve the highest PCE values within their respective families, PII2T and PII2TF. Devices based on the fluorinated polymers **P4–P6** consistently outperform those utilizing non-fluorinated **P1–P3**. Interestingly, backbone fluorination also mitigates performance disparities among polymers with different side-chain configurations. Morphological studies reveal that geometric mismatch in the side chains enhances interchain packing efficiency, contributing to improved crystallinity and dominant face-on orientation, which collectively facilitate exciton separation and charge transport. Additionally, the presence of noncovalent F···S interactions on the thiophene units—induced by backbone fluorination—stiffens the PII2TF polymer backbone, promoting better crystallinity and molecular organization. These interactions also bolster intermolecular cohesion, offsetting torsional strain introduced by the side chains. As a result of enhanced backbone planarity, the impact of side-chain variation on device performance is substantially diminished. Overall, our results suggest that the combined

doi:10.6342/NTU202502276

effect of backbone fluorination and asymmetric side chains presents a promising strategy to fine-tune energy levels, molecular arrangement, and photovoltaic efficiency in conjugated polymer donors. While the PCEs achieved in this work remain modest, further enhancement may be possible through the copolymerization of IID units with more advanced conjugated moieties and the adoption of high-performance acceptors.

doi:10.6342/NTU202502276

Figures

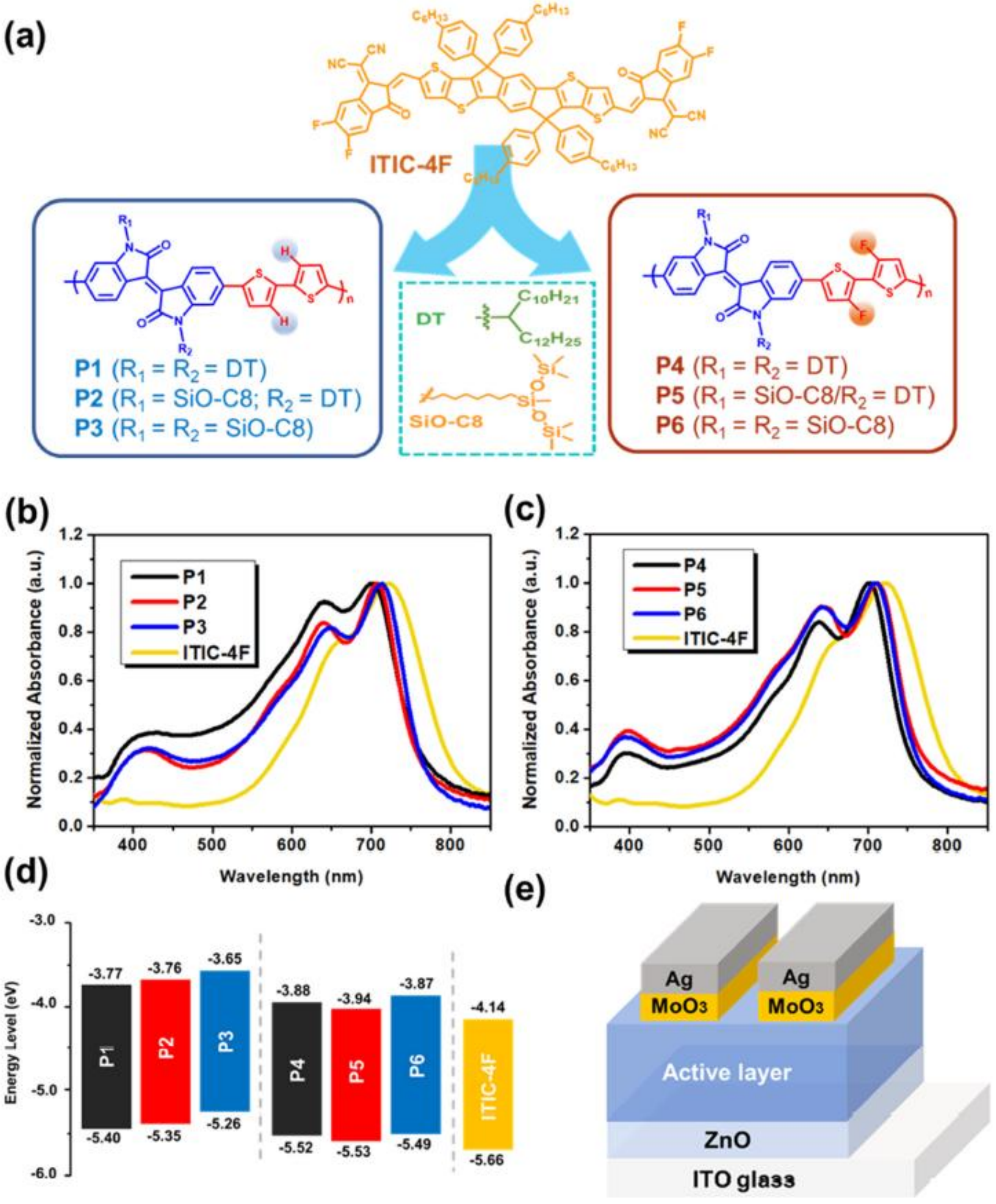

Figure 2-1 (a) The studied six IID-based polymer donors, **P1–P6**, and NFA, **ITIC-4F** and (b,c) their normalized UV–vis absorption spectra. (d) The energy-level diagram of the studied compounds. (e) Schematic illustration of device architecture.

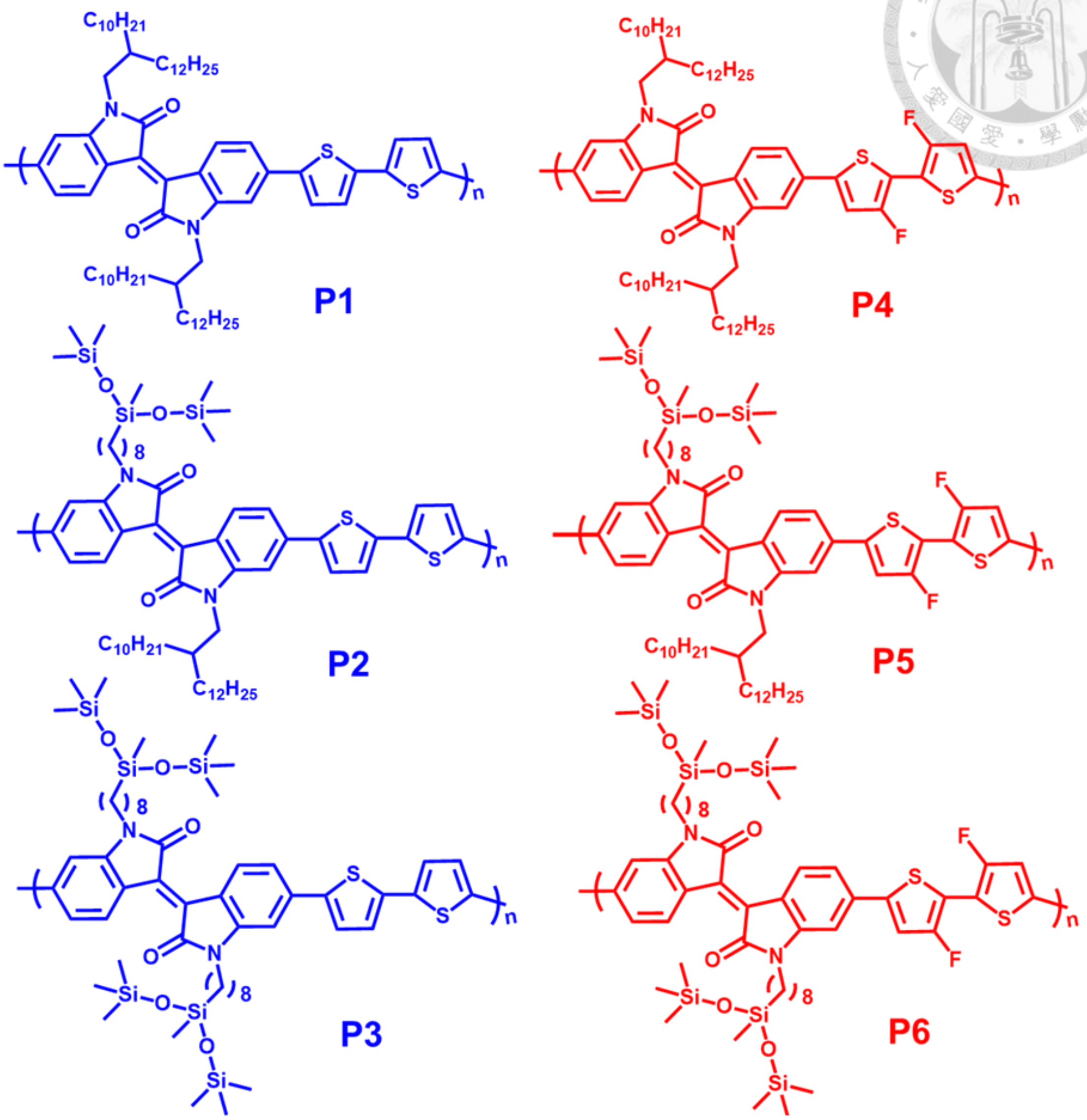

Figure 2-2 Chemical structures of **P1-P6**.

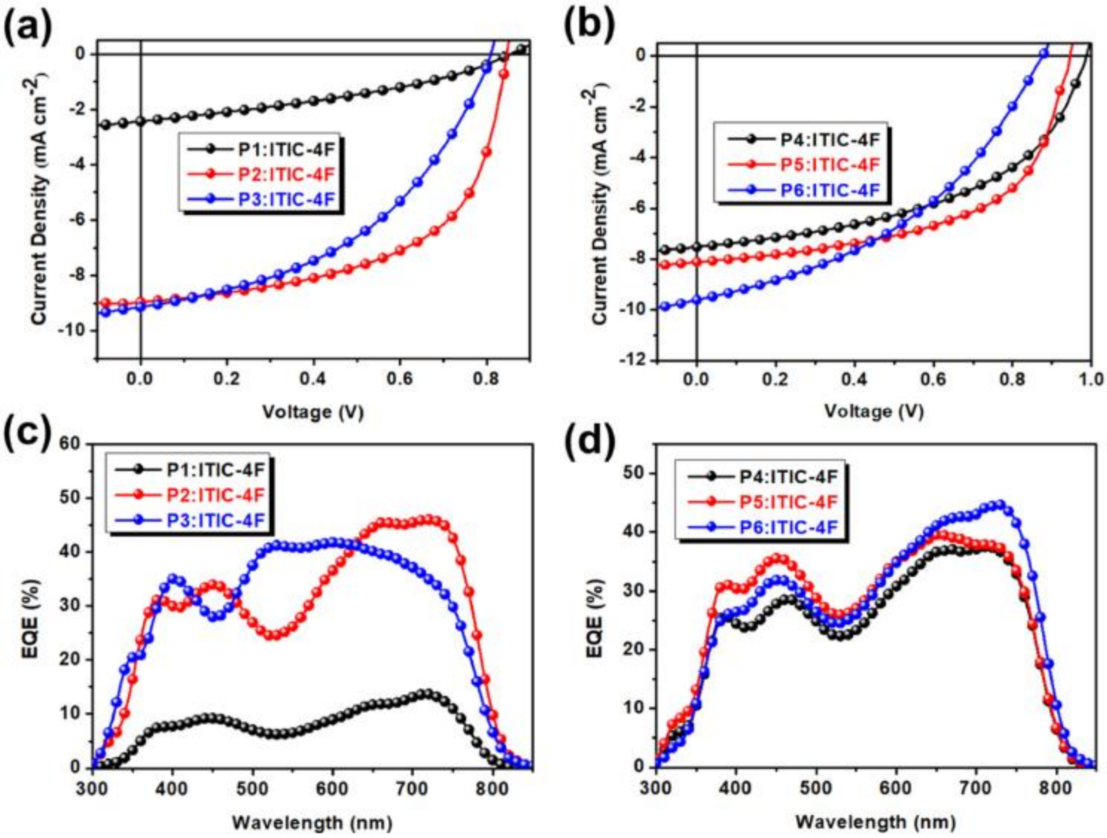

Figure 2-3 (a, b) *J*-*V* and (c, d) EQE curves of the fabricated binary PSCs using (a, c) **P1–P3** and (b, d) **P4–P6** as the polymer donors.

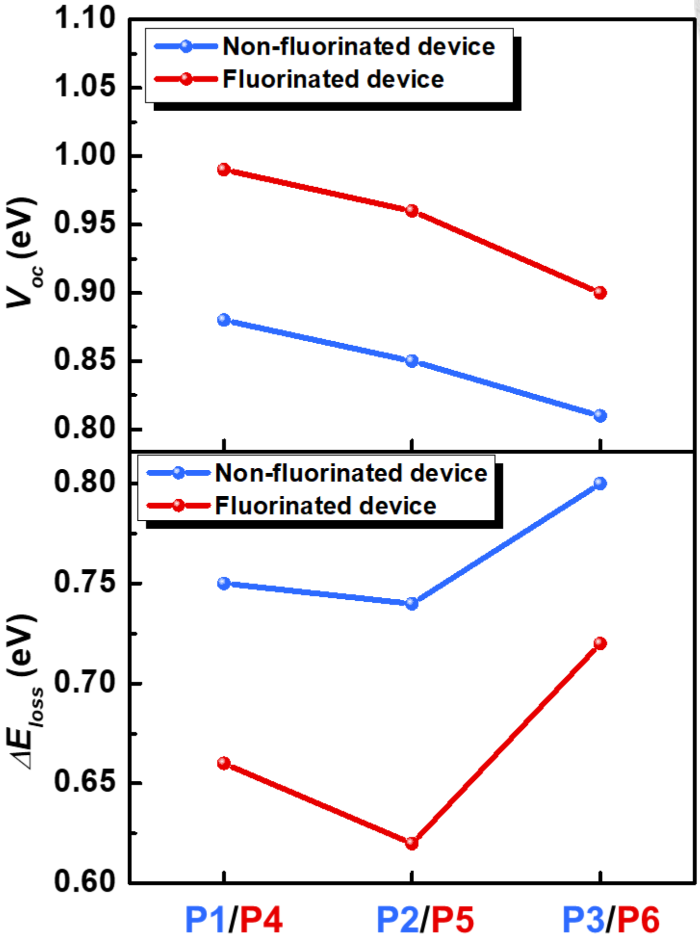

Figure 2-4 V_{oc} and potential loss comparison of the non-fluorinated **P1-P3** devices and the fluorinated **P4-P6** devices.

doi:10.6342/NTU202502276

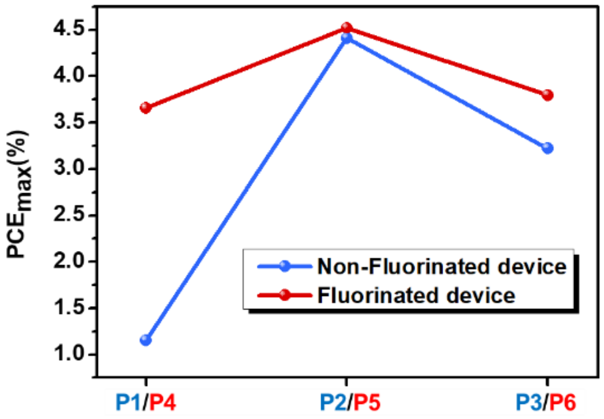

Figure 2-5 PCE comparison of the non-fluorinated **P1-P3** devices and the fluorinated **P4-P6** devices.

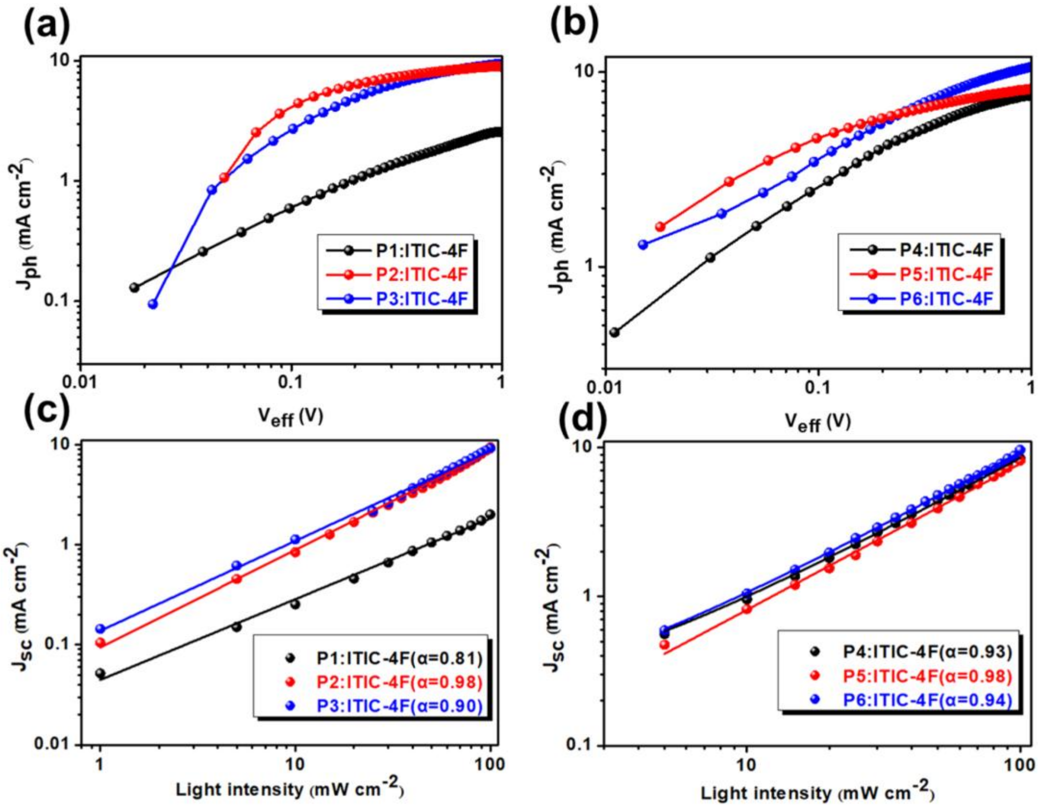

Figure 2-6 (a, b) J_{ph}-V_{eff} characteristics and (c, d) J_{sc}-light intensity fitting lines for (a, c) **P1-P3** and (b, d) **P4-P6** devices.

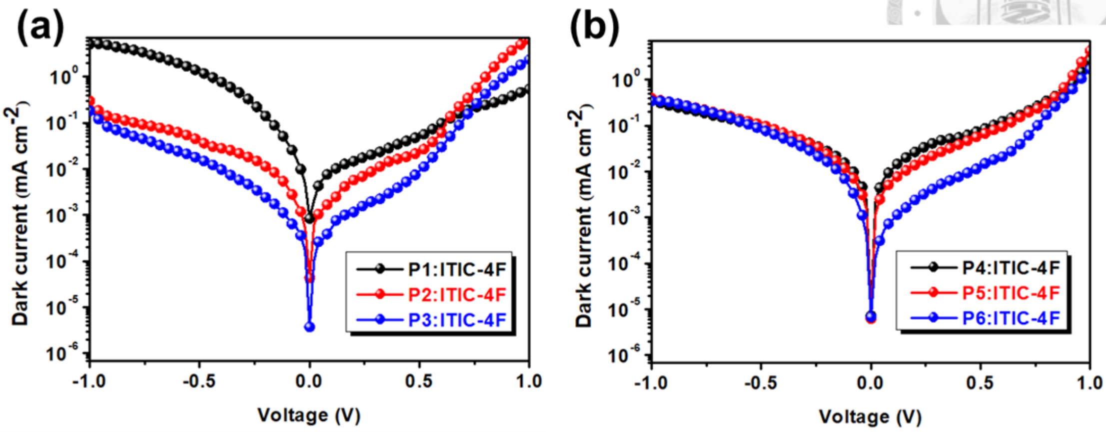

Figure 2-7 The dark currents for (a) **P1-P3** and (b) **P4-P6** devices.

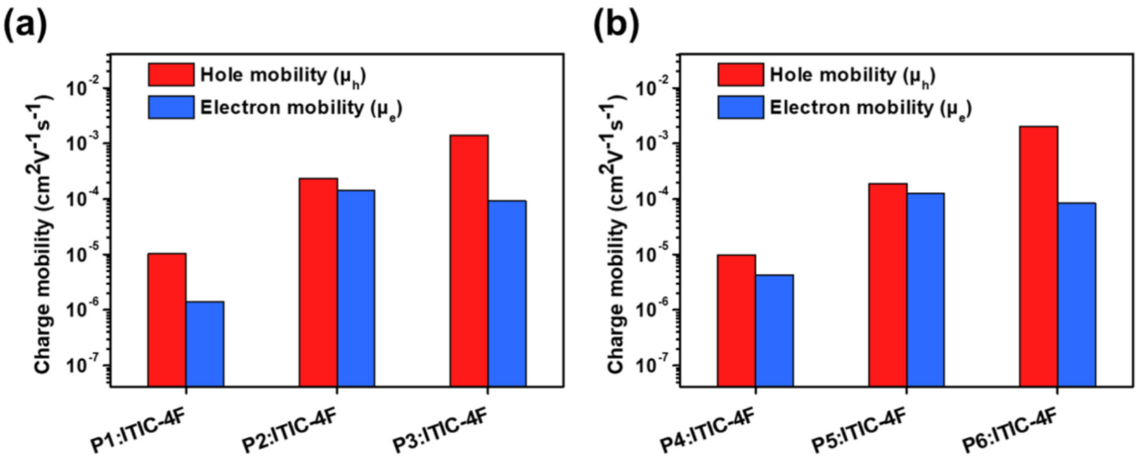

Figure 2-8 Diagrams of hole/electron mobility for (a) **P1–P3** devices and (b) **P4–P6** devices.

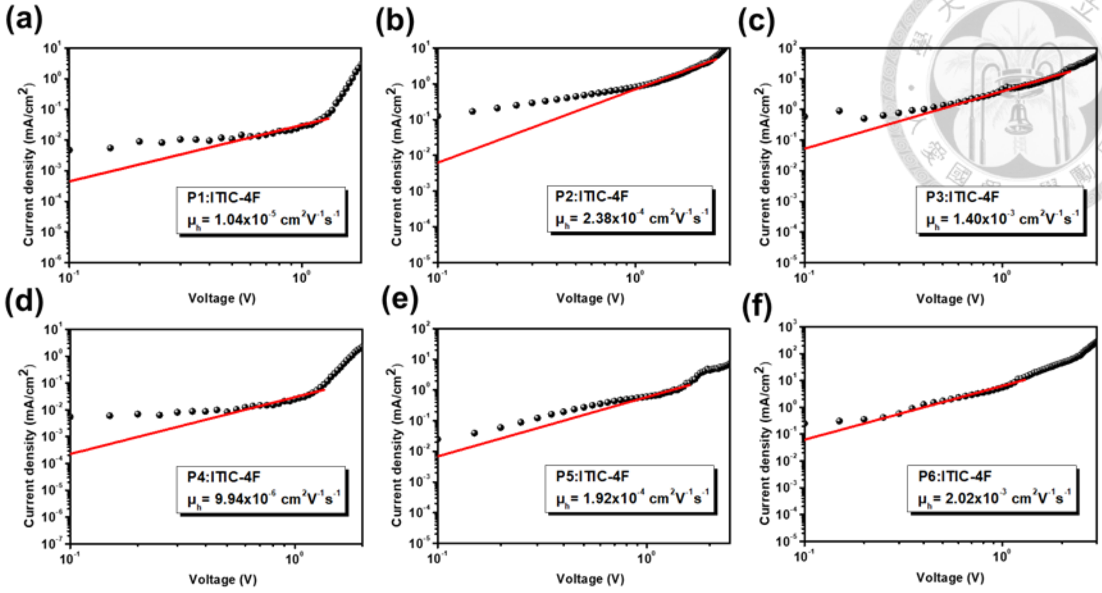

Figure 2-9 *J*-*V* curves with fitting lines (log*J* versus 2log*V*) for the hole-only devices for estimation of hole mobilities using an SCLC model.

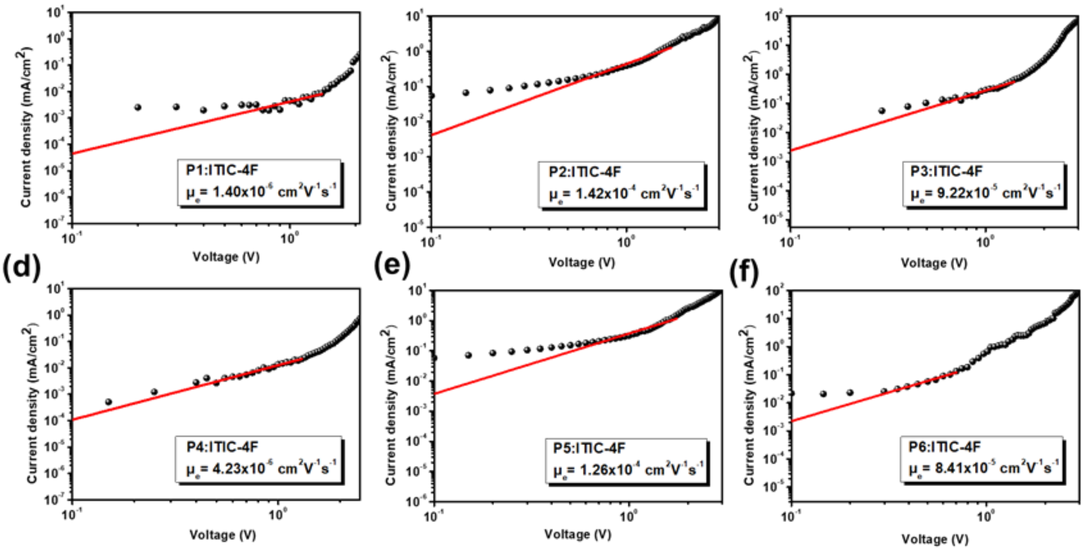

Figure 2-10 *J*-*V* curves with fitting lines (log*J* versus 2log*V*) for the electron-only devices for estimation of electron mobilities using an SCLC model.

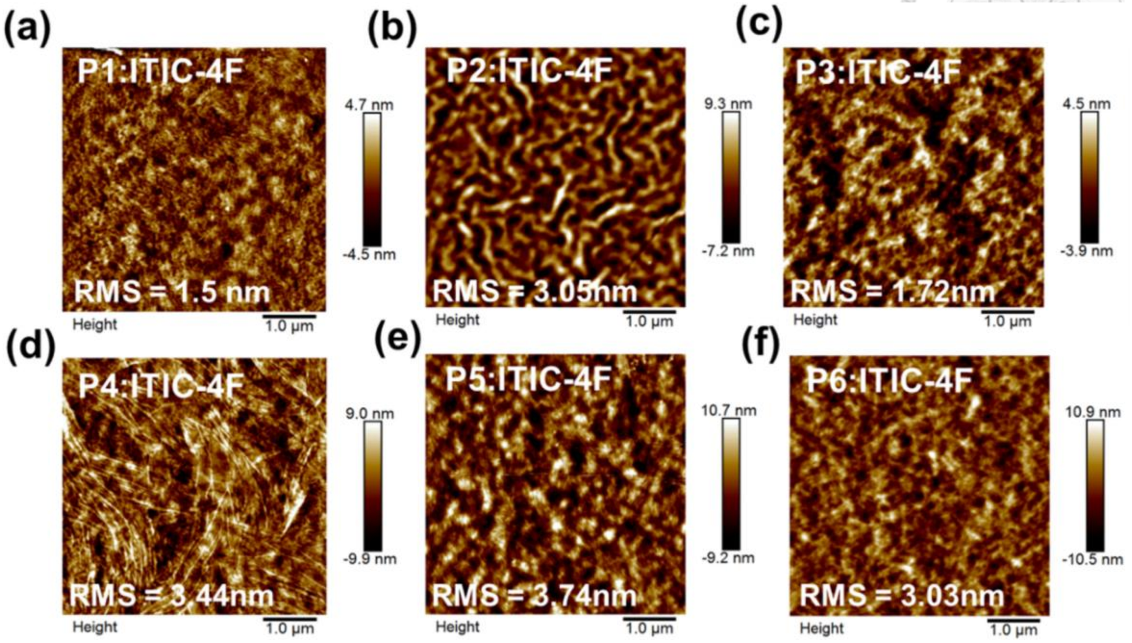

Figure 2-11 AFM height images for studied blend films based on P1–P6 as indicated.

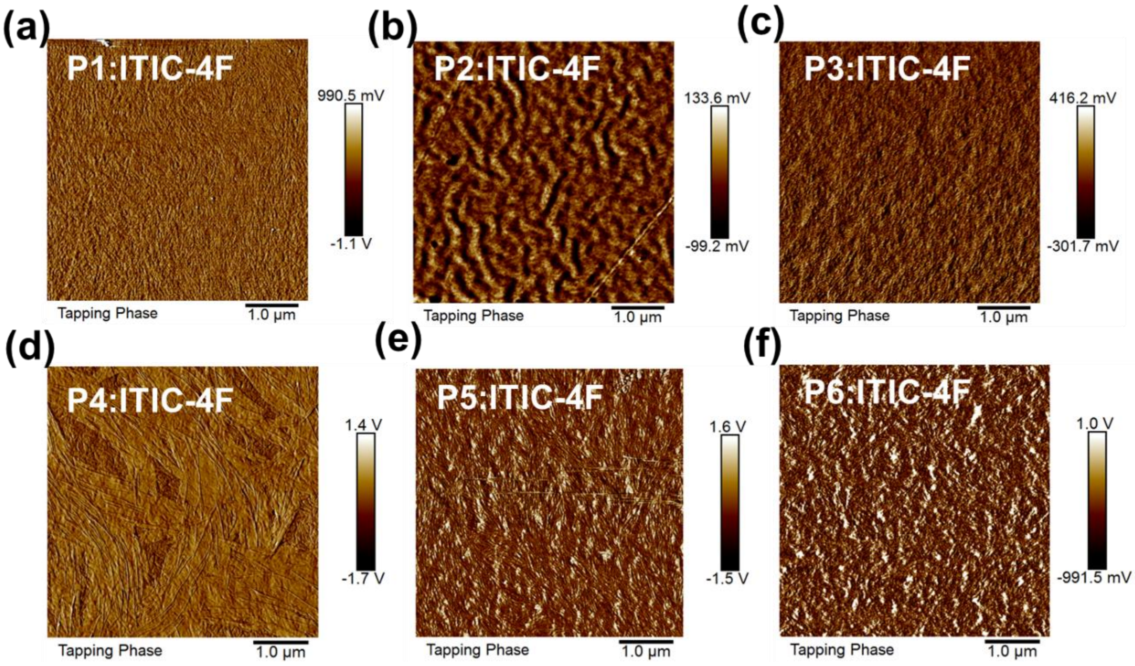

Figure 2-12 AFM phase images for studied blend films based on **P1-P6** as indicated.

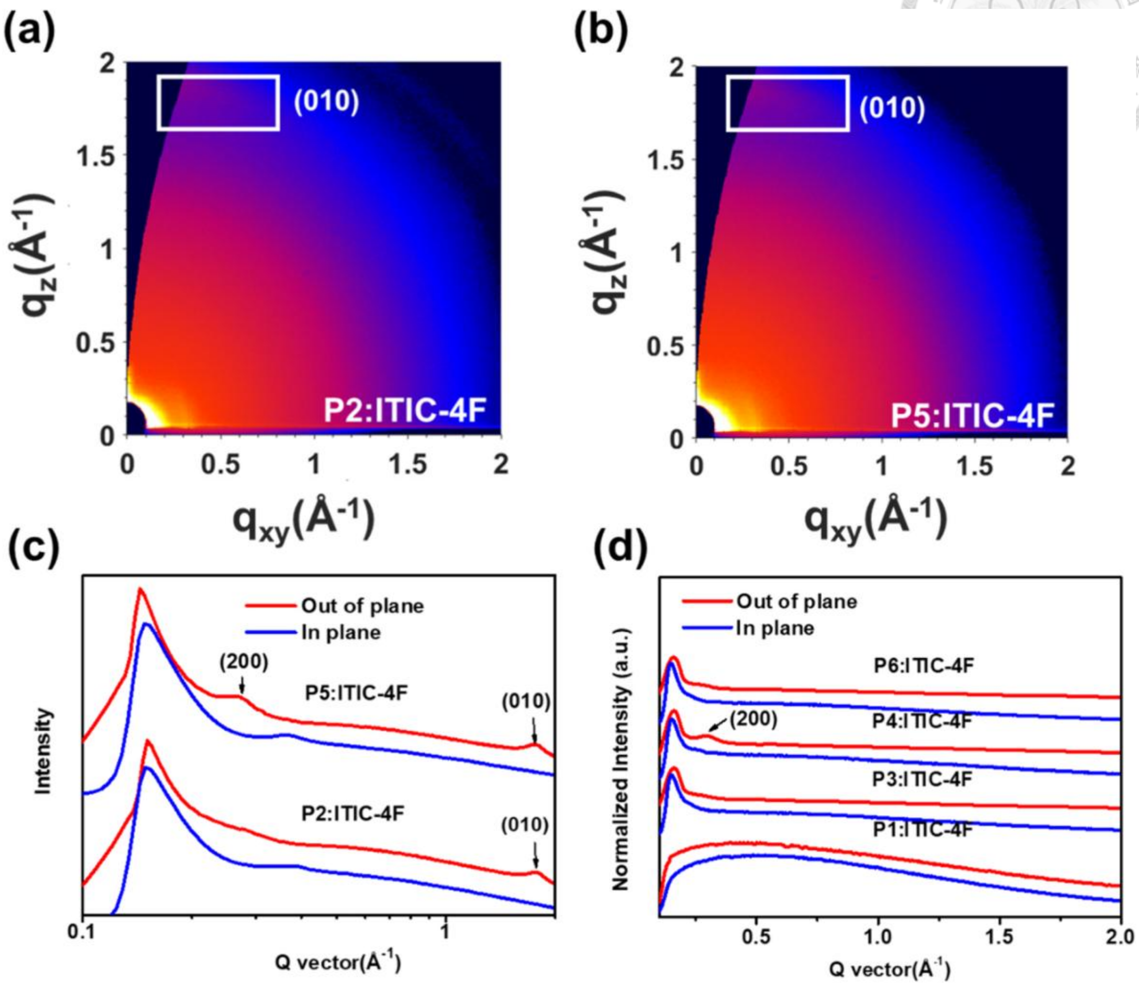

Figure 2-13 (a, b) 2D GIWAXS patterns for studied blend films based on **P2** and **P5** as indicated. Out-of-plane (red line) and in-plane (blue line) line-cuts of the 2D-GIWAXS results for the studied blend films based on (c) **P2** and **P5** with asymmetric side chains and (d) **P1, P3, P4** and **P6** with symmetric side chains.

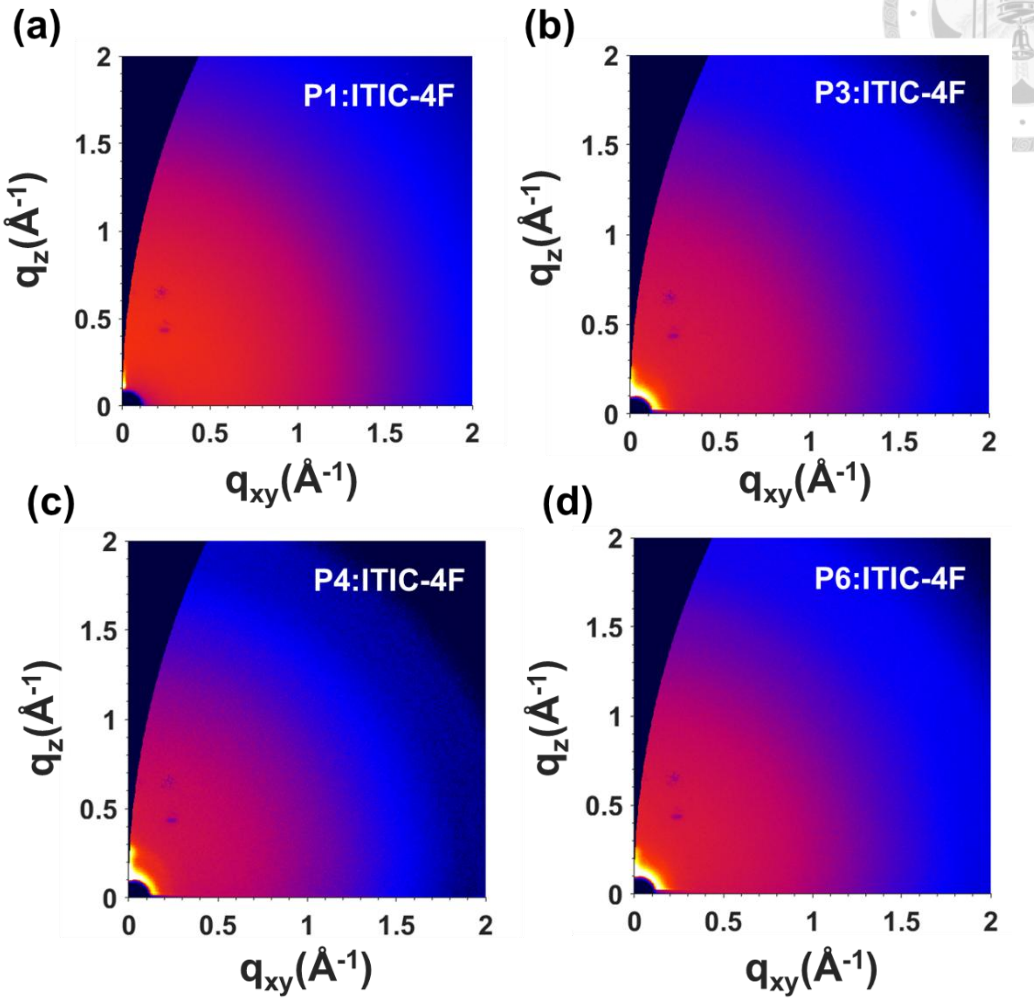

Figure 2-14 2D GIWAXS patterns for studied blend films based on **P1**, **P3**, **P4** and **P6** as indicated.

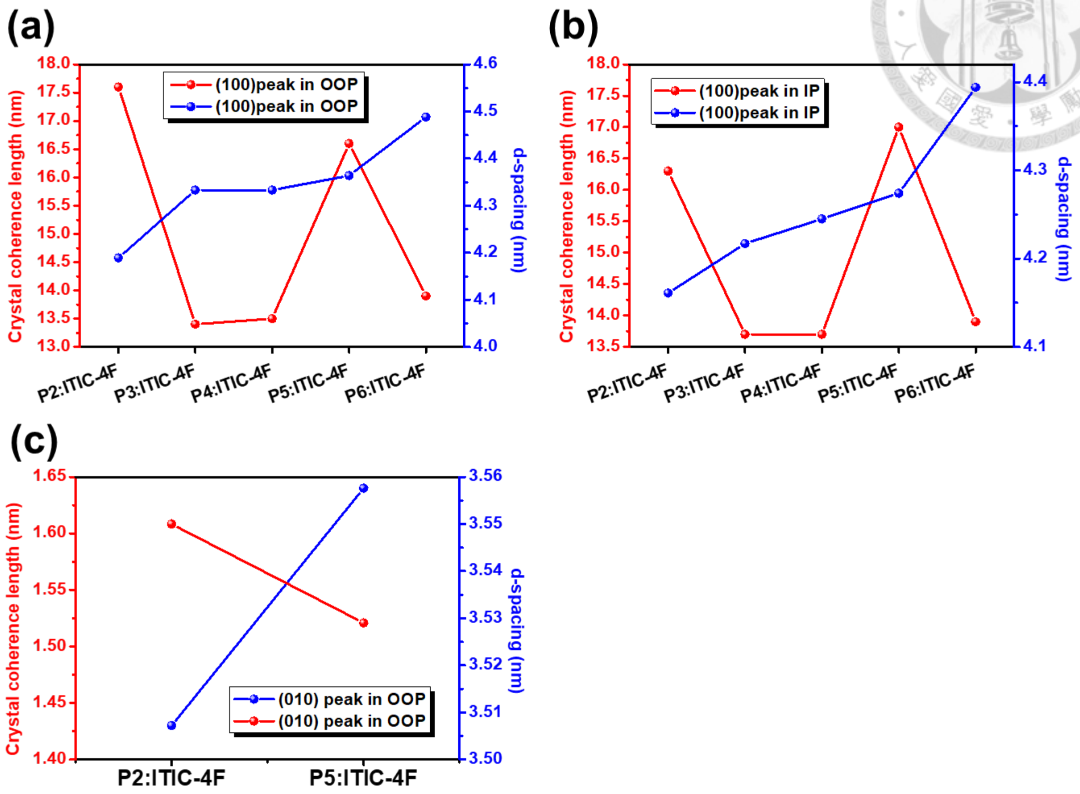

Figure 2-15 CCL (red symbol) and *d*-spacing (blue symbol) for the blend films based on **P2-P6** in (a) the out-of-plane (OOP) and (b) the in-plane (IP) directions. (c) CCL (red symbol) and *d*-spacing (blue symbol) of the (010) peak for the blend films based on **P2** and **P5** in the OOP direction.

Tables

Table 2-1 Physical, optical, and electrochemical properties of **P1-P6.**

	M_n (kDa)[a]	**M_w (kDa)[a]**	**PDI[a]**	**λ_{max} (nm)[b]**	**E_g (eV)[c]**	**HOMO (eV)[d]**	**LUMO (eV)[e]**
P1	200	260	1.30	700	1.63	-5.40	-3.77
P2	168	398	2.34	706	1.59	-5.35	-3.76
P3	197	251	1.27	714	1.61	-5.26	-3.65
P4	143	214	1.50	703	1.65	-5.52	-3.88
P5	146	444	3.27	711	1.58	-5.53	-3.94
P6	182	252	1.38	716	1.62	-5.49	-3.87

[a] M_n, M_w, and *PDI* were measured by GPC eluted by THF. [b] Thin-film UV−vis absorption maxima. [c] Optical E_g derived from the absorption onset of polymer films. [d] CV determined using Fc/Fc+ as an internal potential reference. [e] Caculated by LUMO = HOMO + E_g.

Table 2-2 Photovoltaic performance for the fabricated binary PSCs based on **P1–P6**.

With ITIC-4F	V_{oc} (V)	J_{sc} (mA cm^{-2})	*FF* (%)	PCE$_{max}$ (PCE$_{avg}$)^{a} (%)
P1	0.880 (0.850±0.03)	3.046 (2.975±0.071)	43.103 (41.508±1.595)	1.156 (1.050±0.106)
P2	0.847 (0.837±0.01)	9.119 (8.967±0.152)	57.391 (54.914±2.477)	4.412 (4.244±0.168)
P3	0.810 (0.769±0.041)	9.142 (9.067±0.08)	42.903 (37.230±5.70)	3.224 (2.911±0.313)
P4	0.987 (0.966±0.021)	7.525 (7.431±0.094)	49.234 (46.663±2.571)	3.657 (3.349±0.308)
P5	0.963 (0.952±0.011)	8.179 (7.79±0.389)	57.107 (55.074±2.033)	4.524 (4.216±0.308)
P6	0.896 (0.892±0.001)	9.878 (9.207±0.671)	41.533 (40.729±0.804)	3.798 (3.590±0.208)

[a] The average PCE shown in the parentheses are calculated based on 10 devices.

Table 2-3 Charge transport properties of **P1–P6** blend films.

Active layer	Hole mobility μ_h (cm^{2}V^{-1}s^{-1})	Electron mobility μ_e (cm^{2}V^{-1}s^{-1})	μ_h/μ_e
P1:ITIC-4F	1.04×10^{-5}	1.40×10^{-6}	7.43
P2:ITIC-4F	2.38×10^{-4}	1.42×10^{-4}	1.68
P3:ITIC-4F	1.40×10^{-3}	9.22×10^{-5}	15.18
P4:ITIC-4F	9.94×10^{-6}	4.23×10^{-6}	2.35
P5:ITIC-4F	1.92×10^{-4}	1.26×10^{-4}	1.52
P6:ITIC-4F	2.02×10^{-3}	8.41×10^{-5}	24.02

Table 2-4 Detailed GIWAXS (100) and (010) peak information in the OOP of the blend films based on **P1-P6**.

	Peak location (100) (Å^{-1})	***d*-spacing (100) (Å)**	**FWHW (100) (Å)**	**C.C.L (100) (nm)**	**Peak location (010) (Å^{-1})**	***d*-spacing (010) (Å)**	**FWHW (010) (Å)**	**C.C.L (010) (nm)**
P1:ITIC-4F	-	-	-	-	-	-	-	-
P2:ITIC-4F	0.150	41.89	0.03567	17.6	0.177	35.50	0.4389	1.43
P3:ITIC-4F	0.145	43.33	0.04701	13.4	-	-	-	-
P4:ITIC-4F	0.145	43.33	0.04666	13.5	-	-	-	-
P5:ITIC-4F	0.144	43.63	0.0377	16.6	0.178	35.29	0.38366	1.64
P6:ITIC-4F	0.140	44.88	0.04506	13.9	-	-	-	-

Table 2-5 Detailed GIWAXS (100) peak information in the IP of the blend films based on **P1-P6**.

Active layer	**Peak location (100) (Å^{-1})**	***d*-spacing (100) (Å)**	**FWHW (100) (Å)**	**C.C.L (100) (nm)**
P1:ITIC-4F	-	-	-	-
P2:ITIC-4F	0.151	41.61	0.03862	16.3
P3:ITIC-4F	0.149	42.17	0.04592	13.7
P4:ITIC-4F	0.148	42.45	0.04574	13.7
P5:ITIC-4F	0.147	42.74	0.03695	17.0
P6:ITIC-4F	0.143	43.94	0.04531	13.9

CHAPTER 3

Morphology-Controlled All-Polymer Solar Cells Enabled by Mixed Green Solvent Strategy

3.1 Introduction

All-polymer solar cells (All-PSCs), which utilize conjugated polymers as both the electron donor and acceptor materials, have gained increasing attention as a promising generation of photovoltaic technologies.[101–103] Compared to polymer:small molecule systems, All-PSCs exhibit several key benefits such as superior mechanical flexibility, improved thermal stability, and ease of solution processing.[104–107] These characteristics make them particularly suitable for flexible and wearable electronic devices. The adoption of polymeric acceptors also enhances morphological compatibility and allows for more tunable energy levels, both of which are critical for long-term operational stability.[108–110] Over the past decade, the power conversion efficiency (PCE) of All-PSCs has seen substantial growth, now exceeding 17%.[111, 112] This progress has brought them closer to competing with traditional polymer:non-fullerene small molecule solar cells.[113] Nonetheless, consistently achieving high efficiencies remains a significant hurdle, primarily due to the difficulty in regulating phase separation between two polymeric components. This often results in unfavorable film morphology and hindered charge transport.[114, 115] It is now well recognized that precise control over morphology—specifically in terms of domain size

doi:10.6342/NTU202502276

and donor–acceptor (D/A) interface distribution—is crucial for reducing recombination losses and enhancing exciton dissociation and charge transport. To address these challenges, researchers have employed various strategies, including rational molecular design, thermal annealing, blade coating, and post-deposition treatments.[116, 117] Among these, processing solution engineering—particularly through the use of solvent and solid additives—has emerged as a highly effective and scalable technique.[118, 119] High-boiling-point solvent additives like 1,8-diiodooctane (DIO), chloronaphthalene (CN), and diphenyl ether (DPE) are commonly used to tailor molecular crystallinity and optimize phase separation.[120, 121] However, residual traces of these additives can persist in the film after processing, potentially causing long-term morphological instability and reduced device reliability.[122, 123] In contrast, solid additives such as dithieno[3,2-b:2′,3′-d]thiophene (DTT) and diiodobenzene (DIB) have emerged as attractive alternatives due to their clean evaporation during post-annealing and their ability to transiently influence polymer packing through non-covalent interactions.[124, 125] These solid additives have demonstrated improvements in both film uniformity and device performance, including enhanced photostability.[126] Beyond additive selection, the solvent system itself plays a critical role in dictating the final morphology of the active layer.[127, 128] While chloroform (CF) remains a widely used solvent due to its excellent solubility and rapid evaporation characteristics, it poses environmental and health hazards and is often insufficient on its own to produce optimal morphologies.[129] To address these limitations, we propose a green co-solvent strategy. In this approach, small amounts of environmentally friendly, high-boiling-point solvents—such as tetrahydrofuran (THF), 2-methyltetrahydrofuran (2-MeTHF), and 3-methyltetrahydrofuran (3-MeTHF)—are blended with CF to fine-tune the film formation dynamics and improve morphology control.

doi:10.6342/NTU202502276

In this work, we systematically explored how mixed solvent systems in combination with the solid additive DTT influence film morphology, molecular arrangement, energetic disorder, and overall device performance in all-PSCs. Compared to devices processed using chloroform alone, those fabricated with co-solvent mixtures exhibited tighter lamellar packing, smaller domain sizes, reduced trap densities, and more balanced charge carrier transport. Notably, devices using CF+THF and CF+2-MeTHF as solvent systems achieved power conversion efficiencies exceeding 17%, outperforming those based on CF-only and CF+3-MeTHF formulations.

Furthermore, the use of green co-solvent blends enhanced several critical optoelectronic properties, including improved exciton dissociation (as indicated by P_d/P_c ratios), extended carrier lifetimes (from TPV measurements), reduced recombination losses (from TRPL analysis), and elevated built-in voltages (V_{bi}). These improvements collectively contribute to superior photovoltaic performance. Beyond performance enhancement, this approach introduces a more sustainable and environmentally conscious processing method for All-PSC fabrication. By incorporating eco-friendly solvents and cleanly evaporating solid additives, our strategy offers a practical pathway for morphology control that supports both high efficiency and long-term scalability—marking a promising direction for future green manufacturing of polymer solar cells.

doi:10.6342/NTU202502276

3.2 Experimental Section

3.2.1 Materials

The polymer donor PM6 and the polymer acceptor PY-IT were purchased from Solarmer Materials. Chloroform (CF), Tetrahydrofuran (THF) and 2-methyltetrahydrofuran (2-MeTHF) were purchased from Sigma-Aldrich. 3-methyltetrahydrofuran (3-MeTHF) and dithieno[3,2-b:2′,3′-d]thiophene (DTT) were purchased from TCI Chemicals.

3.2.2 Device Fabrication and General Characterizations

In this study, inverted solar cell devices with a structure of ITO/ZnO/active layer/MoO_3/Ag were fabricated. The ITO-coated glass substrates underwent sequential ultrasonication in diluted detergent, deionized water, acetone, and isopropanol, each for 10 minutes. After cleaning, the substrates were oven-dried and subjected to plasma treatment for 10 minutes prior to ZnO deposition. The ZnO layer was prepared via a sol-gel approach by dissolving 100 mg of zinc acetate dihydrate in 2 mL of 2-methoxyethanol, followed by the addition of 56 μL of ethanolamine. The resulting precursor solution was spin-coated onto the ITO substrates at 4000 rpm for 30 seconds. This was followed by a two-step annealing process: first at 50 °C for 5 minutes in a nitrogen-filled glove box, and then at 180 °C for 15 minutes in ambient air. For the active layer, a binary blend of PM6 and PY-IT (donor:acceptor ratio of 1.2:1, total concentration of 15 mg/mL) was dissolved in chloroform mixed with a green solvent system consisting of THF/2-MeTHF/3-MeTHF, and included 100 wt% dithieno[3,2-b:2′,3′-d]thiophene (DTT) as a volatile solid additive. The binary solution was stirred vigorously at 50 °C for 2.5 hours inside a nitrogen-filled glove box. The solvent ratio of chloroform to green solvent was adjusted to 98:2 (v/v). For ternary devices, a pre-dissolved Y6 or D18 solution—prepared by dissolving the material in the same chloroform–green solvent mixture containing DTT overnight—was added to the binary blend and stirred at 50 °C for an additional 2.5 hours in the glove box. The resulting active layer solutions were deposited onto the ZnO-coated substrates by spin-coating at 3000 rpm for 40 seconds, followed by thermal annealing at 90 °C for 5 minutes. Finally, 8 nm of MoO_3 and 100 nm of Ag were thermally evaporated under high vacuum conditions ($\sim 10^{-6}$ Torr) to complete the device structure. The active area of each device was defined as 5.625 mm^2.

The current–voltage (J–V) characteristics of the fabricated solar cells were recorded using a computer-controlled Keithley 2400 source-measurement unit (SMU) under simulated AM 1.5G illumination at 100 mW cm^{-2}. Illumination was provided by an SS-F5-3A solar simulator (Enlitech Co., Ltd., Taiwan), and the intensity was calibrated using a silicon photodiode equipped with a KG-5 filter. External quantum efficiency (EQE) spectra were measured using monochromatic light generated by a xenon lamp during illumination, with the QE-R system from Enlitech Co., Ltd. Calibration of the spectral light intensity—from 300 to 1000 nm—was performed using a standard monocrystalline silicon reference cell. Surface morphology was examined using atomic force microscopy (AFM) in tapping mode, employing a MultiMode system equipped with a Nanoscope 3D controller (Digital Instruments) at ambient temperature. UV–visible absorption spectra were collected using a Hitachi U-4100 spectrophotometer. To estimate the Urbach energy (E_U), FTPS-EQE measurements were conducted using the FTPS PECT-600 system (Enlitech Co., Ltd.). The relative dielectric constant and Mott–Schottky analysis for determining the built-in potential (V_{bi})

were carried out using the PIAOS system from FLUXiM. Charge carrier mobility (μ_{device}) was evaluated through photo-CELIV (charge extraction by linearly increasing voltage) measurements, also using the PIAOS system. For transient photocurrent (TPC) measurements, the devices were subjected to a 200 µs square LED light pulse under short-circuit conditions and without background illumination. The resulting current transients were captured by the PIAOS system. In transient photovoltage (TPV) analysis, a 405 nm laser diode was employed to maintain the devices under open-circuit (V_{oc}) conditions, and the voltage decay was similarly recorded using the PIAOS system (FLUXiM).

3.2.3 Space Charge Limited Current (SCLC) Measurement

The hole and electron mobilities of the bulk heterojunction (BHJ) films were evaluated using the space-charge-limited current (SCLC) technique. For this purpose, hole-only devices were constructed with the architecture: ITO glass/PEDOT:PSS/active layer/MoO_3/Ag, while electron-only devices employed the configuration: ITO glass/ZnO/active layer/TPBi/LiF/Ag. The SCLC measurement was carried out in dark conditions, and mobility was determined according to the modified Mott-Gurney equation:[130]

$$J=\frac{9}{8}\varepsilon_0\varepsilon_r\mu\frac{V^2}{L^3}$$

where J is current density, V is the voltage, μ is the mobility, L is the active layer thickness, ε_0 is the vacuum permittivity and ε_r is the relative dielectric constant.

The relative dielectric constant can be obtained through the following equation:[131]

$$\varepsilon_r = \frac{Cd}{\varepsilon_0 A}$$

where C is the measured capacitance, d is the thickness of active layer, ε_0 represents the vacuum permittivity and A is the active area.

3.2.4 GIWAXS and GISAXS Measurement

The grazing-incidence wide-angle X-ray scattering (GIWAXS) and small-angle X-ray scattering (GISAXS) data of the studied BHJ films were estimated from the BL23A and 13A1 beamline (TLS) at the National Synchrotron Radiation Research Center (NSRRC) in Taiwan. All studied BHJ films were spin-coated on the Si wafers (1.5×1.5 cm^2) by the same fabrication process as the active layer of solar cell devices. The samples were irradiated at fixed incident angles of 0.15^{o} and 0.12^{o} under monochromatic light beams (beamlines BL23A and 13A1) with wavelengths of 1.2398 and 1.0273, respectively.

3.2.5 TRPL measurement

Carrier lifetimes are fitted using a biexponential decay model, i.e., $I(t)=A_1\exp\left(-\frac{t}{\tau_1}\right)+A_2\exp\left(-\frac{t}{\tau_2}\right)$. Here, A_1 and A_2 denote the relative contributions of each decay component. The faster decay time constant, τ_1, is typically associated with trap-assisted nonradiative recombination occurring at the surface or grain boundaries (GBs), whereas the slower component, τ_2, corresponds to intrinsic radiative recombination processes within the bulk of the film.

3.3 Results and Discussion

3.3.1 Molecular characterization and optical properties

In this study, we introduce a co-solvent approach aimed at addressing both morphology optimization and environmental concerns in all-polymer solar cells (All-PSCs). This strategy involves the partial substitution of conventional but hazardous chloroform (CF) with environmentally friendlier solvents that possess higher boiling points. As illustrated schematically in **Figure 3-1a**, four solvent systems were formulated by blending CF with varying amounts of green solvents: tetrahydrofuran (THF), 2-methyltetrahydrofuran (2-MeTHF), and 3-methyltetrahydrofuran (3-MeTHF). For this investigation, we employed a high-performance donor–acceptor polymer pair—PM6 as the donor and PY-IT as the acceptor (**Figure 3-2**). This material combination is widely recognized for its broad optical absorption, efficient charge transport, and suitability for morphology regulation through additive-assisted strategies.[132]

The selected green solvents not only improve ecological safety but also feature higher boiling points (66 °C to 89 °C) compared to CF (61 °C). As depicted in **Figure 3-1b**, blending these co-solvents into the casting solution slows down solvent evaporation, thereby extending the solution-to-film transformation time. This allows for enhanced molecular diffusion and structural rearrangement during film formation.[127, 128] Such delayed drying is expected to influence polymer chain packing, domain development, and phase separation, all of which play critical roles in charge carrier behavior and overall device efficiency. By combining mixed-solvent processing with a volatile solid additive—dithieno[3,2-b:2′,3′-d]thiophene (DTT)—our approach aims to achieve optimized film morphology while avoiding residual additives in the active layer.

In the sections that follow, we present a systematic evaluation of how these co-solvent systems affect key parameters including the boiling point–volatility relationship, optical behavior, intermolecular organization, charge recombination dynamics, and photovoltaic performance in PM6:PY-IT-based All-PSCs.

As presented in **Figure 3-1c** and **Table 3-1**, a comparison is made between the boiling points and saturated vapor pressures of four solvents: CF, THF, 2-MeTHF, and 3-MeTHF.[133] Among them, CF exhibits the lowest boiling point and highest vapor pressure, making it highly volatile. In contrast, the THF-based green alternatives show higher boiling points and reduced vapor pressures, with THF having the lowest boiling point within this group. These results imply that although the green solvents evaporate more slowly, their reduced toxicity and environmental impact make them viable replacements for CF in eco-conscious processing. The observed inverse correlation between boiling point and vapor pressure aligns with established thermodynamic principles. In addition, UV–visible absorption spectra of DTT-rich (100 wt%) blend films prepared using the different solvent systems reveal notable features in the near-infrared region, particularly around 800 nm—a region critical for efficient light absorption in all-polymer solar cells. Blends processed with THF-based solvents (THF, 2-MeTHF, and 3-MeTHF) show significantly stronger absorption in this spectral region compared to the CF-based reference.

Two distinct absorption bands are observed: a longer-wavelength 0–0 peak (~800 nm), and a slightly blue-shifted 0–1 peak. The 0–0 transition corresponds to the excitation from the vibrational ground state to the electronic excited state without vibrational excitation, while the 0–1 peak reflects an excitation involving vibrational energy.[134] A relatively stronger 0–0 peak, as seen in the THF-derived blends, is often indicative of enhanced molecular order and more efficient π–π stacking—morphological

doi:10.6342/NTU202502276

traits known to benefit charge transport and photovoltaic efficiency in All-PSCs. Collectively, these results not only demonstrate the optical advantages of using green co-solvents but also underscore their capability to serve as high-performance, sustainable alternatives to CF in all-polymer solar cell fabrication.

To gain deeper insight into polymer interactions in solution, variable-temperature UV–Vis absorption measurements were conducted for four solvent systems: pure chloroform (CF), CF blended with THF, CF with 2-MeTHF, and CF with 3-MeTHF. As illustrated in **Figures 3-1e** and **3-1f**, two key absorption features—around 600 nm (peak A) and 800 nm (peak B)—show a gradual reduction in intensity as the temperature increases. Notably, this decrease is much more pronounced in the CF-only solution than in the three co-solvent systems. This trend suggests that polymers dissolved solely in CF exhibit weaker or more transient aggregation, making them more susceptible to thermal disruption. In contrast, the presence of THF, 2-MeTHF, or 3-MeTHF leads to greater thermal resilience in the absorption spectra, implying stronger intermolecular forces or pre-aggregation in solution. These enhanced interactions in the liquid state likely contribute to more efficient molecular organization during film formation.

This interpretation aligns well with the UV–Vis absorption spectra of the corresponding solid films (**Figure 3-1d**), where blends processed with THF-based co-solvents display a more prominent 0–0 absorption peak near 800 nm—a signature of improved π–π stacking and molecular order. Thus, the superior film morphologies observed in devices using co-solvent blends can be partly attributed to the stronger and more favorable polymer-polymer interactions present in solution before deposition.

doi:10.6342/NTU202502276

3.3.2 Morphology and molecular stacking behavior

To further clarify the relationship between aggregation behavior in solution and the resulting solid-state morphology, grazing-incidence wide-angle X-ray scattering (GIWAXS) was employed to analyze the molecular packing characteristics of active layers processed with different solvent systems. As shown in the out-of-plane (OOP) scattering profiles (**Figure 3-4a**), all blend films exhibited clear (100) and (010) diffraction peaks, corresponding to lamellar side-chain stacking and π–π stacking, respectively. When compared to the film processed using chloroform alone, the blends fabricated with co-solvent systems (CF+THF, CF+2-MeTHF, and CF+3-MeTHF) displayed slightly reduced lamellar d-spacings based on the (100) peak positions. This contraction suggests a denser and more compact packing of the side chains, reflecting a higher degree of molecular ordering—likely a result of the more stable intermolecular interactions present in solution, as indicated by the variable-temperature UV–Vis absorption results. Additionally, examination of the (010) diffraction peak revealed that the crystal coherence length (CCL)—determined from the full width at half maximum (FWHM)—was significantly greater in the mixed-solvent blends than in the CF-only film (**Figure 3-5a**, **Table 3-2**). The increase in CCL signifies enhanced crystallinity and longer-range ordering along the π–π stacking direction, which is beneficial for efficient charge carrier transport. On the other hand, the in-plane GIWAXS patterns showed negligible variation among the four solvent systems, indicating that the structural improvements primarily occur in the vertical (OOP) orientation. This anisotropic molecular organization suggests that the use of co-solvents mainly influences the vertical alignment of polymer chains, a factor that plays a crucial role in charge extraction for vertically structured devices such as All-PSCs.

These findings validate that incorporating high-boiling-point, environmentally

doi:10.6342/NTU202502276

friendly co-solvents not only influence polymer aggregation behavior in solution but also promotes improved molecular packing and enhanced crystallinity within the resulting solid-state films. This combined morphological refinement plays a crucial role in driving the superior photovoltaic performance observed in the devices.

To gain deeper insight into how these solvent systems affect morphology evolution, we further assessed the miscibility between PM6 and PY-IT using contact angle measurements and Flory–Huggins interaction parameters ($\chi_{D:A}$).[135] A lower $\chi_{D:A}$ value indicates stronger compatibility between donor and acceptor components, which typically results in more controlled phase separation and a more optimal nanoscale morphology.[136] As shown in **Table 3-3**, the calculated χ values reveal a distinct trend: the CF-only system yields the highest $\chi_{D:A}$, suggesting poor miscibility between PM6 and PY-IT. This is likely due to chloroform's relatively low boiling point (61 °C), which causes rapid solvent evaporation and limits molecular interaction time during film formation. The introduction of higher boiling point co-solvents—such as THF (66 °C), 2-MeTHF (80 °C), and 3-MeTHF (89 °C)—effectively slows down the evaporation rate, prolonging the solution-to-solid transition and allowing more time for inter-diffusion and self-organization of the donor and acceptor molecules. This improved dynamic is reflected in the progressively lower $\chi_{D:A}$ values, indicating better miscibility.

This miscibility trend is further supported by the optical absorption spectra, where mixed-solvent-processed films display sharper vibronic structures and more intense 0–0 transitions—signatures of enhanced molecular ordering. It is also consistent with GIWAXS results, which demonstrate tighter π–π stacking and improved crystallinity. Collectively, these observations indicate that the use of high-boiling-point co-solvents facilitates more homogeneous donor–acceptor mixing, resulting in well-ordered phase morphology that is favorable for efficient charge generation and transport.

To further validate the influence of donor–acceptor miscibility on the phase morphology of the active layer, grazing-incidence small-angle X-ray scattering (GISAXS) was employed to assess domain sizes in PM6:PY-IT blends prepared using various solvent systems.[137] Domain size was estimated using correlation length (ξ) fitting, and the resulting trend is as follows: CF-only (ξ = 6.58 nm) > CF+2-MeTHF (ξ = 5.80 nm) ≈ CF+THF (ξ = 5.69 nm) > CF+3-MeTHF (ξ = 3.85 nm), as shown in **Figure 3-5d**. This pattern closely mirrors the previously discussed χ values. The pure CF system, which exhibited the highest χ value due to its low boiling point and rapid evaporation, resulted in the largest domain size—indicative of poor miscibility and early phase separation. Conversely, the CF+3-MeTHF blend, with the lowest χ value and highest boiling point, enabled more complete mixing between PM6 and PY-IT during film formation, leading to smaller, more uniformly distributed domains. The blends processed with CF+THF and CF+2-MeTHF showed intermediate values for both domain size and miscibility. These findings strongly support the conclusion that regulating solvent evaporation dynamics through the use of high-boiling-point green co-solvents enhances donor–acceptor miscibility. This, in turn, helps suppress excessive phase separation and facilitates the formation of finely interpenetrated networks, which is advantageous for efficient exciton dissociation and charge transport—ultimately contributing to improved device performance.

To complement the GISAXS results, atomic force microscopy (AFM) was used to examine the surface morphology of the active layers. As shown in **Figure 3-5e**, noticeable differences in surface roughness were observed across the solvent systems. The CF-only film exhibited the highest root-mean-square (RMS) roughness of 2.52 nm, suggesting significant vertical phase separation and surface irregularity. In contrast, the film processed with CF+3-MeTHF displayed the smoothest surface with an RMS

doi:10.6342/NTU202502276

roughness of just 0.73 nm, indicating a more homogeneous and finely mixed morphology. Films processed with CF+THF and CF+2-MeTHF exhibited intermediate roughness values of 1.29 nm and 1.38 nm, respectively.

The consistent trends observed in AFM surface roughness, GISAXS-derived domain size, and calculated Flory–Huggins interaction parameters collectively reinforce the conclusion that employing green co-solvents with higher boiling points improves miscibility between PM6 and PY-IT. This enhanced miscibility results in a finer phase-separated morphology with smoother film surfaces, which is highly beneficial for charge generation and transport in All-PSC devices.

3.3.3 Photovoltaic performance and charge recombination properties

To validate the structural and morphological insights obtained, photovoltaic devices were fabricated using various solvent systems and characterized accordingly. The devices employed an inverted architecture of ITO/ZnO/active layer/MoO_3/Ag.[138] As detailed in **Table 3-4** and illustrated in **Figure 3-9a**, the device processed with pure chloroform (CF) delivered the lowest power conversion efficiency (PCE) of 16.72%, alongside reduced open-circuit voltage (V_{oc} = 0.930 V) and short-circuit current density (J_{sc} = 25.14 mA cm^{-2}). This underperformance can be attributed to the formation of large phase-separated domains in the CF-only system, which results in fewer donor–acceptor (D/A) interfaces. These oversized domains likely surpass the exciton diffusion length, leading to inefficient exciton separation and increased geminate recombination losses. On the other hand, while the CF+3-MeTHF-based device showed the smoothest surface morphology (RMS = 0.73 nm) and the smallest domain size (ξ = 3.85 nm), it achieved only a moderate PCE of 16.86% and a comparatively lower fill

doi:10.6342/NTU202502276

factor (*FF* = 70.60%). This is likely due to excessive miscibility between the donor and acceptor materials, resulting in overly mixed domains. Although this condition increases D/A interface density, it may compromise continuous charge transport pathways, thereby enhancing non-geminate recombination.

In contrast, devices processed with CF+THF and CF+2-MeTHF exhibited the best overall performance, both achieving PCEs above 17.1% with well-balanced photovoltaic parameters. These blends demonstrated moderate domain sizes and optimal miscibility, which collectively promoted efficient exciton generation, dissociation, and charge transport. The observed enhancement in J_{sc} is consistent with the stronger absorption around 800 nm in UV–Vis spectra and the thermally stable aggregation behavior confirmed through variable-temperature UV–Vis analysis. Furthermore, GIWAXS measurements indicated improved molecular packing and crystallinity in these films, contributing to better *FF* and device efficiency. Altogether, these results highlight that achieving intermediate miscibility and regulated polymer aggregation—as observed in the THF- and 2-MeTHF-based systems—yields the most favorable active layer morphology for high-efficiency all-polymer solar cells.

As shown in **Figure 3-9c**, devices processed with CF+THF and CF+2-MeTHF exhibit notably stronger external quantum efficiency (EQE) responses across the full visible to near-infrared spectrum (400–900 nm), with a marked enhancement near 800 nm—correlating well with the improved absorption features observed in their corresponding UV–Vis spectra. In contrast, the device based solely on CF demonstrates the weakest EQE, particularly in the longer wavelength region (~750–850 nm), reinforcing the conclusion that insufficient miscibility and coarse phase separation reduce both optical absorption and charge collection efficiency. Interestingly, while the CF+3-MeTHF-based device shows a slightly higher EQE response at shorter

doi:10.6342/NTU202502276

wavelengths, it suffers a relative decline in the near-infrared region, which is likely due to an excessively mixed morphology that disrupts long-range charge transport. Moreover, the J_{sc} values obtained by integrating the EQE spectra align well with those derived from the J–V measurements, further validating the consistency of the data.

To examine how the concentration of the solid additive DTT affects device performance, additional control experiments were performed using 133 wt% and 166 wt% DTT within the same PM6:PY-IT (1.2:1) blend ratio under identical solvent conditions. **Figure 3-11a** and **Table 3-5** summarize the results. Although all tested concentrations yielded devices with comparable performance, the 100 wt% DTT condition consistently led to the highest PCE across all solvent systems. Notably, for CF, CF+THF, CF+2-MeTHF, and CF+3-MeTHF, the 100 wt% DTT formulations either achieved the best or closely matched the best performance, while also offering more balanced V_{oc}, J_{sc}, and FF values relative to higher additive loadings.

Increasing the DTT concentration beyond 100 wt% did not yield further benefits and, in some cases, resulted in marginal declines in fill factor or greater variability in V_{oc}, possibly due to disruptions in optimal film morphology or phase separation. Based on these observations, the remainder of this study will focus on devices fabricated with 100 wt% DTT, with emphasis placed on investigating how variations in solvent system composition influence active layer morphology and overall photovoltaic performance.

To further enhance device efficiency, ternary solar cells were developed by incorporating a third component—either Y6 or D18—into the PM6:PY-IT binary system. As shown in **Table 3-4** and **Figure 3-9b**, both ternary blends achieved notable improvements in PCE, reaching 17.57% for the Y6-based device and 17.35% for the D18-based one. These enhancements are primarily driven by a substantial increase in J_{sc}, which rose to 26.12 mA cm^{-2} and 26.05 mA cm^{-2}, respectively. The elevated J_{sc} is

doi:10.6342/NTU202502276

attributed to extended light absorption and broader spectral coverage introduced by the third component, as well as potentially improved charge separation and transport facilitated by the optimized morphology enabled by the mixed solvent systems. When benchmarked against recent literature on PM6:PY-IT-based all-polymer solar cells (**Figure 3-11b**, **Table 3-6**), the ternary devices reported here exhibit superior PCE and J_{sc} values. These findings underscore the effectiveness of our green co-solvent strategy in enhancing light harvesting and charge transport properties. The use of high-boiling-point, environmentally benign solvents such as THF, 2-MeTHF, and 3-MeTHF proves instrumental in refining film morphology, improving donor–acceptor miscibility, and achieving favorable phase separation—all of which contribute directly to improved device performance. Overall, this approach enables both binary and ternary devices to achieve record-level efficiencies while also offering a scalable, eco-friendly processing pathway for next-generation high-efficiency all-polymer solar cells.

Three complementary techniques were employed to deepen our understanding of charge recombination mechanisms. First, the relationship between short-circuit current density (J_{sc}) and incident light intensity (P_{light}) was analyzed. All four devices exhibited α values approaching unity, suggesting that bimolecular recombination was largely suppressed.[139] In parallel, the slope of the open-circuit voltage (V_{oc}) plotted against the natural logarithm of light intensity ($\ln(P_{light})$) fell within the range of 1.18 to 1.43 (kT/q) for each device, indicating the presence of both bimolecular and trap-assisted recombination processes, but with no major differences observed across solvent systems.[139] To better distinguish the impact of solvent environment on recombination, we further assessed charge dissociation efficiency (P_d) and charge collection efficiency (P_c) using photocurrent measurements at varying effective voltages (V_{eff}).[140] As reported in **Table 3-7**, the device processed with chloroform alone

doi:10.6342/NTU202502276

exhibited reduced P_d (95.81%) and P_c (82.96%) values relative to those prepared with mixed solvents. Notably, the CF+2-MeTHF-based device achieved the highest P_c at 96.10%. These results suggest that the CF-only system experiences greater geminate and non-geminate recombination losses, which aligns with its larger domain sizes and limited donor–acceptor interfacial area.

Collectively, these recombination studies support the morphological findings: the CF-only blend, with its excessive phase separation, inhibits effective exciton dissociation and charge extraction, contributing to the reduced V_{oc} and J_{sc} observed. Conversely, while the CF+3-MeTHF blend forms smaller domains and smoother films, its overly mixed morphology may compromise the continuity of charge transport pathways. By contrast, the CF+THF and CF+2-MeTHF systems appear to strike an optimal balance—effectively suppressing recombination while maintaining robust charge transport—which accounts for their superior PCEs among the solvent systems investigated.

3.3.4 Charge carrier dynamics and electrical characteristics

To gain further insight into exciton dissociation behavior, time-resolved photoluminescence (TRPL) measurements were performed on blend films prepared using different solvent systems.[141] As illustrated in **Figure 3-13a**, the PL decay curves show clear distinctions in carrier lifetimes among the four systems. The blend processed with chloroform alone displayed the longest photoluminescence lifetime (τ = 0.52 ns), indicating slower charge separation dynamics. In comparison, blends processed with THF (τ = 0.47 ns), 2-MeTHF (τ = 0.49 ns), and 3-MeTHF (τ = 0.51 ns) exhibited shorter decay times, suggesting more efficient exciton dissociation and faster

doi:10.6342/NTU202502276

charge transfer at the donor–acceptor interface. These results align with the higher exciton dissociation efficiencies (P_d) obtained from photocurrent measurements and reinforce the conclusion that mixed solvent systems promote improved interfacial morphology. The faster PL quenching observed in these blends suggests stronger D/A contact, facilitating ultrafast charge generation and minimizing geminate recombination losses.

To further investigate the origins of photocurrent differences and recombination effects, space-charge-limited current (SCLC) and photo-induced charge extraction by linearly increasing voltage (Photo-CELIV) techniques were used to assess charge transport properties.[142] As shown in **Figure 3-13c** and detailed in **Table 3-8**, both electron (μ_e) and hole (μ_h) mobilities increase progressively from the CF-based device to the 3-MeTHF-based device, indicating enhanced charge transport as a result of high-boiling-point solvent use. Notably, while the 3-MeTHF-based blend exhibited the highest individual mobilities, the devices based on THF and 2-MeTHF displayed more balanced transport characteristics, with μ_h/μ_e ratios close to unity (~1.1 and ~1.0, respectively). This balance is essential for minimizing space-charge buildup and reducing bimolecular recombination. In contrast, the CF-based device exhibited a more imbalanced carrier mobility ratio (μ_h/μ_e = 1.53), which likely contributes to its lower *FF* and higher recombination-related losses. These trends are corroborated by Photo-CELIV results (**Figure 3-13b**), which show a consistent order in overall device mobility (μ_{device}), with the THF- and 2-MeTHF-based devices again demonstrating both higher and more balanced transport properties. Collectively, these findings confirm that improved and balanced charge mobility—achieved through mixed solvent processing—is closely linked to the enhanced performance metrics observed, particularly higher J_{sc} and *FF*.

doi:10.6342/NTU202502276

To further validate the observed charge recombination and transport behaviors, transient photovoltage (TPV) and transient photocurrent (TPC) measurements were conducted. TPV provides insights into carrier lifetimes under open-circuit conditions, offering a window into the recombination dynamics.[143] In contrast, TPC assesses the timescale for charge extraction under short-circuit conditions.[144] As shown in **Figure 3-13d**, the device processed using only chloroform exhibited the shortest carrier lifetime (τ = 1.20 μs), suggesting higher recombination losses. On the other hand, devices based on THF and 2-MeTHF demonstrated substantially longer carrier lifetimes—7.42 μs and 3.32 μs, respectively—indicating reduced recombination and enhanced charge carrier stability. This trend is further supported by TPC data: the CF-based device showed the slowest charge extraction (τ = 0.80 μs), while THF- and 2-MeTHF-based devices achieved faster extraction times of 0.45 μs and 0.41 μs, respectively. These measurements collectively confirm that devices processed with mixed green solvents enable more efficient charge transport and significantly lower recombination rates.

To evaluate the degree of energetic disorder in the active layers, Urbach energy (E_U) was derived from the low-energy tail of the FTPS-EQE spectra (**Figure 3-14c**). E_U reflects the exponential decay of the absorption edge and is directly linked to the sharpness of the density of states (D.O.S.) near the band edge.[145] As illustrated in **Figure 3-13f**, the CF-based blend film shows the highest E_U value (~26 meV), which implies greater energetic disorder and a broader distribution of localized states. In contrast, the THF-, 2-MeTHF-, and 3-MeTHF-based blends exhibit noticeably lower E_U values, suggesting a more ordered electronic structure and a steeper band-edge slope. A reduction in E_U is commonly associated with fewer trap states and a diminished likelihood of recombination.[146]

These findings are in excellent agreement with earlier results from TPV/TPC,

doi:10.6342/NTU202502276

TRPL, and P_d/P_c analyses, reinforcing the conclusion that the use of high-boiling-point green co-solvents enhances molecular packing and reduces energetic disorder. Together, these improvements contribute to suppressed charge recombination and superior photovoltaic performance in all-polymer solar cells.

To gain deeper insight into the internal electric field and its influence on exciton dissociation, Mott–Schottky analysis was employed to determine the built-in potential (V_{bi}) of the devices. As illustrated in **Figure 3-13g**, the device processed with chloroform alone exhibits the lowest V_{bi} value (0.757 V), whereas the THF-, 2-MeTHF-, and 3-MeTHF-based devices show notably higher built-in potentials, with the THF-based device reaching up to 0.903 V. This elevated V_{bi} reflects a stronger internal electric field, which promotes more effective exciton separation and helps suppress charge recombination.

Complementing this, dielectric spectroscopy was conducted to evaluate the relative dielectric constant (ε_r) of the active layers. As shown in **Figure 3-13i**, devices fabricated with mixed solvent systems consistently exhibit higher ε_r values compared to the CF-only device. The increased dielectric constant observed in the THF-, 2-MeTHF-, and 3-MeTHF-based blends is indicative of improved molecular packing, which enhances dipole alignment and increases electric field screening within the film. This more favorable dielectric environment facilitates stronger Coulombic screening and more efficient exciton dissociation, thereby supporting better charge carrier mobility and overall device performance.

Trap densities (N_A) for the respective devices were further calculated using the Mott–Schottky plots, applying the following equation: [147]

$$N_A = \frac{-2}{q\varepsilon_0\varepsilon_r A}\left[\frac{dV}{dC^{-2}}\right]$$

doi:10.6342/NTU202502276

where q is the elementary charge, A is the active area of the device, and ε_0 and ε_r represent the vacuum permittivity and relative dielectric constant, respectively. According to **Figure 3-13h**, the device based on chloroform alone exhibited the highest trap density of 1.78×10^{17} cm^{-3}, pointing to a greater presence of defect states that can act as recombination centers. In contrast, the THF-, 2-MeTHF-, and 3-MeTHF-processed devices showed lower trap densities, ranging from 1.62 to 1.54×10^{17} cm^{-3}, suggesting that the mixed solvent formulations help minimize trap-state formation during the film drying process.

The observed reduction in trap-assisted recombination aligns well with other performance indicators, including extended carrier lifetimes (from TPV), improved exciton dissociation efficiencies, and enhanced V_{oc} and FF values for devices processed with green co-solvents. These findings provide additional evidence that the green solvent strategy not only improves morphology and charge mobility but also contributes to energetically cleaner active layers with fewer defect states, ultimately translating to superior photovoltaic performance.

3.4 Conclusion

In this study, we present a sustainable and effective approach for enhancing the morphology and performance of All-PSCs through the use of eco-friendly mixed co-solvent systems paired with a volatile solid additive (DTT). Utilizing PM6 as the donor and PY-IT as the acceptor, we systematically explored how combining chloroform (CF) with green solvents—THF, 2-MeTHF, and 3-MeTHF—affects the solution-to-solid transition dynamics. This in turn influences active layer morphology, phase separation behavior, and charge transport characteristics.

doi:10.6342/NTU202502276

Our findings reveal that compared to the CF-only system, co-solvent blends—particularly those using CF+THF and CF+2-MeTHF—significantly enhance polymer miscibility and molecular packing, reduce phase domain sizes, lower trap densities, and achieve more balanced charge carrier mobilities. These morphological refinements translate into higher exciton dissociation efficiencies, reduced recombination losses, and improved charge extraction, enabling devices to reach PCEs exceeding 17%.

Moreover, measurements of energetic disorder and dielectric properties confirm that mixed solvent processing leads to a narrower density of states and increased built-in electric fields, both of which further contribute to the overall efficiency improvements.

Beyond performance gains, this co-solvent strategy offers an environmentally responsible and scalable route for manufacturing high-efficiency All-PSCs. Overall, our work establishes a strong correlation between processing conditions, morphological evolution, and device performance—offering valuable guidance for future solvent engineering in organic photovoltaic technologies.

Figures

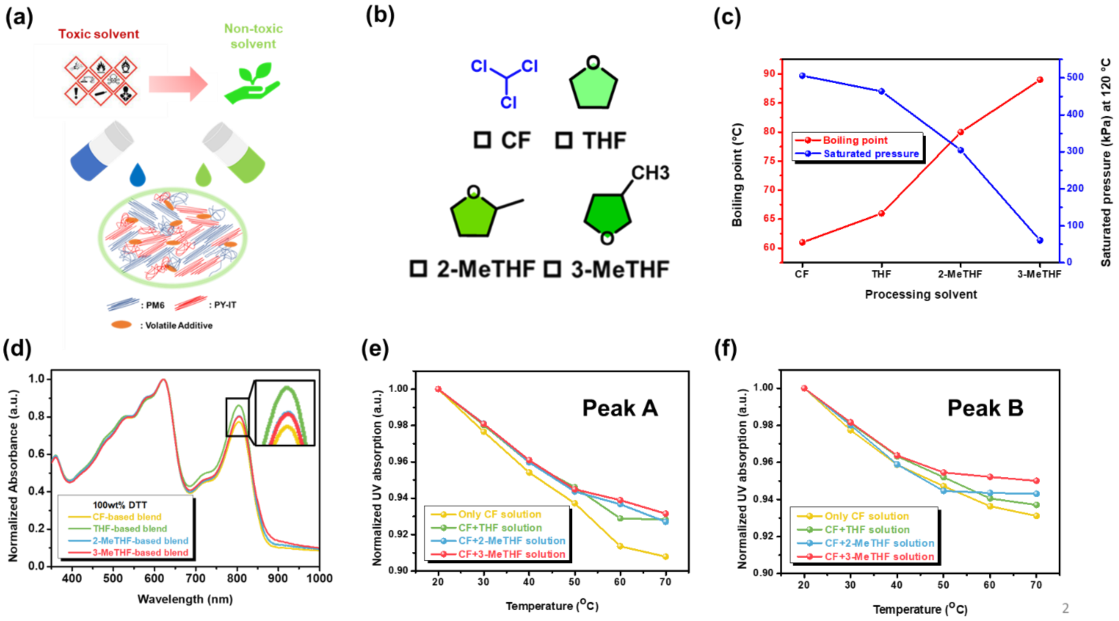

Figure 3-1 (a) Schematic illustration of the transition from toxic chloroform-based to eco-friendly mixed-solvent systems for film fabrication. (b) Chemical structures of CF, THF, 2-MeTHF, and 3-MeTHF. (c) Boiling point and saturated vapor pressure trends of the solvents used. (d) UV-Vis absorption spectra of blend films prepared using different co-solvent systems. (e–f) Variable-temperature UV-Vis spectra at 600 nm and 800 nm, showing that the mixed-solvent systems exhibit improved thermal stability of polymer–polymer interactions compared to only CF.

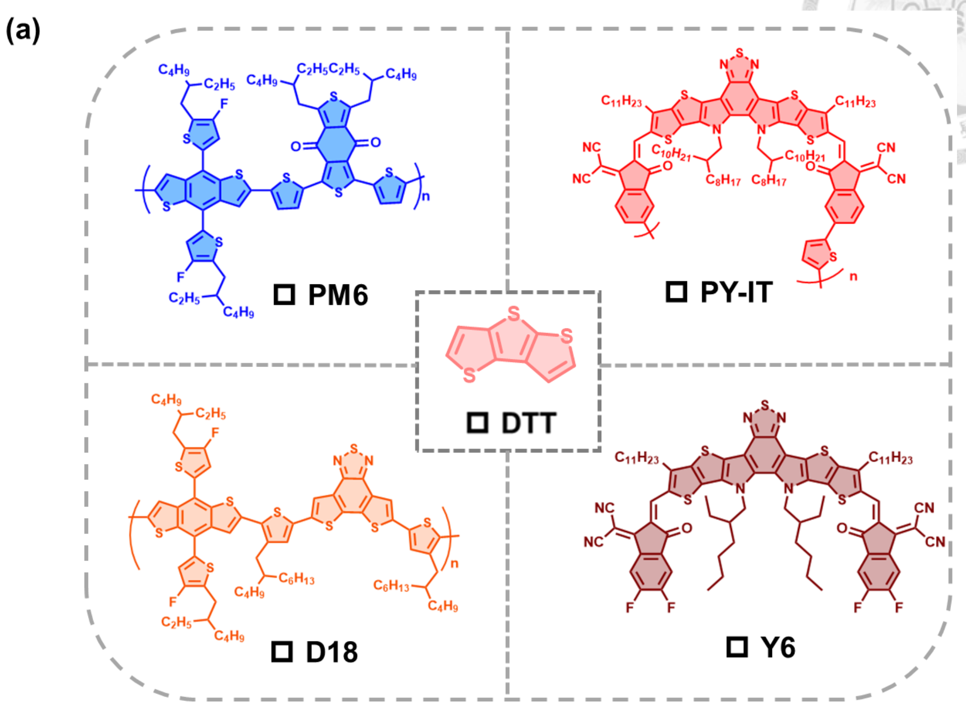

Figure 3-2 Chemical structures of the donor, acceptor, and solid additive materials used in this study.

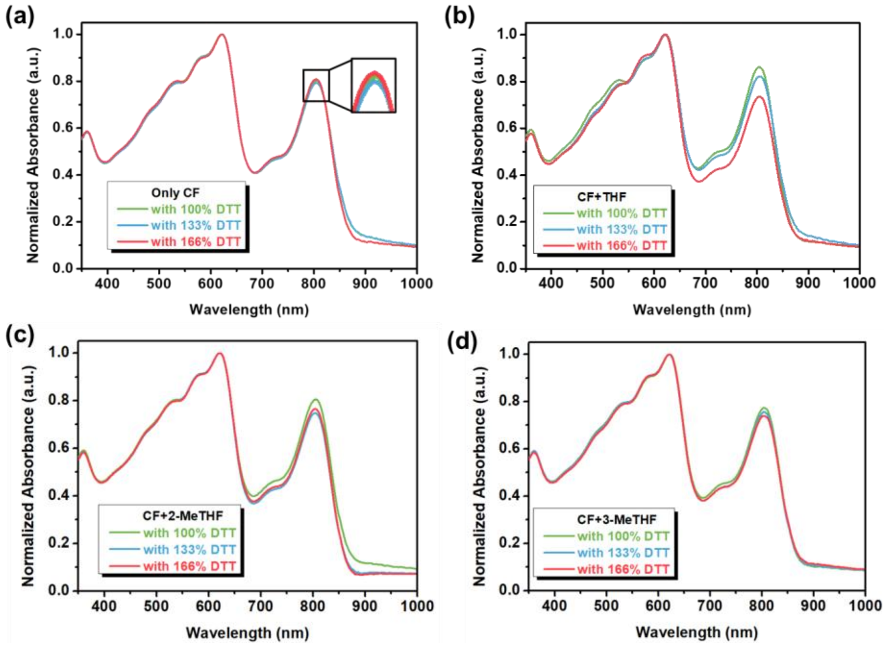

Figure 3-3 (a–d) Normalized UV–Vis absorption spectra of PM6:PY-IT blend films with 100 wt%, 133 wt%, and 166 wt% DTT under different co-solvent systems.

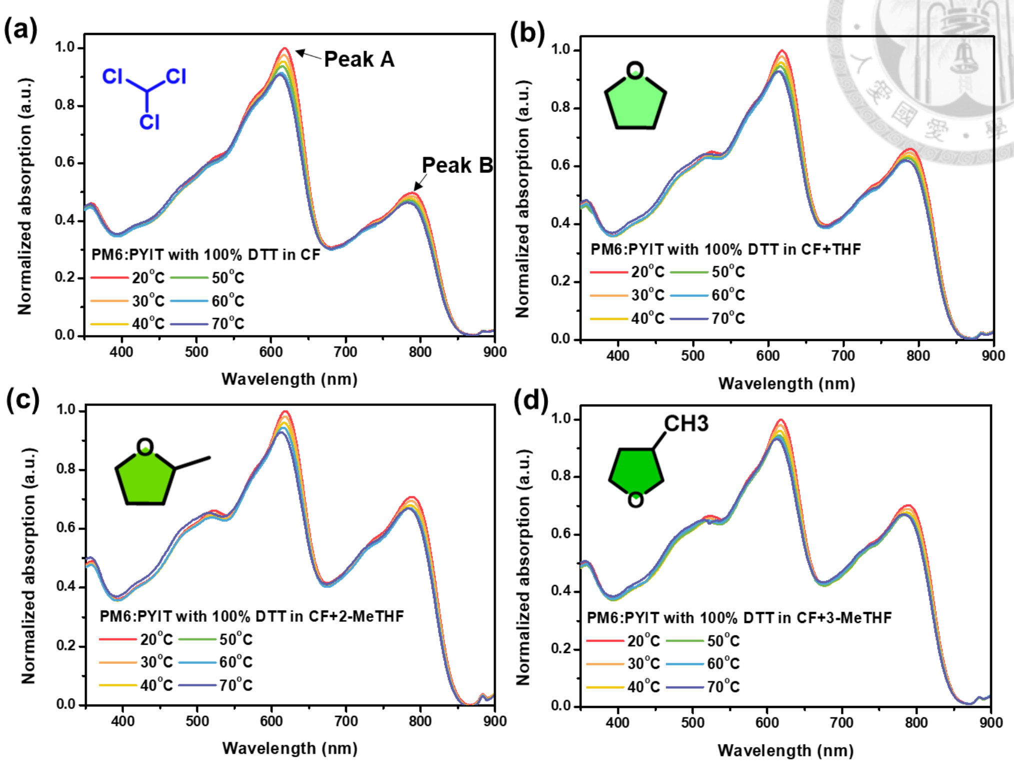

Figure 3-4 (a-d) Variable-temperature UV–Vis absorption spectra of PM6:PY-IT solutions using CF, CF+THF, CF+2-MeTHF, and CF+3-MeTHF as co-solvents, each with 100 wt%, 133 wt%, and 166 wt% DTT.

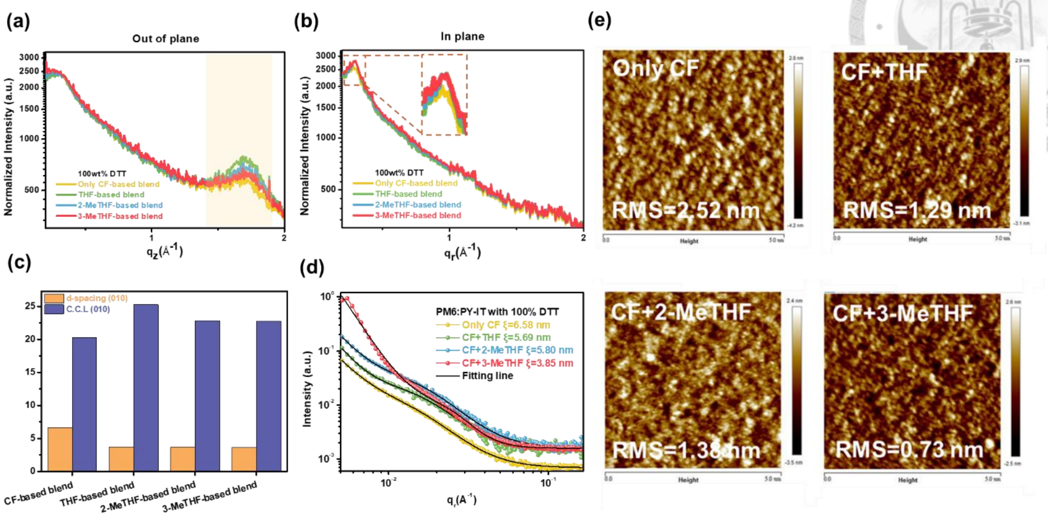

Figure 3-5 (a–b) GIWAXS 1D line-cut profiles along the (a) out-of-plane and (b) in-plane directions, revealing differences in lamellar (100) and π–π stacking (010) features. (c) Summary of lamellar d-spacing (100) and crystal coherence length (C.C.L.) from GIWAXS out-of-plane peaks. (d) Domain sizes derived from GISAXS measurements using correlation length (ξ). (e) AFM height images of the active layer surfaces and corresponding root-mean-square (RMS) roughness values.

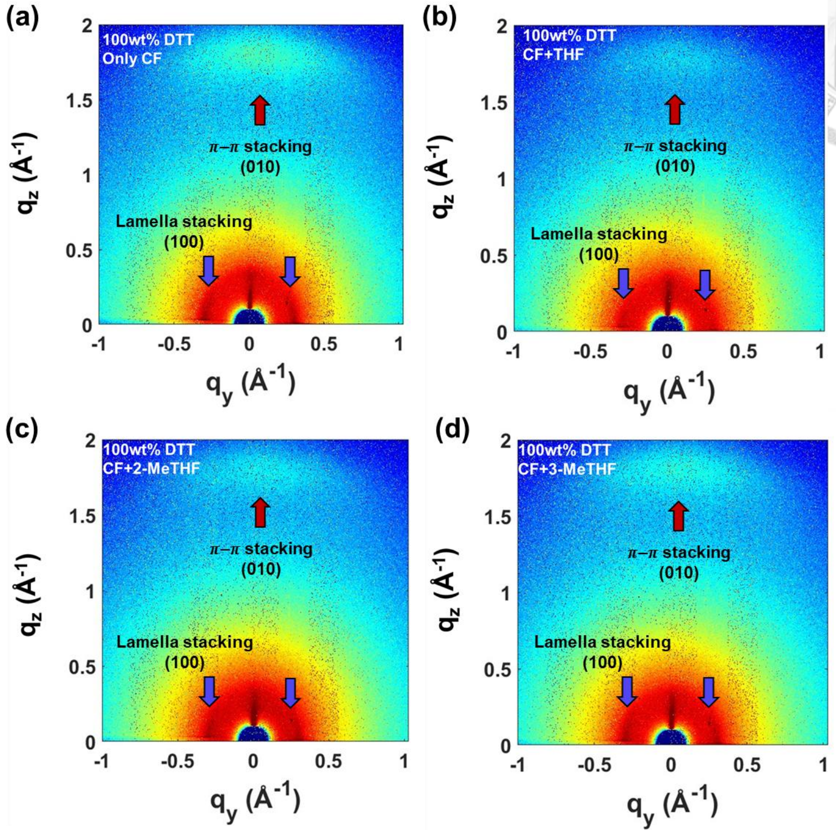

Figure 3-6 (a-d) 2D GIWAXS patterns of PM6:PY-IT blend films processed with different co-solvent systems (with 100 wt% DTT).

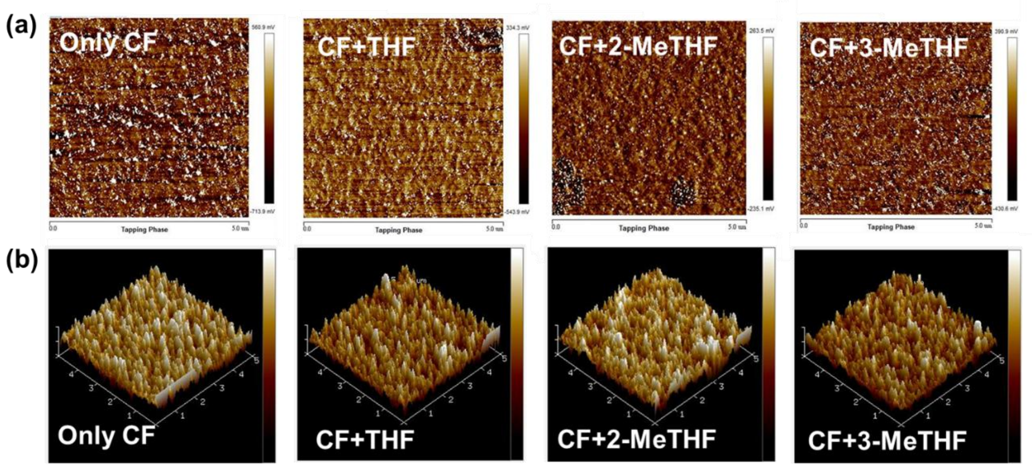

Figure 3-7 AFM phase and topography images of PM6:PY-IT blend films processed with different co-solvent systems (100 wt% DTT).

doi:10.6342/NTU202502276

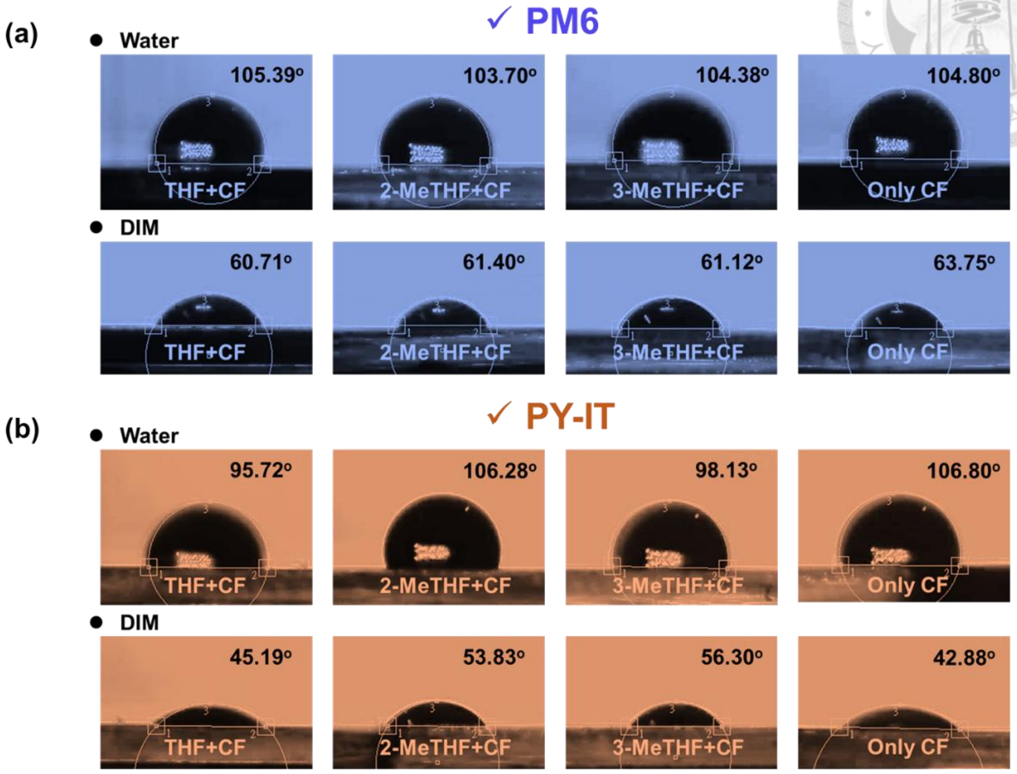

Figure 3-8 Contact angle measurements of donor (PM6) and acceptor (PY-IT) films using water and diiodomethane (DIM).

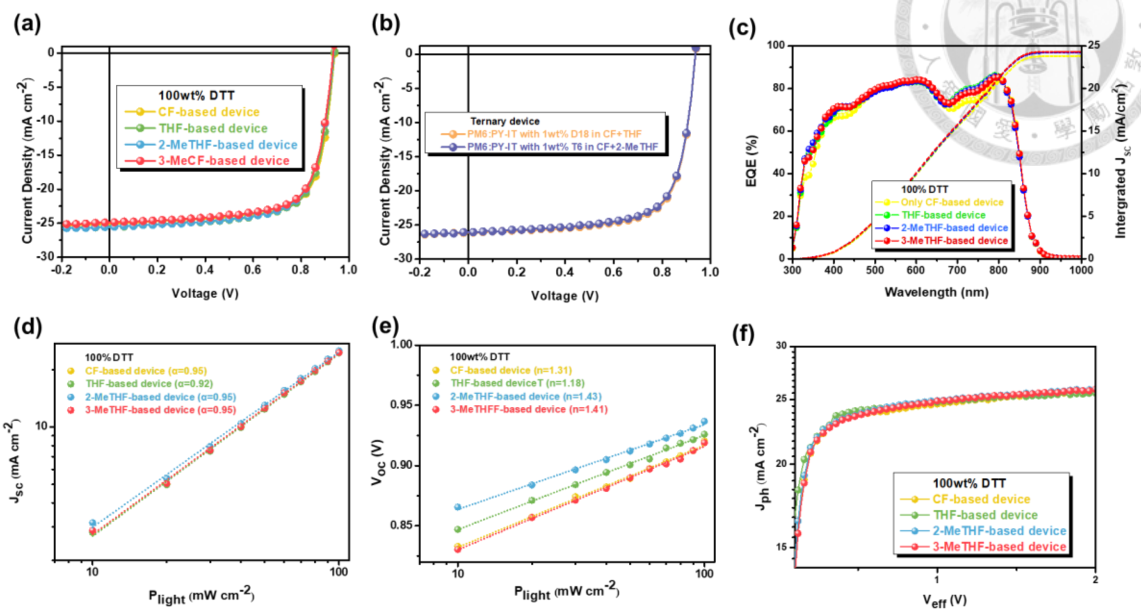

Figure 3-9 (a) *J*–*V* curves of PM6:PY-IT binary devices fabricated with different solvent systems under 100 mW cm^{-2} illumination. (b) *J*–*V* characteristics of ternary devices incorporating either 1 wt% D18 or Y6 into the mixed-solvent systems. (c) External quantum efficiency (EQE) spectra of the binary devices (d) Light intensity dependence of J_{sc} for all devices; fitted α values close to 1 suggest negligible bimolecular recombination. (e) V_{oc} versus ln(P_{light}) plots for all devices; the fitted slope ($n \times kT/q$) indicates the recombination mechanism (bimolecular vs. trap-assisted). (f) J_{ph}–V_{eff} curves illustrating charge dissociation and collection performance.

doi:10.6342/NTU202502276

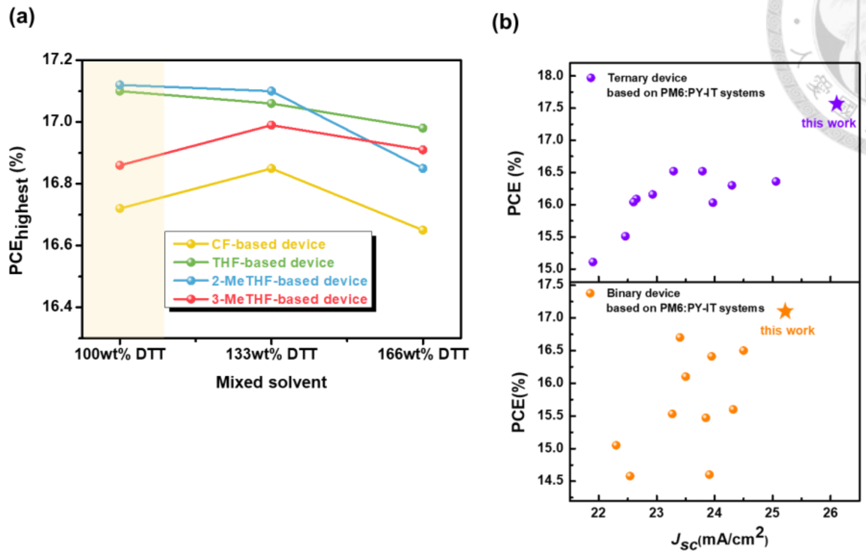

Figure 3-10 (a) PCE comparison of PM6:PY-IT devices processed with different co-solvent systems (CF, CF+THF, CF+2-MeTHF, CF+3-MeTHF) under three DTT concentrations (100, 133, and 166 wt%). (b) Benchmark comparison of binary and ternary PM6:PY-IT devices reported in literature.

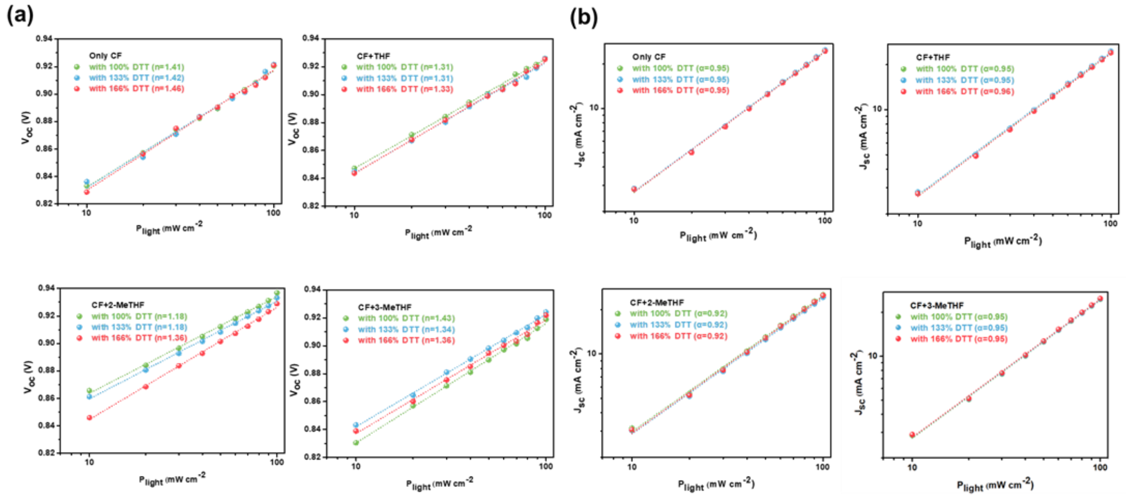

Figure 3-11 Light-intensity-dependent analyses of PM6:PY-IT blend processed with different co-solvent systems (CF, CF+THF, CF+2-MeTHF, CF+3-MeTHF) under 100%, 133%, and 166% DTT concentrations.

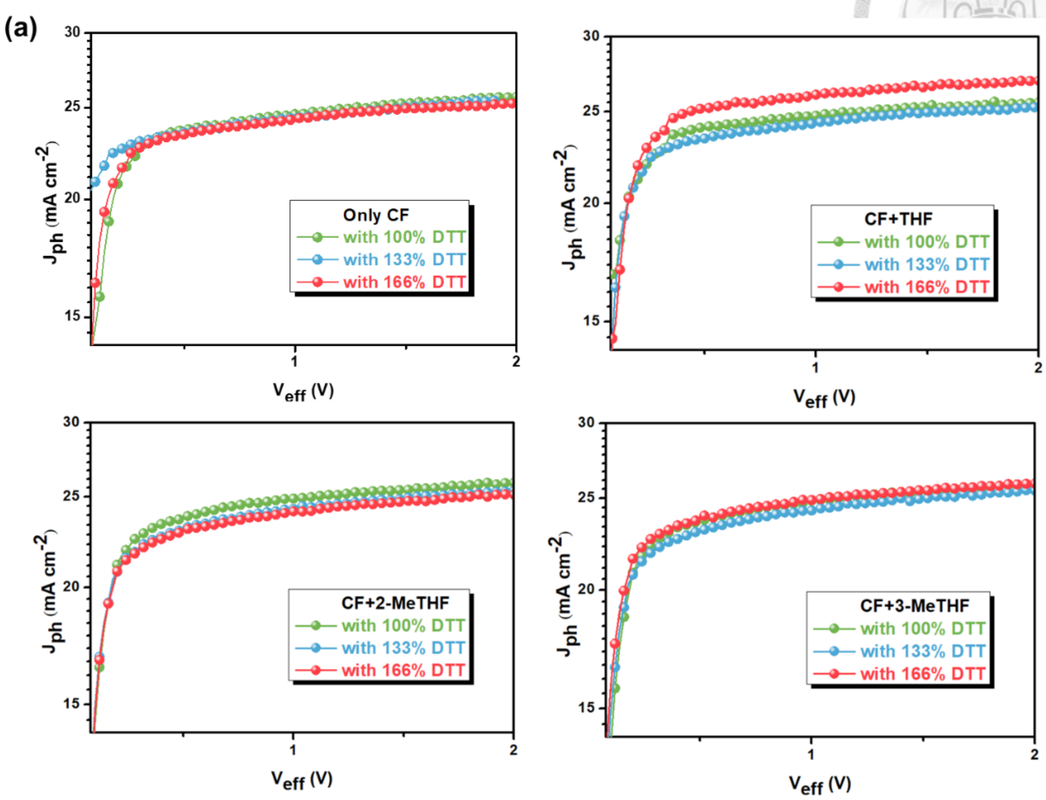

Figure 3-12 Photocurrent density (J_{ph}) versus effective voltage (V_{eff}) plots of PM6:PY-IT devices processed with different DTT concentrations (100%, 133%, and 166%)

doi:10.6342/NTU202502276

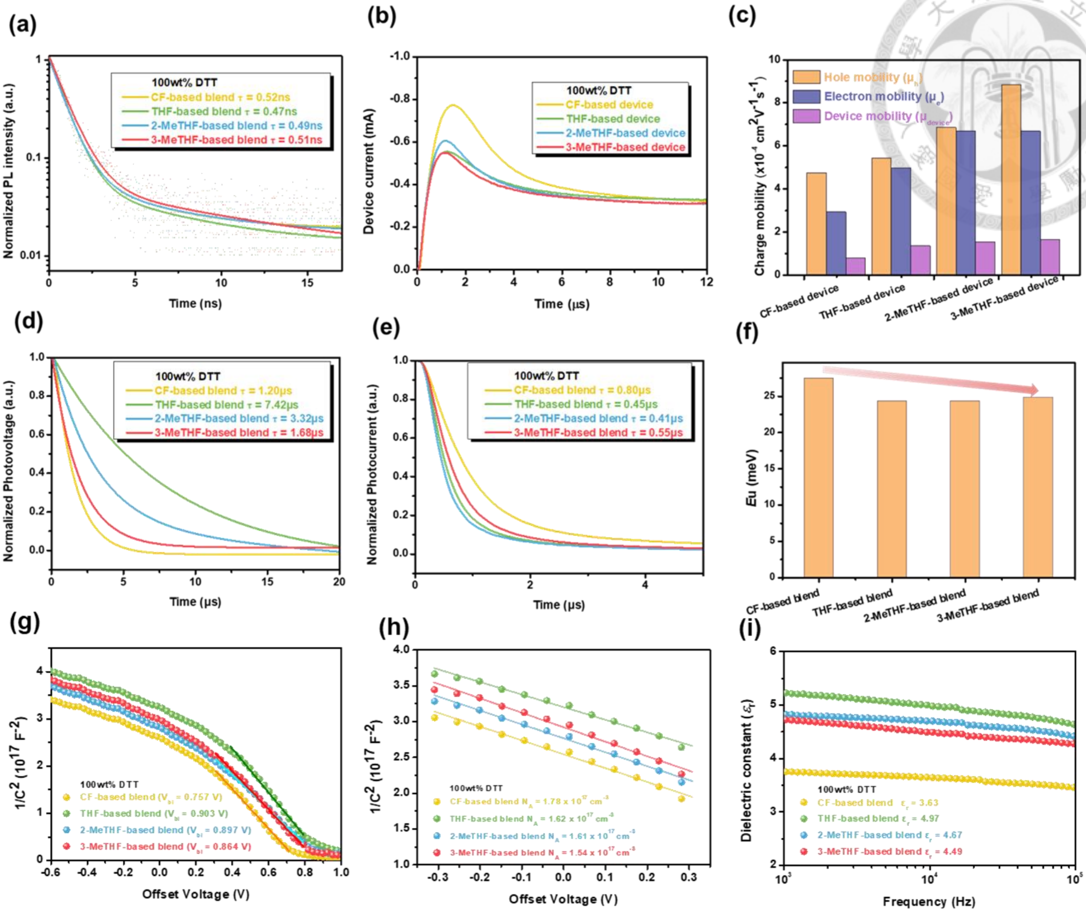

Figure 3-13 (a) Time-resolved photoluminescence (TRPL) spectra of the blend films, showing shorter lifetimes for the mixed-solvent systems, indicative of faster exciton dissociation. (b) Photo-CELIV transient photocurrent curves used to evaluate device mobility, showing enhanced charge transport with co-solvent processing. (c) Summary of hole mobility (μ_h), electron mobility (μ_e), and device mobility (μ_{device}) extracted via SCLC and Photo-CELIV methods. (d) Transient photovoltage (TPV) measurements showing longer carrier lifetimes in mixed-solvent systems. (e) Transient photocurrent (TPC) decay curves indicating more efficient charge extraction in mixed-solvent-based devices. (f) Urbach energy (E_U) values derived from FTPS-EQE spectra. (g) Mott-Schottky plots used to extract built-in potential (V_{bi}). (h) Carrier density (N_A) estimation showing fewer trap states in co-solvent-processed devices. (i) Frequency-dependent dielectric constants (ε_r), where increased values suggest stronger

exciton dissociation capabilities in green solvent systems.

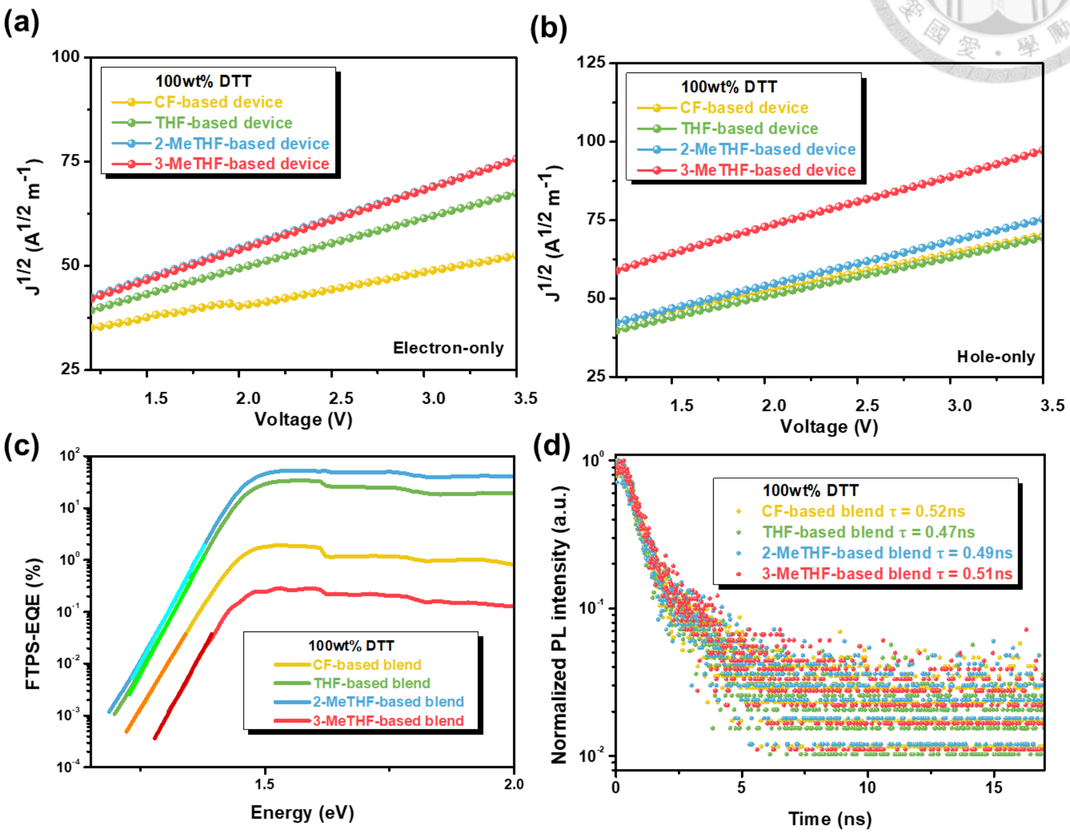

Figure 3-14 Charge transport and recombination characteristics of PM6:PY-IT devices processed with different mixed solvents and 100 wt% DTT. (a) Space-charge-limited current (SCLC) analysis of electron-only devices for extracting μ_e. (b) SCLC analysis of hole-only devices for extracting μ_h. (c) FTPS-EQE spectra indicating sub-bandgap response and energy disorder. (d) Time-resolved photoluminescence (TRPL) raw decay curves reflecting exciton lifetime behavior.

Tables

Table 3-1 Boiling points and saturated vapor pressures of CF, THF, 2-MeTHF, and 3-MeTHF at 120 °C.

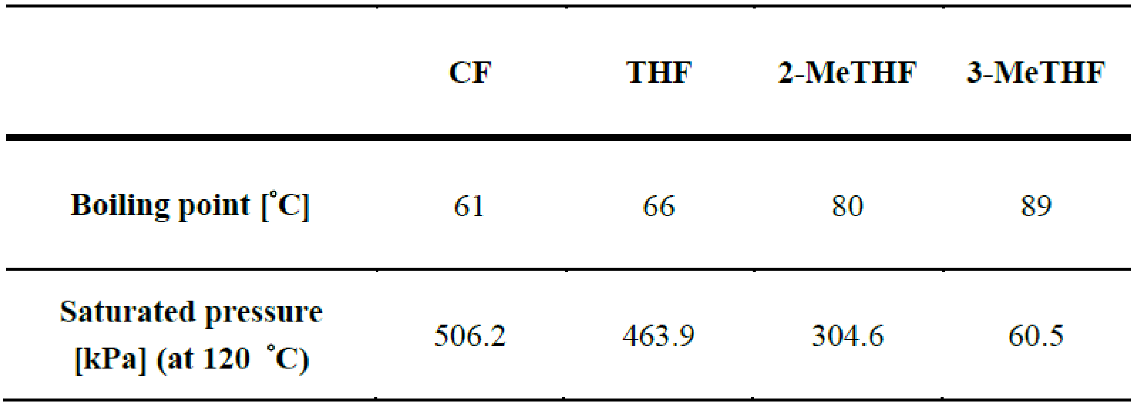

	CF	**THF**	**2-MeTHF**	**3-MeTHF**
Boiling point [˚C]	61	66	80	89
Saturated pressure [kPa] (at 120 ˚C)	506.2	463.9	304.6	60.5

doi:10.6342/NTU202502276

Table 3-2 Morphological parameters of the studied BHJ films derived from GIWAXS characterization.

Out of plane						In plane	
PM6:PY-IT	Peak location (100) ($Å^{-1}$)	d-spacing (100) (Å)	Peak location (010) ($Å^{-1}$)	d-spacing (010) (Å)	C.C.L (010) (Å)	Peak location (100) ($Å^{-1}$)	d-spacing (100) (Å)
CF-based blend	0.27	23.26	1.71	6.68	20.25	0.29	21.65
THF-based blend	0.29	21.65	1.70	3.69	25.27	0.29	21.65
2-MeTHF-based blend	0.29	21.65	1.71	3.68	22.83	0.29	21.65
3-MeTHF-based blend	0.29	21.65	1.72	3.66	22.76	0.29	21.65

Table 3-3 Contact angle measurements, surface energy parameters, and Flory–Huggins interaction parameter ($\chi_{D:A}$) for PM6 and PY-IT films using water and diiodomethane (DIM).

Active layer	**θ_{water} [°]**	**θ_{DIM} [°]**	**γ [mN m^{-1}]^{a}**
PM6 (Only CF)	104.8	63.75	35.65
PM6 (THF+CF)	105.39	60.71	37.24
PM6 (2-MeTHF+CF)	103.70	61.40	35.94
PM6 (3-MeTHF+CF)	104.38	61.12	36.38
PY-IT (Only CF)	106.80	42.88	44.55
PY-IT (THF+CF)	95.72	45.19	39.57
PY-IT (2-MeTHF+CF)	106.28	53.83	40.07
PY-IT (3-MeTHF+CF)	98.13	56.30	35.52

a The Surface tension of films were calculated through Owens method

PM6:PY-IT	**Only CF**	**THF+CF**	**2-MeTHF+CF**	**3-MeTHF+CF**
$\chi_{D:A}$	0.495	0.035	0.112	0.005

doi:10.6342/NTU202502276

Table 3-4 Photovoltaic parameters of PM6:PY-IT devices with different mixed solvent.

PM6:PY-IT(1.2:1) with 100wt% DTT	V_{oc} (V)	J_{sc} (mA cm^{-2})	*FF* (%)	**PCE$_{max}$ (PCE$_{avg}$) (%)**
100% CF	0.930 (0.930)	25.14 (24.61)	72.53 (69.54)	16.72 (15.89)
2% THF CF:THF(98:2)	0.938 (0.931)	25.12 (24.95)	72.56 (70.76)	17.10 (16.43)
2% 2-MeTHF CF:2-MeTHF(98:2)	0.938 (0.936)	25.45 (25.31)	71.76 (70.24)	17.12 (16.64)
2% 3-MeTHF CF:3-MeTHF(98:2)	0.935 (0.936)	25.55 (25.22)	70.60 (69.74)	16.86 (16.45)
Ternary device	V_{oc} (V)	J_{sc} (mA cm^{-2})	*FF* (%)	**PCE$_{max}$ (PCE$_{avg}$) (%)**
1wt% Y6 with 133wt% DTT in CF+2% 2-MeTHF	0.936 (0.932)	26.12 (25.25)	71.99 (71.03)	17.57 (16.70)
1wt% D18 with 100wt% DTT in CF+2% THF	0.936 (0.932)	26.05 (25.13)	71.27 (70.65)	17.35 (16.53)

Table 3-5 Photovoltaic parameters of PM6:PY-IT (1.2:1) based devices processed with 133 wt% and 166 wt% DTT using various co-solvent systems.

PM6:PY-IT(1.2:1) with 133wt% DTT	V_{oc} **(V)**	J_{sc} **(mA cm^{-2})**	***FF*** **(%)**	**PCE$_{max}$ (PCE$_{avg}$) (%)**
100% CF	0.937 (0.932)	24.86 (24.81)	72.51 (71.26)	16.85 (16.44)
2% THF **CF:THF(98:2)**	0.939 (0.936)	24.88 (24.69)	73.02 (71.47)	17.06 (16.50)
2% 2-MeTHF **CF:2-MeTHF(98:2)**	0.938 (0.933)	25.23 (25.20)	72.18 (69.69)	17.10 (16.39)
2% 3-MeTHF **CF:3-MeTHF(98:2)**	0.935 (0.935)	25.52 (25.43)	71.42 (69.85)	16.99 (16.55)
PM6:PY-IT(1.2:1) with 166wt% DTT	V_{oc} **(V)**	J_{sc} **(mA cm^{-2})**	***FF*** **(%)**	**PCE$_{max}$ (PCE$_{avg}$) (%)**
100% CF	0.938 (0.933)	24.34 (24.22)	73.07 (71.18)	16.65 (16.07)
2% THF **CF:THF(98:2)**	0.937 (0.935)	24.94 (24.61)	72.68 (71.66)	16.98 (16.49)
2% 2-MeTHF **CF:2-MeTHF(98:2)**	0.934 (0.930)	25.60 (25.15)	70.37 (66.50)	16.85 (15.56)
2% 3-MeTHF **CF:3-MeTHF(98:2)**	0.942 (0.937)	25.19 (24.88)	71.54 (69.09)	16.91 (16.06)

Table 3-6 Summary of recently reported all-PSCs based on PM6:PY-IT blend.

Photoactive layer (Binary device)	**V_{oc} (V)**	**J_{sc} (mA cm^{-2})**	**FF (%)**	**PCE (%)^b**	**Reference**
PM6:PY-IT with 1% CN	0.933	22.30	72.3	15.05	[148]
PM6: PY-IT with 2% CN	0.941	23.40	75.7	16.70	[149]
PM6:PY-IT without additive	0.945	23.91	64.8	14.60	[125]
PM6:PY-IT with DIB	0.945	24.32	68.0	15.60	[125]
PM6:PY-IT with DBCl	0.951	24.50	71.0	16.50	[125]
PM6:PY-IT with 1% CN	0.938	23.85	69.2	15.47	[150]
PM6:PY-IT with 1% CN	0.950	23.95	72.1	16.41	[150]
PM6:PY-IT with 2% CN	0.938	23.50	72.9	16.10	[151]
PM6:PY-IT with 1% CN	0.945	23.27	70.8	15.53	[152]
PM6:PY-IT with 1% CN	0.936	22.54	69.1	14.58	[152]
PM6:PY-IT With 100wt% DTT	**0.930**	**25.14**	**72.5**	**16.72**	**This work**
Photoactive layer (Ternary device)	**V_{oc} (V)**	**J_{sc} (mA cm^{-2})**	**FF (%)**	**PCE (%)^b**	**Reference**
PM6:PY-IT:J71 with 1% CN	0.940	23.29	75.2	16.52	[153]
PM6:PY-IT:PTQ10 with 1% CN	0.940	23.79	73.8	16.52	[154]
PM6:PY-IT:PDI-2T with 1% CN	0.950	23.97	70.5	16.03	[155]
PM6:PY-IT:BN-T with 1% CN	0.937	21.90	73.6	15.11	[132]
PM6:PY-IT:BN-T with 1% CN	0.960	22.65	74.3	16.09	[132]

PM6:PY-IT:BN-T with 1% CN	0.960	22.46	72.0	15.51	[132]
PM6:PY-IT:Tech-PCBM with 1% CN	0.960	22.93	73.6	16.16	[156]
PM6:PY-IT:PC$_{71}$BM with 1% CN	0.942	25.06	69.27	16.36	[157]
PM6:PY-IT:N2200 with 0.7% CN	0.947	22.60	74.90	16.04	[158]
PM6:PY-IT:PYCl-T with 1% CN	0.913	24.30	73.4	16.30	[159]
PM6:PY-IT:Y6 with 133wt% DTT	**0.936**	**26.12**	**71.99**	**17.57**	**This work**

doi:10.6342/NTU202502276

Table 3-7 Exciton dissociation probability (P_d) and charge collection efficiency (P_c) of PM6:PY-IT devices processed with 100%, 133%, and 166% DTT in four different solvent systems (CF, CF+THF, CF+2-MeTHF, and CF+3-MeTHF).

100wt% DTT	**CF**	**THF**	**2-MeTHF**	**3-MeTHF**
P_d (%)	95.81%	96.86%	96.21%	96.10%
P_c (%)	82.96%	84.91%	96.10%	83.99%
133wt% DTT	**CF**	**THF**	**2-MeTHF**	**3-MeTHF**
P_d (%)	95.26%	95.57%	95.57%	95.28%
P_c (%)	83.65%	83.55%	83.55%	82.93%
166wt% DTT	**CF**	**THF**	**2-MeTHF**	**3-MeTHF**
P_d (%)	96.10%	96.66%	95.93%	96.06%
P_c (%)	83.94%	84.96%	84.11%	84.52%

Table 3-8 Charge carrier mobilities of PM6:PY-IT devices processed with different solvent systems and 100 wt% DTT, including hole mobility (μ_h), electron mobility (μ_e), device mobility (μ_{device}), and the mobility ratio (μ_h/μ_e).

PM6:PY-IT	**Hole mobility μ_h (cm^{2}V^{-1}s^{-1})**	**Electron mobility μ_e (cm^{2}V^{-1}s^{-1})**	**Device mobility μ_{device} (cm^{2}V^{-1}s^{-1})**	**μ_h/μ_e**
THF-based device	5.43×10^{-4}	4.96×10^{-4}	7.70×10^{-5}	1.095
2-MeTHF-based device	6.85×10^{-4}	6.68×10^{-4}	1.35×10^{-4}	1.025
3-MeTHF-based device	8.85×10^{-4}	6.68×10^{-4}	1.53×10^{-4}	1.325
CF-based device	4.74×10^{-4}	2.92×10^{-4}	1.63×10^{-4}	1.531

CHAPTER 4

Conclusion and Future work

In this thesis, two complementary strategies—molecular design and processing engineering—were systematically investigated to enhance the performance and morphological quality of organic solar cells (OSCs), with a focus on all-polymer solar cells (All-PSCs). The research demonstrates that by tailoring both the chemical structure of the photoactive materials and the dynamics of film formation, it is possible to significantly improve device efficiency, reduce charge recombination, and promote environmentally responsible fabrication.

In **Chapter 2**, six isoindigo-based donor polymers were synthesized with variations in side-chain symmetry and backbone fluorination. The results clearly revealed that the incorporation of asymmetric side chains promotes more favorable face-on molecular orientation, enhances crystallinity, and improves interchain packing, which collectively contribute to superior charge mobility and fill factor. Moreover, the introduction of fluorine atoms along the polymer backbone was shown to rigidify the molecular structure through non-covalent F···S interactions, reduce energetic disorder, and enhance overall molecular packing. These effects not only improved the optoelectronic properties of the donor polymers but also mitigated the morphological sensitivity associated with side-chain configuration. The optimized polymers achieved a power conversion efficiency (PCE) exceeding 4.5%, highlighting the value of rational donor design based on donor–acceptor architecture and side-chain engineering.

doi:10.6342/NTU202502276

In the **Chapter 3**, a green co-solvent strategy was developed to address the challenge of morphology control in high-efficiency All-PSCs based on the PM6:PY-IT blend system. By partially replacing chloroform with environmentally friendly, high-boiling-point solvents such as THF and 2-MeTHF, and combining them with a volatile solid additive (DTT), the film formation kinetics were effectively regulated. This approach resulted in improved donor–acceptor miscibility, reduced phase separation scale, enhanced molecular packing, and suppressed trap formation. Devices processed with THF- and 2-MeTHF-based systems demonstrated significantly improved external quantum efficiency, balanced charge transport, and reduced charge recombination losses, achieving PCEs exceeding 17%. These findings confirm that green solvent processing not only enhances performance but also offers a sustainable route for scalable fabrication.

Overall, this work underscores the critical interplay between molecular structure and processing strategy in determining the morphology and function of OSCs. By integrating backbone engineering, side-chain modification, and controlled solution dynamics, this thesis provides both mechanistic understanding and practical guidance for the design of next-generation organic photovoltaic materials and processes. For future work, it would be valuable to explore the use of biodegradable or bio-sourced conjugated polymers and additives, as a further step toward fully sustainable solar cell systems. Additionally, long-term device stability under operational stress and environmental conditions should be more extensively evaluated to ensure real-world applicability.

doi:10.6342/NTU202502276

Reference

[1] Wang B-Y, Lee E-S, Oh Y-J, Kang HW. A silver nanowire mesh overcoated protection layer with graphene oxide as a transparent electrode for flexible organic solar cells. Rsc Advances. 2017;7(83):52914-22.

[2] Li S, Li Z, Wan X, Chen Y. Recent progress in flexible organic solar cells. Escience. 2023;3(1):100085.

[3] Seri M, Mercuri F, Ruani G, Feng Y, Li M, Xu Z-X, et al. Toward real setting applications of organic and perovskite solar cells: A comparative review. Energy Technology. 2021;9(5):2000901.

[4] Park S, Heo SW, Lee W, Inoue D, Jiang Z, Yu K, et al. Self-powered ultra-flexible electronics via nano-grating-patterned organic photovoltaics. Nature. 2018;561(7724):516-21.

[5] Liu C, Xiao C, Xie C, Li W. Flexible organic solar cells: Materials, large-area fabrication techniques and potential applications. Nano Energy. 2021;89:106399.

[6] Warren R, Privitera A, Kaienburg P, Lauritzen AE, Thimm O, Nelson J, et al. Controlling energy levels and Fermi level en route to fully tailored energetics in organic semiconductors. Nature communications. 2019;10(1):5538.

[7] Köhler A, Bässler H. Electronic processes in organic semiconductors: An introduction: John Wiley & Sons, 2015.

[8] Tress W, Beyer B, Ashari Astani N, Gao F, Meloni S, Rothlisberger U. Extended Intermolecular Interactions Governing Photocurrent–Voltage Relations in Ternary Organic Solar Cells. The journal of physical chemistry letters. 2016;7(19):3936-44.

[9] Xie Y, Wu H. Balancing charge generation and voltage loss toward efficient nonfullerene organic solar cells. Materials Today Advances. 2020;5:100048.

doi:10.6342/NTU202502276

[10] Schwarz C, Milan F, Hahn T, Reichenberger M, Kümmel S, Köhler A. Ground state bleaching at donor–acceptor interfaces. Advanced Functional Materials. 2014;24(41):6439-48.

[11] Kokil A, Yang K, Kumar J. Techniques for characterization of charge carrier mobility in organic semiconductors. Journal of polymer science part b: polymer physics. 2012;50(15):1130-44.

[12] Chen C, Wang L, Xia W, Qiu K, Guo C, Gan Z, et al. Molecular interaction induced dual fibrils towards organic solar cells with certified efficiency over 20%. Nature Communications. 2024;15(1):6865.

[13] Qiu D, Adil MA, Lu K, Wei Z. The crystallinity control of polymer donor materials for high-performance organic solar cells. Frontiers in Chemistry. 2020;8:603134.

[14] Koerner C, Elschner C, Cates N, Fitzner R, Selzer F, Reinold E, et al. Probing the effect of substrate heating during deposition of DCV4T: C60 blend layers for organic solar cells. Organic Electronics. 2012;13(4):623-31.

[15] Zhang W, Zhang K, Hao X. Multilength-Scale Morphological Engineering for Stable Organic Solar Cells. Small. 2025;21(15):2412230.

[16] Irfan A, Mahmood A, Al-Sehemi AG, Ahmad F. Experimental and theoretical study of planar small molecule acceptor for organic solar cells. Journal of Molecular Structure. 2019;1196:169-75.

[17] Luo Z, Yan H, Yang C. End-group engineering of nonfullerene acceptors for high-efficiency organic solar cells. Accounts of Materials Research. 2023;4(11):968-81.

[18] Chen Z, Zhang S, Zhang T, Dai J, Yu Y, Li H, et al. Simplified fabrication of high-performance organic solar cells through the design of self-assembling hole-transport molecules. Joule. 2024;8(6):1723-34.

[19] Liu F, Hou T, Xu X, Sun L, Zhou J, Zhao X, et al. Recent advances in nonfullerene acceptors for organic solar cells. Macromolecular Rapid Communications. 2018;39(3):1700555.

[20] Xue P, Cheng P, Han RP, Zhan X. Printing fabrication of large-area non-fullerene organic solar cells. Materials Horizons. 2022;9(1):194-219.

[21] Panidi J, Mazzolini E, Eisner F, Fu Y, Furlan F, Qiao Z, et al. Biorenewable solvents for high-performance organic solar cells. ACS Energy Letters. 2023;8(7):3038-47.

[22] Xu X, Feng K, Yu L, Yan H, Li R, Peng Q. Highly efficient all-polymer solar cells enabled by p-doping of the polymer donor. ACS Energy Letters. 2020;5(7):2434-43.

[23] Xiong W, Meng X, Liu T, Cai Y, Xue X, Li Z, et al. Rational design of perylenediimide-based polymer acceptor for efficient all-polymer solar cells. Organic Electronics. 2017;50:376-83.

[24] Du J, Hu K, Zhang J, Meng L, Yue J, Angunawela I, et al. Polymerized small molecular acceptor based all-polymer solar cells with an efficiency of 16.16% via tuning polymer blend morphology by molecular design. Nature communications. 2021;12(1):5264.

[25] Wang J, Han C, Wen S, Bi F, Hu Z, Li Y, et al. Achieving 17.94% efficiency all-polymer solar cells by independently induced d/a orderly stacking. Energy & Environmental Science. 2023;16(5):2327-37.

[26] Hu L, Qiao W, Han J, Zhou X, Wang C, Ma D, et al. Naphthalene diimide–diketopyrrolopyrrole copolymers as non-fullerene acceptors for use in bulk-heterojunction all-polymer UV–NIR photodetectors. Polymer Chemistry. 2017;8(3):528-36.

doi:10.6342/NTU202502276

[27] Li Y, Song J, Dong Y, Jin H, Xin J, Wang S, et al. Polymerized small molecular acceptor with branched side chains for all polymer solar cells with efficiency over 16.7%. Advanced Materials. 2022;34(14):2110155.

[28] Zhang ZG, Li Y. Polymerized small-molecule acceptors for high-performance all-polymer solar cells. Angewandte Chemie International Edition. 2021;60(9):4422-33.

[29] Li Y, Huang W, Zhao D, Wang L, Jiao Z, Huang Q, et al. Recent progress in organic solar cells: a review on materials from acceptor to donor. Molecules. 2022;27(6):1800.

[30] Yin H, Yan C, Hu H, Ho JKW, Zhan X, Li G, et al. Recent progress of all-polymer solar cells–From chemical structure and device physics to photovoltaic performance. Materials Science and Engineering: R: Reports. 2020;140:100542.

[31] Sun C, Lee JW, Seo S, Lee S, Wang C, Li H, et al. Synergistic engineering of side chains and backbone regioregularity of polymer acceptors for high-performance all-polymer solar cells with 15.1% efficiency. Advanced Energy Materials. 2022;12(3):2103239.

[32] Li Y. Molecular design of photovoltaic materials for polymer solar cells: toward suitable electronic energy levels and broad absorption. Accounts of chemical research. 2012;45(5):723-33.

[33] Zhao J, Yao C, Ali MU, Miao J, Meng H. Recent advances in high-performance organic solar cells enabled by acceptor–donor–acceptor–donor–acceptor (A–DA′ D–A) type acceptors. Materials Chemistry Frontiers. 2020;4(12):3487-504.

[34] Lüer L, Wang R, Liu C, Dube H, Heumüller T, Hauch J, et al. Maximizing performance and stability of organic solar cells at low driving force for charge separation. Advanced science. 2024;11(6):2305948.

doi:10.6342/NTU202502276

[35] Yu R, Wei X, Wu G, Tan Za. Layer-by-layered organic solar cells: Morphology optimizing strategies and processing techniques: Photovoltaics: Special Issue Dedicated to Professor Yongfang Li. Aggregate. 2022;3(3):e107.

[36] Han G, Guo Y, Song X, Wang Y, Yi Y. Terminal π–π stacking determines three-dimensional molecular packing and isotropic charge transport in an A–π–A electron acceptor for non-fullerene organic solar cells. Journal of Materials Chemistry C. 2017;5(20):4852-7.

[37] Tao J, Zhao C, Wang Z, Chen Y, Zang L, Yang G, et al. Suppressing non-radiative recombination for efficient and stable perovskite solar cells. Energy & Environmental Science. 2025;18(2):509-44.

[38] Xu M, Zhang D, Wang Z, Liu Z, Gao X, He J, et al. Highly stretchable All-polymer solar cells enabled by Siloxane-terminated side chains and molecular weight control. Chemical Engineering Journal. 2022;440:135829.

[39] Lee T, Song CE, Lee SK, Shin WS, Lim E. Alkyl-side-chain engineering of nonfused nonfullerene acceptors with simultaneously improved material solubility and device performance for organic solar cells. ACS omega. 2021;6(7):4562-73.

[40] Mooney M, Nyayachavadi A, Awada A, Iakovidis E, Wang Y, Chen M-N, et al. Asymmetric side-chain engineering in semiconducting polymers: A platform for greener processing and post-functionalization of organic electronics. Polymer Chemistry. 2023;14(5):562-72.

[41] Lee Y, Raju TB, Yeom H, Gopikrishna P, Kim K, Cho HW, et al. Alkyl Chain Engineering of Low Bandgap Non-Fullerene Acceptors for High-Performance Organic Solar Cells: Branched vs. Linear Alkyl Side Chains. Polymers. 2022;14(18):3812.

[42] Mei J, Wu HC, Diao Y, Appleton A, Wang H, Zhou Y, et al. Effect of Spacer Length of Siloxane-Terminated Side Chains on Charge Transport in Isoindigo-Based

Polymer Semiconductor Thin Films. Advanced Functional Materials. 2015;25(23):3455-62.

[43] Shin J, Kim M, Kang B, Lee J, Kim HG, Cho K. Impact of side-chain fluorination on photovoltaic properties: fine tuning of the microstructure and energy levels of 2D-conjugated copolymers. Journal of Materials Chemistry A. 2017;5(32):16702-11.

[44] Li S, Yang X, Zhang L, An J, Cai B, Wang X. Effect of fluorine substituents on benzothiadiazole-based D–π–A′–π–A photosensitizers for dye-sensitized solar cells. RSC advances. 2020;10(16):9203-9.

[45] Wei W, Zhou X, Pang S, Zhou J, Yuan X, Li J, et al. A–D–A'–D–A type nonfused ring electron acceptors for efficient organic solar cells via synergistic molecular packing and orientation control. Aggregate. 2024;5(2):e488.

[46] Luo D, Li L, Zhou E, Wong W-Y, Kyaw AKK. Additive engineering for high-performance P3HT: non-fused ring electron acceptor organic solar cell. Materials Advances. 2023;4(19):4444-54.

[47] Kim W, Kim JK, Kim E, Ahn TK, Wang DH, Park JH. Conflicted effects of a solvent additive on PTB7: PC71BM bulk heterojunction solar cells. The Journal of Physical Chemistry C. 2015;119(11):5954-61.

[48] Pan J, Zhang Q, Guan J, Gao H, Li L, Zhang R, et al. Enhancing molecular aggregation and decreasing the optical gap by a dual-additive to reduce the energy loss of all-polymer organic solar cells. Journal of Materials Chemistry C. 2025;13(3):1457-68.

[49] Li Y, Xu X, Shi C, Chen W, Fu Y, Liu W, et al. Triazine derivative as volatile solid additive for non-halogenated solvent and thermal annealing-free processed organic solar cells with over 18% efficiency. Information & Functional Materials. 2024;1(3):323-30.

[50] Hou Y, Wang Q, Yang Y, Yang C, Shen W, Tang J. Morphology Regulation Is Achieved by Volatile Solid Additives in Halogen-Free Solvents to Fabricate Efficient Polymer Solar Cells. ACS Applied Materials & Interfaces. 2025;17(10):15728-40.

[51] Lu L, Zheng T, Wu Q, Schneider AM, Zhao D, Yu L. Recent advances in bulk heterojunction polymer solar cells. Chemical Reviews. 2015;115(23):12666–731.

[52] Cheng P, Li G, Zhan X, Yang Y. Next-generation organic photovoltaics based on non-fullerene acceptors. Nature Photonics. 2018;12(3):131–42.

[53] Liang N, Jiang W, Hou J, Wang Z. New developments in non-fullerene small molecule acceptors for polymer solar cells. Materials Chemistry Frontiers. 2017;1(7):1291–303.

[54] Lipomi DJ, Tee BCK, Vosgueritchian M, Bao Z. Stretchable organic solar cells. Advanced Materials. 2011;23(15):1771–5.

[55] Guo X, Zhou N, Lou SJ, Smith J, Tice DB, Hennek JW, et al. Polymer solar cells with enhanced fill factors. Nature Photonics. 2013;7(10):825–33.

[56] Cui Y, Yao H, Zhang J, Xian K, Zhang T, Hong L, et al. Single-junction organic photovoltaic cells with approaching 18% efficiency. Advanced Materials. 2020;32(19): 1908205.

[57] Luo Z, Ma R, Liu T, Yu J, Xiao Y, Sun R, et al. Fine-tuning energy levels via asymmetric end groups enables polymer solar cells with efficiencies over 17. Joule. 2020;4(6):1236–47.

[58] Zhang ZG, Wang J. Structures and properties of conjugated Donor–Acceptor copolymers for solar cell applications. Journal of Materials Chemistry. 2012;22(10):4178–87.

doi:10.6342/NTU202502276

[59] Holliday S, Li Y, Luscombe CK. Recent advances in high performance donoracceptor polymers for organic photovoltaics. Progress in Polymer Science. 2017;70:34–51.

[60] Ajayaghosh A. Donor–acceptor type low band gap polymers: polysquaraines and related systems. Chemical Society Reviews. 2003;32(4):181–91.

[61] Van Mullekom H, Vekemans J, Havinga E, Meijer E. Developments in the chemistry and band gap engineering of donor–acceptor substituted conjugated polymers. Materials Science and Engineering R: Reports. 2001;32(1):1–40.

[62] Yang J, Xiao B, Tajima K, Nakano M, Takimiya K, Tang A, et al. Comparison among perylene diimide (Pdi), naphthalene diimide (Ndi), and Naphthodithiophene diimide (Ndti) based N-type polymers for all-polymer solar cells application. Macromolecules. 2017;50(8):3179–85.

[63] Lee C, Lee S, Kim G-U, Lee W, Kim BJ. Recent advances, design guidelines, and prospects of all-polymer solar cells. Chemical Reviews. 2019;119(13):8028–86.

[64] Zhou N, Facchetti A. Naphthalenediimide (NDI) polymers for all-polymer photovoltaics. Materials Today. 2018;21(4):377–90.

[65] Qu S, Tian H. Diketopyrrolopyrrole (DPP)-based materials for organic photovoltaics. Chemical Communications. 2012;48(25):3039–51.

[66] Deng P, Zhang Q. Recent developments on isoindigo-based conjugated polymers. Polymer Chemistry. 2014;5(10):3298–305.

[67] Wei X, Zhang W, Yu G. Semiconducting polymers based on isoindigo and its derivatives: synthetic tactics, structural modifications, and applications. Advanced Functional Materials. 2021:2010979.

doi:10.6342/NTU202502276

[68] Gu H, Ming S, Lin K, Chen S, Liu X, Lu B, et al. Isoindigo as an electron-deficient unit for high-performance polymeric electrochromics. Electrochimica Acta. 2018; 260:772–82.

[69] Lin Y-C, Chen F-H, Chiang Y-C, Chueh C-C, Chen W-C. Asymmetric side-chain engineering of isoindigo-based polymers for improved stretchability and applications in field-effect transistors. ACS Applied Materials & Interfaces. 2019;11(37):34158–70.

[70] Zhou Y, Kurosawa T, Ma W, Guo Y, Fang L, Vandewal K, et al. High performance all-polymer solar cell via polymer side-chain engineering. Advanced Materials. 2014;26(22):3767–72.

[71] Mei J, Bao Z. Side chain engineering in solution-processable conjugated polymers. Chemistry of Materials. 2014;26(1):604–15.

[72] Liu T, Pan X, Meng X, Liu Y, Wei D, Ma W, et al. Alkyl side-chain engineering in wide-bandgap copolymers leading to power conversion efficiencies over 10. Advanced Materials. 2017;29(6):1604251.

[73] Back JY, Yu H, Song I, Kang I, Ahn H, Shin TJ, et al. Investigation of structure–property relationships in diketopyrrolopyrrole-based polymer semiconductors via side-chain engineering. Chemistry of Materials. 2015;27(5):1732–9.

[74] Lei T, Wang J-Y, Pei J. Roles of flexible chains in organic semiconducting materials. Chemistry of Materials. 2014;26(1):594–603.

[75] Wang T, Coropceanu V, Br´edas J-L. All-polymer solar cells: impact of the length of the branched alkyl side chains on the polymer acceptors on the interchain packing and electronic properties in amorphous blends. Chemistry of Materials. 2019;31(16):6239–48.

[76] Yang S-F, Liu Z-T, Cai Z-X, Luo H-W, Qi P-L, Zhang G-X, et al. Conjugated donor–acceptor polymers entailing Pechmann Dye-derived acceptor with

doi:10.6342/NTU202502276

siloxaneterminated side chains exhibiting balanced ambipolar semiconducting behavior. Macromolecules. 2016;49(16):5857–65.

[77] Kim Y, Long DX, Lee J, Kim G, Shin TJ, Nam K-W, et al. A balanced face-on to edgeon texture ratio in naphthalene diimide-based polymers with hybrid siloxane chains directs highly efficient electron transport. Macromolecules. 2015;48(15):5179–87.

[78] Lee J, Han A-R, Yu H, Shin TJ, Yang C, Oh JH. Boosting the ambipolar performance of solution-processable polymer semiconductors via hybrid side-chain engineering. Journal of the American Chemical Society. 2013;135(25):9540–7.

[79] Lee J, Han A-R, Kim J, Kim Y, Oh JH, Yang C. Solution-processable ambipolar diketopyrrolopyrrole–selenophene polymer with unprecedentedly high hole and electron mobilities. Journal of the American Chemical Society. 2012;134(51):20713–21.

[80] Kamatham N, Ibraikulov OA, Durand P, Wang J, Boyron O, Heinrich B, et al. On the impact of linear siloxanated side chains on the molecular self-assembling and charge transport properties of conjugated polymers. Advanced Functional Materials. 2021;31(6):2007734.

[81] Feng S, Zhang Ce, Liu Y, Bi Z, Zhang Z, Xu X, et al. Fused-ring acceptors with asymmetric side chains for high-performance thick-film organic solar cells. Advanced Materials. 2017;29(42):1703527.

[82] Chen X, Kan B, Kan Y, Zhang M, Jo SB, Gao K, et al. As-cast ternary organic solar cells based on an asymmetric side-chains featured acceptor with reduced voltage loss and 14.0% efficiency. Advanced Functional Materials. 2020;30(11):1909535.

[83] Kan B, Chen X, Gao K, Zhang M, Lin F, Peng X, et al. Asymmetrical side-chain engineering of small-molecule acceptors enable high-performance nonfullerene organic solar cells. Nano Energy. 2020;67:104209.

doi:10.6342/NTU202502276

[84] Chao P, Liu L, Qu J, He Q, Gan S, Meng H, et al. Overcoming the trade-off between Voc and Jsc: asymmetric chloro-substituted two-dimensional benzo [1, 2-b: 4, 5-b′] dithiophene-based polymer solar cells. Dyes and Pigments. 2019;162:746 – 54.

[85] Tang Z, Xu X, Li R, Yu L, Meng L, Wang Y, et al. Asymmetric siloxane functional side chains enable high-performance donor copolymers for photovoltaic applications. ACS Applied Materials & Interfaces. 2020;12(15):17760–8.

[86] An Q, Ma X, Gao J, Zhang F. Solvent additive-free ternary polymer solar cells with 16.27% efficiency. Science Bulletin. 2019;64(8):504–6.

[87] Zhou H, Yang L, Stuart AC, Price SC, Liu S, You W. Development of fluorinated benzothiadiazole as a structural unit for a polymer solar cell of 7% efficiency. Angewandte Chemie. 2011;123(13):3051–4.

[88] Zhang M, Guo X, Zhang S, Hou J. Synergistic effect of fluorination on molecular energy level modulation in highly efficient photovoltaic polymers. Advanced Materials. 2014;26(7):1118–23.

[89] Peng F, An K, Zhong W, Li Z, Ying L, Li N, et al. A universal fluorinated polymer acceptor enables all-polymer solar cells with> 15% efficiency. ACS Energy Letters. 2020;5(12):3702–7.

[90] Meyer F. Fluorinated conjugated polymers in organic bulk heterojunction photovoltaic solar cells. Progress in Polymer Science. 2015;47:70–91.

[91] Leclerc N, Ch´avez P, Ibraikulov OA, Heiser T, L´evˆeque P. Impact of backbone fluorination on π-conjugated polymers in organic photovoltaic devices: a review. Polymers. 2016;8(1):11.

[92] Deng D, Zhang Y, Zhang J, Wang Z, Zhu L, Fang J, et al. Fluorination-enabled optimal morphology leads to over 11% efficiency for inverted small-molecule organic solar cells. Nature Communications. 2016;7(1):1–9.

doi:10.6342/NTU202502276

[93] Fan Q, M´endez-Romero UA, Guo X, Wang E, Zhang M, Li Y. Fluorinated photovoltaic materials for high-performance organic solar cells. Chemistry-An Asian Journal. 2019;14(18):3085–95.

[94] Cowan SR, Roy A, Heeger AJ. Recombination in polymer-fullerene bulk heterojunction solar cells. Physical Review B. 2010;82(24):245207.

[95] Xu X, Li Z, Bi Z, Yu T, Ma W, Feng K, et al. Highly efficient nonfullerene polymer solar cells enabled by a copper (I) coordination strategy employing a 1, 3, 4-Oxadiazole-containing wide-bandgap copolymer donor. Advanced Materials. 2018;30(28):1800737.

[96] Lakhwani G, Rao A, Friend RH. Bimolecular recombination in organic photovoltaics. Annual Review of Physical Chemistry. 2014;65:557–81.

[97] Wetzelaer G, Kuik M, Lenes M, Blom P. Origin of the dark-current ideality factor in polymer: fullerene bulk heterojunction solar cells. Applied Physics Letters. 2011;99(15):153506.

[98] Cowan SR, Leong WL, Banerji N, Dennler G, Heeger AJ. Identifying a threshold impurity level for organic solar cells: enhanced first-order recombination via well-defined PC84BM traps in organic bulk heterojunction solar cells. Advanced Functional Materials. 2011;21(16):3083–92.

[99] Kang H, Uddin MA, Lee C, Kim K-H, Nguyen TL, Lee W, et al. Determining the role of polymer molecular weight for high-performance all-polymer solar cells: its effect on polymer aggregation and phase separation. Journal of the American Chemical Society. 2015;137(6):2359–65.

[100] Fan B, Ying L, Zhu P, Pan F, Liu F, Chen J, et al. All-polymer solar cells based on a conjugated polymer containing siloxane-functionalized side chains with efficiency over 10. Advanced Materials. 2017;29(47):1703906.

doi:10.6342/NTU202502276

[101] Jia T, Zhang J, Zhang K, Tang H, Dong S, Tan C-H, et al. All-polymer solar cells with efficiency approaching 16% enabled using a dithieno [3′, 2′: 3, 4; 2″, 3″: 5, 6] benzo [1, 2-c][1, 2, 5] thiadiazole (fDTBT)-based polymer donor. Journal of Materials Chemistry A. 2021;9(14):8975-83.

[102] Wang J, Li Y, Han C, Chen L, Bi F, Hu Z, et al. All-polymer solar cells with 19% efficiency via introducing pincer-shaped non-covalent bond interactions. Energy & Environmental Science. 2024;17(12):4216-27.

[103] Fan B, Ying L, Zhu P, Pan F, Liu F, Chen J, et al. All-polymer solar cells based on a conjugated polymer containing siloxane-functionalized side chains with efficiency over 10%. Advanced materials. 2017;29(47):1703906.

[104] Zhao W, Li S, Yao H, Zhang S, Zhang Y, Yang B, et al. Molecular optimization enables over 13% efficiency in organic solar cells. Journal of the American Chemical Society. 2017;139(21):7148-51.

[105] Yi C, Hu X, Liu HC, Hu R, Hsu C-H, Zheng J, et al. Efficient polymer solar cells fabricated from solvent processing additive solution. Journal of Materials Chemistry C. 2015;3(1):26-32.

[106] Wang T, Chen M, Sun R, Min J. Recent research progress of all-polymer solar cells based on PSMA-type polymer acceptors. Chem. 2023;9(7):1702-67.

[107] Li Y, Li Q, Cai Y, Jin H, Zhang J, Tang Z, et al. An efficient polymer acceptor via a random polymerization strategy enables all-polymer solar cells with efficiency exceeding 17%. Energy & Environmental Science. 2022;15(9):3854-61.

[108] Sun R, Wang W, Yu H, Chen Z, Xia X, Shen H, et al. Achieving over 17% efficiency of ternary all-polymer solar cells with two well-compatible polymer acceptors. Joule. 2021;5(6):1548-65.

doi:10.6342/NTU202502276

[109] Zhang L, Yao Z, Wang H, Zhang J, Ma X, Zhang F. Recent progress of all polymer solar cells with efficiency over 15%. Solar RRL. 2023;7(12):2300219.

[110] Majhi J, Ghosh S, Priya K, Sharma S, Bandyopadhyay A. A critical review on the progress of emerging active and substrate materials for organic solar cells and device level fabrication techniques by solution process method. Next Materials. 2025;8:100595.

[111] Zhou K, Xian K, Ye L. Morphology control in high-efficiency all-polymer solar cells. InfoMat. 2022;4(4):e12270.

[112] Yue Y, Zheng B, Ni J, Yang W, Huo L, Wang J, et al. All-Polymer Solar Cells with 17% Efficiency Enabled by the “End-Capped” Ternary Strategy. Advanced Science. 2022;9(32):2204030.

[113] Yu R, Yao H, Hong L, Qin Y, Zhu J, Cui Y, et al. Design and application of volatilizable solid additives in non-fullerene organic solar cells. Nature communications. 2018;9(1):4645.

[114] Shen W, Chen W, Zhu D, Zhang J, Xu X, Jiang H, et al. High-performance ternary polymer solar cells from a structurally similar polymer alloy. Journal of Materials Chemistry A. 2017;5(24):12400-6.

[115] Jeon J, Doi K, Kim HD, Ogawa H, Takenaka M, Ohkita H. Correlating the structures and photovoltaic properties in phase-separated blends of conjugated donor polymers and acceptors. Polymer Journal. 2023;55(4):477-87.

[116] Memon WA, Deng Z, He F. Recent development in solid additives enables high-performance organic solar cells. EnergyChem. 2024:100129.

[117] Liang Q, Li H, Xu W, Lu J, Ma R, Bai Q, et al. Dual-Asymmetric Solid Additive Enables Eco-friendly All-Polymer Solar Cells with Over 19% Efficiency and Excellent Stability. Angewandte Chemie International Edition. 2025;64(14):e202425267.

doi:10.6342/NTU202502276

[118] McDowell C, Abdelsamie M, Toney MF, Bazan GC. Solvent additives: key morphology-directing agents for solution-processed organic solar cells. Advanced Materials. 2018;30(33):1707114.

[119] Mishra A, Bhuyan NN, Xu H, Sharma GD. Advances in layer-by-layer processing for efficient and reliable organic solar cells. Materials Advances. 2023;4(23):6031-63.

[120] Choi JY, Han YW, Jeon SJ, Ko EJ, Moon DK. Introduction of co-additives to form well dispersed photoactive layer to improve performance and stability of organic solar cells. Solar Energy. 2019;185:1-12.

[121] Xiong Y, Ye L, Zhang C. Eco-friendly solution processing of all-polymer solar cells: Recent advances and future perspective. Journal of Polymer Science. 2022;60(6):945-60.

[122] Tremolet de Villers BJ, O'Hara KA, Ostrowski DP, Biddle PH, Shaheen SE, Chabinyc ML, et al. Removal of residual diiodooctane improves photostability of high-performance organic solar cell polymers. Chemistry of Materials. 2016;28(3):876-84.

[123] Tournebize A, Rivaton A, Peisert H, Chassé T. The crucial role of confined residual additives on the photostability of P3HT: PCBM active layers. The Journal of Physical Chemistry C. 2015;119(17):9142-8.

[124] Liang Q, Li W, Lu H, Yu Z, Zhang X, Dong Q, et al. Recent advances of solid additives used in organic solar cells: toward efficient and stable solar cells. ACS Applied Energy Materials. 2022;6(1):31-50.

[125] Huang X, Sun Y, Zhao Z, Chung S, Cho K, Kan Z. Triggering the Donor–Acceptor Phase Segregation with Solid Additives Enables 16.5% Efficiency in All-Polymer Solar Cells. ACS Applied Materials & Interfaces. 2023;15(37):44012-21.

[126] Zhang G, Hu D, Tang H, Song H, Duan S, Kan Z, et al. Volatile Additive Strategy Triggering 17.48% Efficient Post-Treatment-Free Organic Solar Cells. Solar RRL. 2023;7(4):2200994.

[127] Corzo D, Rosas-Villalva D, Tostado-Blázquez G, Alexandre EB, Hernandez LH, Han J, et al. High-performing organic electronics using terpene green solvents from renewable feedstocks. Nature Energy. 2023;8(1):62-73.

[128] Moon Y, Han N, Lee M, Song GC, Yang D, Beak J, et al. Improving the efficiency of all-polymer solar cells through morphology control via a combination approach: polar solvent additives and external electric field. Journal of Materials Chemistry C. 2025.

[129] Liu S, You Z, Wu T, Feng Y, Cao J, Hou L, et al. Toward Eco-Friendly Solvent-Processable DPP-Based Conjugated Polymers with Siloxane Branched Side Chains: Synthesis, Properties, and Ambipolar Field-Effect Transistor Characteristics. ACS Applied Electronic Materials. 2025.

[130] Buckley A. Analysing space charge limited currents in organic light emitting diodes. Synthetic metals. 2010;160(5-6):540-3.

[131] Zhang X, Li C, Xu J, Wang R, Song J, Zhang H, et al. High fill factor organic solar cells with increased dielectric constant and molecular packing density. Joule. 2022;6(2):444-57.

[132] Liu T, Yang T, Ma R, Zhan L, Luo Z, Zhang G, et al. 16% efficiency all-polymer organic solar cells enabled by a finely tuned morphology via the design of ternary blend. Joule. 2021;5(4):914-30.

[133] Wanderley RR, Knuutila HK. Evaluating the possibility of high-pressure desorption of CO2 via volatile co-solvent injection. Chemical Engineering Research and Design. 2021;169:116-34.

doi:10.6342/NTU202502276

[134] Ling F, Li S, Song X, Wang Y, Long J, Zhang B. Femtosecond time-resolved observation of butterfly vibration in electronically excited o-fluorophenol. Scientific Reports. 2017;7(1):15362.

[135] Sun G, Jiang X, Li X, Meng L, Zhang J, Qin S, et al. High performance polymerized small molecule acceptor by synergistic optimization on π-bridge linker and side chain. Nature Communications. 2022;13(1):5267.

[136] Liu B, Gámez-Valenzuela S, Lee J-W, Li B, Yang W, Wang K, et al. High-Performance Annealing-Free Polythiophene-Based Organic Solar Cells Enabled by Volatile Solid Additive. ACS Energy Letters. 2024;9(8):3727-36.

[137] Müller-Buschbaum P. GISAXS and GISANS as metrology technique for understanding the 3D morphology of block copolymer thin films. European Polymer Journal. 2016;81:470-93.

[138] Chang J-F, Hsieh C-T, Su L-Y, Chueh C-C. Reducing the side-chain influences of isoindigo-based polymer donors by backbone fluorination in photovoltaic applications. Dyes and Pigments. 2022;199:110038.

[139] Du M, Chen Y, Li J, Geng Y, Ji H, Li G, et al. Wide-band-gap phthalimide-based D-π-A polymers for nonfullerene organic solar cells: the effect of conjugated π-bridge from thiophene to thieno [3, 2-b] thiophene. The Journal of Physical Chemistry C. 2019;124(1):230-6.

[140] Tseng Y-C, Kato A, Chang J-F, Chen W-C, Higashihara T, Chueh C-C. Impact of the segment ratio on a donor–acceptor all-conjugated block copolymer in single-component organic solar cells. Nanoscale. 2022;14(14):5472-81.

[141] Wang Y, Yu H, Wu X, Zhao D, Zhang S, Zou X, et al. Boosting the Fill Factor through Sequential Deposition and Homo Hydrocarbon Solvent toward Efficient and Stable All-Polymer Solar Cells. Advanced Energy Materials. 2022;12(48):2202729.

doi:10.6342/NTU202502276

[142] Cui F, Qiao J, Xu Y, Fu Z, Gui R, Zhang C, et al. Using an external electric field to tune active layer morphology enabling high-efficiency organic solar cells via ambient blade coating. Science Advances. 2024;10(26):eado5460.

[143] Yu H, Wang Y, Zou X, Han H, Kim HK, Yao Z, et al. Effects of Halogenation of Small-Molecule and Polymeric Acceptors for Efficient Organic Solar Cells. Advanced Functional Materials. 2023;33(22):2300712.

[144] Yu H, Wang Y, Kim HK, Wu X, Li Y, Yao Z, et al. A vinylene-linker-based polymer acceptor featuring a coplanar and rigid molecular conformation enables high-performance all-polymer solar cells with over 17% efficiency. Advanced Materials. 2022;34(27):2200361.

[145] Rey G, Spindler C, Babbe F, Rachad W, Siebentritt S, Nuys M, et al. Absorption coefficient of a semiconductor thin film from photoluminescence. Physical Review Applied. 2018;9(6):064008.

[146] Wu J, Lee J, Chin Y-C, Yao H, Cha H, Luke J, et al. Exceptionally low charge trapping enables highly efficient organic bulk heterojunction solar cells. Energy & Environmental Science. 2020;13(8):2422-30.

[147] Song X, Song Y, Xu H, Gao S, Wang Y, Li J, et al. Solvent-Induced Anti-Aggregation Evolution on Small Molecule Electron-Transporting Layer for Efficient, Scalable, and Robust Organic Solar Cells. Advanced Energy Materials. 2023;13(1):2203009.

[148] Luo Z, Liu T, Ma R, Xiao Y, Zhan L, Zhang G, et al. Precisely controlling the position of bromine on the end group enables well-regular polymer acceptors for all-polymer solar cells with efficiencies over 15%. Advanced Materials. 2020;32(48):2005942.

doi:10.6342/NTU202502276

[149] Ma L, Cui Y, Zhang J, Xian K, Chen Z, Zhou K, et al. High-Efficiency and Mechanically Robust All-Polymer Organic Photovoltaic Cells Enabled by Optimized Fibril Network Morphology. Advanced Materials. 2023;35(9):2208926.

[150] Zhang G, Wang L, Zhao C, Wang Y, Hu R, Che J, et al. Efficient all-polymer solar cells enabled by interface engineering. Polymers. 2022;14(18):3835.

[151] Zhang T, Xu Y, Yao H, Zhang J, Bi P, Chen Z, et al. Suppressing the energetic disorder of all-polymer solar cells enables over 18% efficiency. Energy & Environmental Science. 2023;16(4):1581-9.

[152] Yue Y, Zheng B, Yang W, Huo L, Wang J, Jiang L. Meniscus-assisted coating with optimized active-layer morphology toward highly efficient all-polymer solar cells. Advanced Materials. 2022;34(14):2108508.

[153] Ma R, Zhou K, Sun Y, Liu T, Kan Y, Xiao Y, et al. Achieving high efficiency and well-kept ductility in ternary all-polymer organic photovoltaic blends thanks to two well miscible donors. Matter. 2022;5(2):725-34.

[154] Zhang W, Sun C, Angunawela I, Meng L, Qin S, Zhou L, et al. 16.52% Efficiency All-Polymer Solar Cells with High Tolerance of the Photoactive Layer Thickness. Advanced Materials. 2022;34(20):2108749.

[155] Cui FZ, Chen ZH, Qiao JW, Wang T, Lu GH, Yin H, et al. Ternary-assisted sequential solution deposition enables efficient all-polymer solar cells with tailored vertical-phase distribution. Advanced Functional Materials. 2022;32(24):2200478.

[156] Sun Y, Ma R, Kan Y, Liu T, Zhou K, Liu P, et al. Simultaneously Enhanced Efficiency and Mechanical Durability in Ternary Solar Cells Enabled by Low-Cost Incompletely Separated Fullerenes. Macromolecular Rapid Communications. 2022;43(22):2200139.

doi:10.6342/NTU202502276

[157] Yu X, Lin H, Li M, Ma B, Zhang R, Du X, et al. Ternary organic solar cells with enhanced charge transfer and stability combining the advantages of polymer acceptors and fullerene acceptors. Organic Electronics. 2022;104:106471.

[158] Ma R, Yu J, Liu T, Zhang G, Xiao Y, Luo Z, et al. All-polymer solar cells with over 16% efficiency and enhanced stability enabled by compatible solvent and polymer additives: Photovoltaics: Special Issue Dedicated to Professor Yongfang Li. Aggregate. 2022;3(3):e58.

[159] Hu K, Du J, Zhu C, Lai W, Li J, Xin J, et al. Chlorinated polymerized small molecule acceptor enabling ternary all-polymer solar cells with over 16.6% efficiency. Science China Chemistry. 2022;65(5):954-63.

doi:10.6342/NTU202502276